

**UCLA**

**UCLA Electronic Theses and Dissertations**

**Title**

Lensfree Optical Tomography for High-Throughput 3D Imaging on a Chip

**Permalink**

<https://escholarship.org/uc/item/7n01r1cc>

**Author**

ISIKMAN, SERHAN OMER

**Publication Date**

2012

Peer reviewed|Thesis/dissertation

UNIVERSITY OF CALIFORNIA

Los Angeles

Lensfree Optical Tomography for High-Throughput 3D Imaging on a Chip

A dissertation submitted in partial satisfaction of the requirements for the degree Doctor of  
Philosophy in Electrical Engineering

by

Serhan Omer Isikman

2012



## ABSTRACT OF THE DISSERTATION

Lensfree Optical Tomography for High-Throughput 3D Imaging on a Chip

by

Serhan Omer Isikman

Doctor of Philosophy in Electrical Engineering

University of California, Los Angeles, 2012

Professor Aydogan Ozcan, Chair

Light microscopes provide us with the key to observe objects that are orders of magnitude smaller than what the unaided eye can see. Therefore, microscopy has been the cornerstone of science and medicine for centuries. Recently, optical microscopy has seen a growing interest in developing three-dimensional (3D) imaging techniques that enable sectional imaging of biological specimen. These imaging techniques, however, are generally quite complex, bulky and expensive in addition to having a limited field-of-view due to the need for lens-based optical magnification.

In this thesis, I demonstrate lensfree optical tomography (LOT) as a new 3D imaging modality that offers high-throughput imaging in a compact and simple architecture. This technique is fundamentally based on lensfree on-chip microscopy, where computation is used to replace bulky components of traditional imaging devices to reduce size, cost and complexity

while at the same time significantly enlarging the imaging field-of-view. In LOT, in-line holograms of objects at different illumination angles are recorded using a digital sensor-array, which enables computing pixel super-resolved tomographic images of the specimen. LOT offers <math><350\text{nm}</math> lateral resolution and  $\sim 2\ \mu\text{m}$  axial resolution over large imaging volumes of e.g., 15-100  $\text{mm}^3$ , and can be assembled in lightweight and compact architectures. The imaging performance of LOT is quantified using spherical microparticles as well as using biological specimen such as *C. elegans* worms and *H. Nana* eggs.

To demonstrate that LOT could be useful for imaging applications in resource-limited settings, I also devised a field-portable, USB-powered compact and lightweight tomographic microscope that only weighs  $\sim 110$  grams. This portable device can fit in a volume of 96 mm x 89 mm x 40 mm. In addition, to demonstrate the integration of LOT in microfluidic platforms and lab-on-a-chip systems, I also introduce an optofluidic tomography platform. In this system, the sample is delivered to the tomographic imager through a microfluidic chamber, which is mounted on the sensor chip. Tomographic data acquisition is performed while the objects are electrokinetically driven through the chamber.

Probing a large volume at micrometer-scale 3D spatial resolution, LOT could provide a powerful imaging tool for high-throughput imaging applications in e.g., cell and developmental biology, as well as for future lab-on-chip platforms.

The dissertation of Serhan Omer Isikman is approved.

Oscar Stafsudd

Laurent Pilon

Benjamin Williams

Aydogan Ozcan, Committee Chair

University of California, Los Angeles

2012

## TABLE OF CONTENTS

<b>1 INTRODUCTION</b> .....	<b>1</b>
<b>2 LENSFREE ON-CHIP HOLOGRAPHIC MICROSCOPY</b> .....	<b>6</b>
2.1. Basic Principles of Lensfree On-Chip Holographic Microscopy .....	6
2.2 Theoretical Analysis of Lensfree On-Chip Holography .....	8
2.3. Digital Reconstruction in Lensfree On-Chip Holographic Imaging .....	13
2.4. Implementation of Pixel Super-Resolution in Lensfree On-Chip Holography .....	15
<b>3 LENSFREE OPTICAL TOMOGRAPHY</b> .....	<b>18</b>
3.1 Introduction .....	18
3.2 Experimental Methods .....	20
3.2.1 Acquisition of holographic projections .....	20
3.2.2 Reconstruction of the holograms to obtain lensfree projection images .....	22
3.2.3 3D image reconstruction in lensfree optical tomography .....	25
3.2.4 Validity of the projection assumption for lensfree images of weakly scattering objects .....	27
3.3 Experimental Results .....	29
3.4 Discussion .....	38
<b>4 FIELD-PORTABLE LENSFREE TOMOGRAPHIC MICROSCOPE</b> .....	<b>43</b>
4.1 Introduction .....	43
4.2 Experimental Methods .....	44
4.3 Experimental Results .....	48
<b>5 OPTOFLUIDIC TOMOGRAPHIC MICROSCOPY</b> .....	<b>54</b>
5.1 Introduction .....	54
5.2 Experimental Methods for Holographic Optofluidic Microscopy (HOM) .....	55
5.3 Experimental Methods for Holographic Optofluidic Tomography (HOT) .....	61
5.3 Experimental Results .....	63
<b>6 CONCLUSION</b> .....	<b>68</b>
<b>APPENDIX 1: Color and Monochrome Lensless On-chip Imaging of Caenorhabditis Elegans Over a Wide Field-of-View</b> .....	<b>71</b>
A1.1 Introduction .....	71
A1.2 Experimental Methods and Results .....	72
<b>APPENDIX 2: Tomographic Image Reconstruction using Filtered Backprojection</b> .....	<b>79</b>
A2.1 Fourier Slice Theorem .....	80
A2.2 Filtered Backprojection Algorithm .....	82
<b>References</b> .....	<b>86</b>

## ACKNOWLEDGEMENT

Foremost, I would like to express my utmost gratitude to my thesis advisor Prof. Aydogan Ozcan for providing his invaluable support, both financially and scientifically, and brilliant ideas throughout my research. I have always been inspired by his unique way of showing genuine trust in my ability to conduct independent research, while at the same time providing his endless energy, guidance and motivation to ensure I always stayed on track and moved forward. Without doubt, the four years I spent at the Ozcan Biophotonics Laboratory at UCLA will remain among the most productive periods of my research career.

I would like to sincerely thank Prof. Oscar Stafsudd, Prof. Laurent Pilon and Prof. Benjamin Williams for kindly taking part in my thesis committee, and providing their invaluable insights for my research.

I would like to thank my colleagues at Ozcan Biophotonics Laboratory for making the long hours spent in the lab so much fun. For sure, I learned a lot from all my colleagues. It was encouraging to see that one friend was always in the lab working at any given time of the day. Those years spent and friendships made at Ozcan Biophotonics Laboratory will always remain memorable.

Last, but definitely not the least, I would like to thank my wife, Elif Sicim Isikman. Listing the infinitely many reasons to thank her would be an attempt to achieve the impossible. For all I know, this work would not be possible in her absence.



## Vita

Serhan O. Isikman received his B.S. and M.S. degrees in Electrical Engineering from Koc University, Turkey in 2006 and 2008, respectively. Between 2008 and 2009, he worked as a consulting engineer for Microvision Inc., WA, USA.

## Book Chapters

**2. S. O. Isikman**, W. Bishara, O. Mudanyali, T. Su, D. Tseng and A. Ozcan, *Lensfree Computational Microscopy Tools for On-Chip Imaging of Bio-Chips*, in “Point of Care Diagnostics on a Chip”, Editors: Robert M Westervelt and David Issadore, Springer (to be published in 2013)

**1. S. O. Isikman**, A. Greenbaum, M. J. Lee, W. Bishara, O. Mudanyali, T. W. Su, A. Ozcan, “*Lensfree Computational Microscopy for Cell and Tissue Imaging at the Point-of-Care and in Low-Resource Settings*”, in “New Approaches to Cell and Tissue Imaging in Pathology”, Editor: Stanley Cohen, (to be published in 2013)

## Peer-reviewed Journal Publications

17. H. Zhu, **S. O. Isikman**, O. Mudanyali, A. Greenbaum and A. Ozcan, “Optical Imaging Techniques for Point-of-Care Diagnostics”, *Lab Chip*, 10.1039/C2LC40864C (2012).

16. A. Greenbaum, W. Luo, T-W. Su, Z. Gorocs, L. Xue, **S.O. Isikman**, A.F. Coskun, O. Mudanyali, and A. Ozcan, “Imaging without lenses: achievements and remaining challenges of wide-field on-chip microscopy,” *Nature Methods*, vol.9, no.9 (2012)

15. **S. O. Isikman**, A. Greenbaum, W. Luo, A. Coskun, and A. Ozcan, "Giga-Pixel Lensfree Holographic Microscopy and Tomography using Color Image Sensors", accepted for publication in *PLoS ONE*, 7(9), e45044 (2012)

14. **S. O. Isikman**, A. Greenbaum, M. Lee, W. Bishara, O. Mudanyali, T. W. Su and A. Ozcan, "Lensfree computational microscopy tools for cell and tissue imaging at the point-of-care and in low-resource settings", *Anal. Cell. Pathology*, vol. 36, pp. 1–19 (2012)

13. (invited paper) **S. O. Isikman**, W. Bishara, A. Ozcan, “Partially Coherent Lensfree Optical Tomographic Microscopy”, *Applied Optics*, vol. 50, iss. 34, 253-264 (2011)

12. (invited paper) W. Bishara, **S. O. Isikman**, A. Ozcan, “Lensfree Optofluidic Microscopy and Tomography”, *Annals of Biomed. Eng.*, DOI: 10.1007/s10439-011-0385-3 (2011)

11. (invited paper) **S. O. Isikman**, W. Bishara, O. Mudanyali, I. Sencan, T.W. Su, D. Tseng, O. Yaglidere, U. Sikora, A. Ozcan, “Lensfree On-Chip Microscopy and Tomography for Global

- Health Applications”, *IEEE J. Sel. Top. Quant. Elect.*, DOI:10.1109/JSTQE.2011.2161460 (2011)
10. G. Biener, A. Greenbaum, **S. O. Isikman**, K. Lee, D. Tseng and A. Ozcan, “Combined reflection and transmission microscope for telemedicine applications in field settings”, *Lab Chip*, DOI: 10.1039/C1LC20169G, (2011)
  9. **S. O. Isikman**, W. Bishara, S. Mavandadi, S. W. Yu, S. Feng, R. Lau, A. Ozcan, “Lens-free optical tomographic microscope with a large imaging volume on a chip”, *Proc. Nat. Acad. Sci. (PNAS)* doi:10.1073/pnas.1018057108 (2011)
  8. **S. O. Isikman**, W. Bishara, U. Sikora, O. Yaglidere, J. Yeah and A. Ozcan, “Field-portable Lensfree Tomographic Microscope”, DOI:10.1039/C1LC20127A, *Lab Chip* (2011)
  7. **S. O. Isikman**, W. Bishara, H. Zhu, A. Ozcan, “Optofluidic Tomography on a Chip”, *Applied Physics Letters*, 89, 161109 (2011)
  6. S. Seo, **S.O. Isikman**, I. Sencan, O. Mudanyali, T. Su, W. Bishara, A. Erlinger and A. Ozcan, “High-throughput Lensfree Blood Analysis On a Chip”, *Analytical Chemistry*, 2010, DOI: 10.1021/ac1007915
  5. Ting-Wei Su, **S. O. Isikman**, Waheb Bishara, Derek Tseng, Anthony Erlinger, and Aydogan Ozcan, “Multi-angle lensless digital holography for depth resolved imaging on a chip”, *Optics Express*, vol. 18, issue 9, pp.9690-9711 (2010)
  4. D. Tseng, O. Mudanyali, C. Oztoprak, **S.O. Isikman**, I. Sencan, O. Yaglidere and A. Ozcan, “Lensfree Microscopy on a Cell-phone”, *Lab Chip* 10, 1787-1792 (2010)
  3. O. Mudanyali, D. Tseng, C. Oh, **S.O. Isikman**, I. Sencan, W. Bishara, C. Oztoprak, S. Seo, B. Khademhosseini, and A. Ozcan, “Compact, Light-weight and Cost-effective Microscope based on Lensless Incoherent Holography for Telemedicine Applications”, *Lab Chip*, 10(11) 1417-1428 (2010)
  2. **S. O. Isikman**, I. Sencan, O. Mudanyali, W. Bishara, C. Oztoprak and Aydogan Ozcan, “Color and Monochrome Lensless On-chip Imaging of Caenorhabditis Elegans Over a Wide Field-of-View”, *Lab Chip*, DOI: 10.1039/C001200A, (2010)
  1. C. Oh, **S.O. Isikman**, B. Khademhosseini, and Aydogan Ozcan, “On-chip differential interference contrast microscopy using lensless digital holography,” *Optics Express*, Vol. 18 Issue 5, 4717-4726 (2010)

## 1 INTRODUCTION

Light microscopy has been an irreplaceable tool in life sciences for several centuries. The quest to resolve smaller features with higher resolution and contrast has improved the capabilities of this important tool at the cost of relatively increasing its size and complexity [1]. Unfortunately, this restricts the use of advanced light microscopes to well-equipped laboratories with trained personnel. Moreover, we have experienced the flourishing of emerging technologies such as microfluidic and lab-on-a-chip systems, which offer fast and efficient handling and processing of biological samples within highly miniaturized architectures [2-7]. The optical inspection of specimen, however, is still being performed by conventional light microscopes, which in general have several orders of magnitude size mismatch compared to the scale of the microfluidic systems. As a result, there is a clear need for alternative compact and cost-effective microscopy modalities for use in low-resource settings as well as towards integration with miniaturized lab-on-a-chip platforms [8].

The urge for new optical microscopy modalities is not solely driven by the need for lowering costs, miniaturization and microfluidic integration. The fact that high resolution is achieved at the cost of significant field-of-view (FOV) reduction is another fundamental limitation of lens-based imaging. The relatively small FOV of conventional light microscopy brings additional challenges for its application to several important problems such as rare cell imaging or optical phenotyping of model organisms [9-15], where high throughput microscopy is highly desired.

In order to provide complementary solutions to these aforementioned needs, several lensfree digital microscopy techniques [16-24] were introduced over the last few years. Along

the same lines, lensfree holographic on-chip microscopy has also been recently developed, which is an imaging platform that combines high resolution and large FOV in a compact, on-chip imaging architecture [25-31]. In this modality, digital in-line holograms of micro-objects are recorded on a sensor array using partially coherent illumination with unit fringe magnification such that the entire active area of the sensor serves as the imaging FOV. To overcome the resolution limitation imposed by the pixel size at the sensor, multiple sub-pixel shifted holograms of the sample are acquired, and pixel super-resolution techniques are then applied to achieve sub-micron lateral resolution [31], reaching a numerical aperture (NA) of  $\sim 0.8-0.9$ , without compromising the FOV (e.g.  $24 \text{ mm}^2$ ).

While pixel super-resolution techniques in partially coherent lensfree in-line holography enable imaging with sub-micron lateral resolution over a large FOV, the axial resolution is unfortunately significantly lower due to the inherently long depth-of-focus of digital in-line holography [32-33]. Accordingly, despite the fact that holographic reconstruction can be numerically focused at different depths, sectioning of planes closer than e.g.  $\sim 50 \text{ }\mu\text{m}$  has not been feasible with lensfree wide-field holographic microscopes regardless of their detection numerical apertures. [25-31] In this dissertation, this fundamental limitation will be addressed through multi-angle lensfree holographic on-chip microscopy that lends itself to tomographic imaging of the samples within a large volume on a chip.

In recent years, there has also been an increased interest in optical imaging modalities that enable sectional imaging. [34-55] As an example, Optical Projection Tomography (OPT) [34], where an optically cleared specimen immersed in index-matching gel is rotated with respect to the fixed optical path of a conventional lens-based microscope, offers an isotropic resolution of  $\sim 10 \text{ }\mu\text{m}$  in all three dimensions within an imaging volume of up to  $\sim 1 \text{ cm}^3$ . A modified version

of OPT by using high NA objective lenses has also been implemented [35] recently to achieve sub-micron resolution cell imaging over a significantly reduced volume of e.g.,  $<0.0005 \text{ mm}^3$ . Optical Diffraction Tomography (ODT) is another powerful technique where digital holography is utilized to reconstruct the 3D refractive index distribution of the specimen by changing the illumination direction [36-40] or by rotating the object [41]. These tomographic systems can routinely image cells potentially achieving sub-micron resolution in all three dimensions. However the trade-off between resolution and imaging volume also applies to these systems just like conventional microscopy, and high resolution is achieved at the cost of a significantly reduced imaging FOV of e.g.,  $< 0.04\text{-}0.2 \text{ mm}^2$  and a depth-of-field (DOF) of  $<10\text{-}20 \text{ }\mu\text{m}$  depending on the objective lens that is used.

Other tomographic microscopy schemes based on holography have also been developed that do not rely on multi-angle views of the sample. Among these, one can cite Optical Scanning Holography (OSH) that requires a 2D raster scan to obtain 3D images [42], and low-coherence holographic microscopy uses the short coherence length of illumination to achieve sectioning [43,44]. Wavelength scanning has also been used to achieve tomographic microscopy based on digital holography [45,46]. Alternatively, compressive holographic microscopy [47] takes a computational approach that does not rely on multiple images, and can offer improved axial resolution in digital inline holography using a single hologram. Multivariate statistical analysis and feature extraction techniques have also been demonstrated as computational means of achieving 3D imaging from a single-shot hologram recorded using coherent or partially coherent light [48-50].

Moreover, three-dimensional holographic imaging has also been extended to fluorescent imaging modalities through the use of spatial light modulators without the need for mechanical

scanning [51-53]. For the same purpose, light-sheet microscopy techniques (limited to fluorescence imaging) have also been introduced, which utilize a light sheet generated by a cylindrical lens to successively illuminate selective planes within a fluorescent sample [54] to create a 3D image with enhanced axial resolution. SPIM [54], for instance, achieves  $\sim 6 \mu\text{m}$  axial resolution in thick samples up to a few millimeters over an FOV ranging between  $0.04\text{-}2 \text{ mm}^2$ , which is dictated by either the NA of the objective lens that is used or the active area of the optoelectronic sensor array.

In general, the existing optical tomography platforms, some of which are summarized above, rely on relatively costly, complex and bulky optical setups that are challenging to miniaturize and integrate with microfluidic systems. Therefore, an alternative tomographic microscopy platform which offers both high resolution and a large imaging volume in a compact embodiment may offer an important imaging toolset in various fields including cell and developmental biology, neuroscience and drug discovery. Toward this end, here I present a new imaging modality that we termed *lensfree optical tomography* (LOT), [55-59] that achieves  $\sim 0.35 \mu\text{m}$  lateral resolution together with an axial resolution of  $\sim 2 \mu\text{m}$  over a large FOV of  $\sim 20 \text{ mm}^2$  and a depth-of-field (DOF) of  $\sim 0.3 \text{ mm}$ , which could be further increased to e.g.,  $\sim 1\text{-}5 \text{ mm}$  at the cost of reduced spatial resolution. [57,58] As a result, our lensfree optical tomography platform merges high resolution in 3D with a significantly large imaging volume, offering a 3D space-bandwidth product that is unmatched by existing optical computed tomography modalities.

The results presented in this dissertation constitute a number of novelties: (1) optical tomographic imaging has been extended to lensfree on-chip imaging; and (2) dual-axis tomography has been applied to the optical part of the electro-magnetic spectrum; and (3) pixel super-resolution techniques have been applied for optical tomographic imaging. [57] Offering a

decent spatial resolution over a large imaging volume, lensfree optical tomography could in general be quite useful for high-throughput imaging applications in e.g., cell and developmental biology as well as for global health applications where cost-effective and field-portable imaging devices can be desirable

## 2 LENSFREE ON-CHIP HOLOGRAPHIC MICROSCOPY

### 2.1. Basic Principles of Lensfree On-Chip Holographic Microscopy

Lensfree optical tomography is fundamentally based on lensfree on-chip holographic microscopy. Thus, I will first provide a discussion of the working principles of lensfree on-chip holographic microscopy. [25-31] A simple illustration of this on-chip holographic microscopy platform is shown in Figure 2-1.

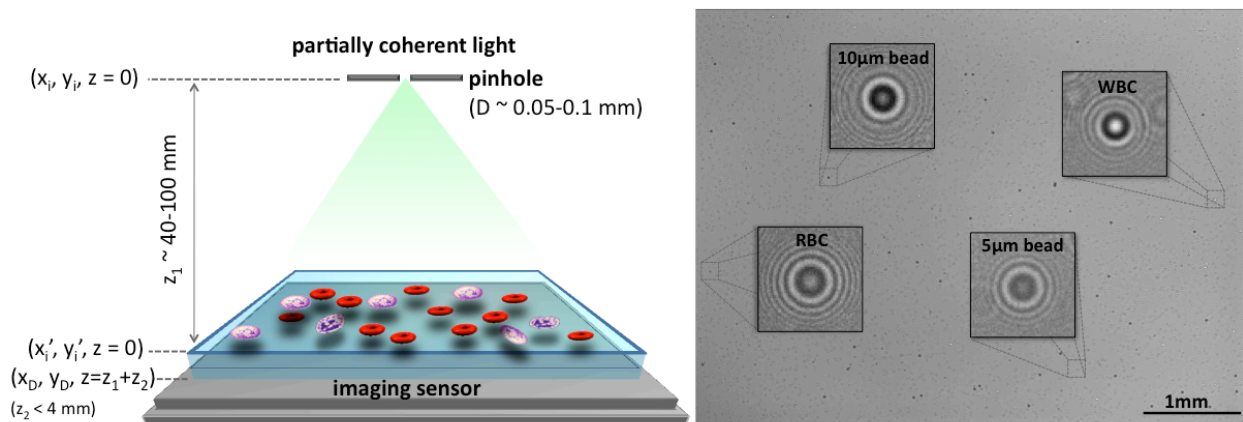


Figure 2-1. (left) schematic diagram of the lensfree on-chip holographic microscopy platform. (right) A full field-of-view holographic image of a heterogeneous sample of spherical micro-particles and blood cells, captured using the system on the left. The holographic image is recorded using a CMOS sensor that has a pixel size of  $2.2 \mu\text{m}$  and a field-of-view of  $24 \text{mm}^2$ .

In this on-chip imaging technique, the sample is directly placed on an optoelectronic sensor array (e.g., a CMOS or CCD chip), and is illuminated with a partially coherent source such as a light emitting diode (LED). The fundamental principle of imaging, as in all digital holography schemes, is to record the interference between the scattered (object wave) and the unperturbed (reference wave) portions of the light as it is transmitted through the sample. This recorded interference pattern encodes the phase information of the object wave in the form of




amplitude oscillations, termed interference fringes. As a result, the recorded intensity image, i.e., the hologram, can be digitally reconstructed to obtain both phase and amplitude information regarding the object wave. Relying on recording the interference between waves, holography inherently requires sufficient coherence between these two wavefronts. To achieve this, traditional in-line holography techniques have employed lasers spatially filtered through small apertures (e.g.,  $\sim 1\text{-}2\ \mu\text{m}$  in diameter). [60,61] In the partially coherent lensfree holography scheme, however, partially coherent sources such as LEDs that are filtered through unusually large apertures (e.g.,  $0.05\text{-}0.1\ \text{mm}$  in diameter) are utilized. Together with using simple low coherence sources emanating through very large apertures, the objects are also brought closer to the sensor, in contrast to traditional in-line holography schemes, such that the pinhole-to-object distance ( $z_1 \sim 50\text{-}100\ \text{mm}$ ) is one or two orders of magnitude larger than the object-to-sensor distance ( $z_2 < 0.5\text{-}4\ \text{mm}$ ).

Propagation over a distance of  $z_1$  enables the incoherent illumination at the aperture plane to acquire sufficient spatial coherence at the sensor plane, so as to permit recording of the interference between the object and the reference waves. In addition to this, the small  $z_2$  distance of our hologram recording scheme also helps us with temporal coherence requirements of our technique such that a relatively wide-band illumination spectrum of e.g.,  $10\text{-}20\ \text{nm}$  can be employed without limiting the achievable spatial resolution. Moreover, this unique geometry also enables using the entire active area of the sensor array as the imaging field-of-view (FOV), significantly increasing the imaging throughput, while at the same time reducing coherent noise terms such as speckle and multiple reflection interference noise originating from air-glass and sample-glass interfaces [25,57] To support the qualitative explanations provided in this section, a

theoretical analysis of hologram formation in partially coherent lensfree holography will be presented next.

It should be noted that the same lensfree on-chip holography setup also lends itself to a color imaging platform, which can be useful for analyzing stained samples such as blood smears, where discerning the color of an object may be desirable. The details of this lensfree color imaging platform are provided in the Appendix 1.

## 2.2 Theoretical Analysis of Lensfree On-Chip Holography

To better understand the hologram formation process for partially coherent illumination, let us assume that two point scatterers (laterally separated by  $2a$  and located at the object plane, i.e.  $z=z_1$ ) with a field transmission of the form  are illuminated vertically, where the amplitudes of the complex coefficients  $c_1$  and  $c_2$  denote the strength of the scattering process, and  $\delta(x,y)$  defines a 2D Dirac-delta function in space. For the same imaging system let us assume that a large aperture (at  $z=0$  plane) having an *arbitrary* shape with a transmission function of  $p(x,y)$  is uniformly illuminated by a spatially incoherent light source. Then, the cross-spectral density at the aperture plane can be written as [25,59,62]:

$$W(x_1, y_1, x_2, y_2, \gamma) = S(\gamma) p(x_1, y_1) \delta(x_1 - x_2) \delta(y_1 - y_2) \quad (2-1)$$

where  $(x_1, y_1)$  and  $(x_2, y_2)$  represents two arbitrary points at  $z=0$ , and  $S(\gamma)$  denotes the power spectrum of the incoherent source with a center wavelength (frequency) of  $\lambda_0(\gamma_0)$ . After free space propagation over a distance of  $z_1$ , the cross-spectral density at  $z=z_1$  (just before interacting with the cells) can be written as [25]:

$$W(\Delta x, \Delta y, q, \gamma) = \frac{S(\gamma)}{(\lambda z_1)^2} e^{-j \frac{2\pi \gamma q}{c z_1}} \iint p(x, y) e^{j \frac{2\pi}{\lambda z_1} (x \Delta x + y \Delta y)} dx dy \quad (2-2)$$


where  $\Delta x = x'_1 - x'_2$ ,  $\Delta y = y'_1 - y'_2$ ,  $q = \frac{x'_1 + x'_2}{2} \Delta x + \frac{y'_1 + y'_2}{2} \Delta y$ ;  $(x'_1, y'_1)$  and  $(x'_2, y'_2)$  represent two arbitrary points on the object plane. After interacting with the objects, the cross-spectral density right after the object plane becomes  $W(\Delta x, \Delta y, q, \gamma) \cdot t^*(x'_1, y'_1) \cdot t(x'_2, y'_2)$ , which further propagates a distance of  $z_2$  toward the detector plane, which is at  $z = z_1 + z_2$ . Thus, the cross-spectral density at the detector plane is given by:

$$W(x_{D1}, y_{D1}, x_{D2}, y_{D2}, \gamma) = \iint \iint W(\Delta x, \Delta y, q, \gamma) t^*(x'_1, y'_1) t(x'_2, y'_2) h_c^*(x'_1, x_{D1}, y'_1, y_{D1}, \gamma) h_c(x'_2, x_{D2}, y'_2, y_{D2}, \gamma) dx'_1 dy'_1 dx'_2 dy'_2 \quad (2-3)$$

where  $(x_{D1}, y_{D1})$  and  $(x_{D2}, y_{D2})$  define arbitrary points on the detector plane (within the lensfree

hologram region of each object); and  $h_c(x', x_D, y', y_D, \gamma) = \frac{1}{j \lambda z_2} e^{j \frac{2\pi z_2}{\lambda}} e^{j \frac{\pi}{\lambda z_2} [(x' - x_D)^2 + (y' - y_D)^2]}$

At the detector plane,  $(x_D, y_D)$ , the recorded intensity,  $i(x_D, y_D)$  can then be written as

$i(x_D, y_D) = \int W_D(x_D, y_D, x_D, y_D, \gamma) d\gamma$ . Assuming  , the

detected intensity can be decomposed into four main terms, such that

$i(x_D, y_D) = C(x_D, y_D) + I(x_D, y_D) + H_1(x_D, y_D) + H_2(x_D, y_D)$ , where:

$$C(x_D, y_D) = D_0 + \frac{|c_1|^2 S_0}{(\lambda_0 z_1 z_2)^2} \tilde{P}(0, 0) + \frac{|c_2|^2 S_0}{(\lambda_0 z_1 z_2)^2} \tilde{P}(0, 0) \quad (2-4.1)$$

$$I(x_D, y_D) = \frac{c_2 c_1^* S_0}{(\lambda_0 z_1 z_2)^2} \tilde{P}\left(\frac{2a}{\lambda_0 z_1}, 0\right) e^{j \frac{4\pi a x_D}{\lambda_0 z_2}} + c.c. \quad (2-4.2)$$

$$H_1(x_D, y_D) = \frac{S_0}{(\lambda_0 z_1)^2} [c_1 \cdot \{p(-x_D \cdot M + a \cdot M \cdot F, -y_D \cdot M) * h_c(x_D, y_D)\} + c.c.] \quad (2-4.3)$$

$$H_2(x_D, y_D) = \frac{S_0}{(\lambda_0 z_1)^2} [c_2 \cdot \{p(-x_D \cdot M - a \cdot M \cdot F, -y_D \cdot M) * h_c(x_D, y_D)\} + c.c.] \quad (2-4.4)$$

In these equations “c.c.” and “\*” refer to the complex conjugate and convolution operations, respectively,  $F = \frac{z_1 + z_2}{z_1}$ ,  $M = \frac{z_1}{z_2}$ , and  $\tilde{P}$  is the 2D spatial Fourier Transform of the arbitrary aperture function  $p(x,y)$ .  $D_0$  represents the background light that does not contain any information regarding the objects, and can be subtracted out digitally. It is rather important to note that  $(x_D, y_D)$  in these equations refers to points within the lensfree in-line hologram extent of an object rather than the entire field-of-view of the detector array. Further,

$$h_c(x_D, y_D) = \frac{1}{j\lambda_0 \cdot F \cdot z_2} e^{j\frac{\pi}{\lambda \cdot F \cdot z_2}(x_D^2 + y_D^2)}$$
, representing the 2D coherent impulse response of free space propagation over an effective distance of  $\Delta z = F \cdot z_2$ . For the incoherent source, we have assumed a center frequency (wavelength) of  $\gamma_0(\lambda_0)$ , where the spectral bandwidth was assumed to be much smaller than  $\lambda_0$  with a power spectrum of  $S(\gamma) \equiv S_0\delta(\gamma - \gamma_0)$ . This approximation can be justified since we typically use incoherent sources (e.g., LEDs) at  $\lambda_0 \sim 500\text{-}650$  nm with a spectral bandwidth of  $\sim 10\text{-}20$  nm.

Equation 2-4.1 describes that the background illumination (term  $D_0$ ) is superposed with the classical diffraction terms (proportional to the strength of self-interference, i.e.  $|c_1|^2$  and  $|c_2|^2$ ) that occur between the object and the detector planes under the paraxial approximation, which is a valid assumption since for this work  $z_1$  and  $z_2$  are typically much longer than the extent of each hologram. Equation 2-4.2 contains the information of the interference between the scattering points located at the object plane. Similar to the self-interference term, this cross-interference term, i.e.,  $I(x_D, y_D)$ , also does ‘not’ contain any useful information as far as holographic reconstruction of the object image is concerned. This interference term is proportional to the amplitude of  $\tilde{P}(\frac{2a}{\lambda_0 z_1}, 0)$ , and since this term will rapidly decay to zero for a large aperture such

as ours, one can estimate that if  $2a > \frac{\lambda_0 z_1}{D}$  (where  $D$  is roughly the aperture width) the scattered fields cannot strongly interfere with each other at the detector plane, which reduces the intensity of this cross-interference term,  $I(x_D, y_D)$ , for objects far apart within our imaging field-of-view.

Equations 2-4.3 and 2-4.4 denote the dominant holographic terms, which represent the interference of the scattered light from each object with the background/reference wave.  $H_1(x_D, y_D)$  and  $H_2(x_D, y_D)$  denote the *holographic* diffraction of the first scatterer,  $c_1\delta(x - a, y)$ , and the second scatterer,  $c_2\delta(x + a, y)$ , respectively. Further inspecting Eqs. 2-4.3 and 2-4.4, we can realize that, for each point scatterer, a scaled (by  $M = \frac{z_1}{z_2}$ ) and shifted (by  $F$ ) version of the aperture function  $p(x, y)$  is convolved with the free space impulse response  $h_c(x_D, y_D)$ , hence coherently diffracts toward the sensor plane with an effective propagation distance of  $\Delta z = F \cdot z_2$ . As  $M$  is typically  $>100$ , the large aperture size effectively shrinks down by  $M$  fold at the object plane to a size of e.g.,  $<500$  nm, and therefore does not significantly degrade the spatial resolution during the hologram recording process. Therefore, for  $M = \frac{z_1}{z_2} \gg 1$ , incoherent illumination through a large aperture is approximately equivalent to coherent illumination of each object individually, as long as the object's diameter is smaller than the coherence diameter ( $D_{coh} \sim \frac{\lambda_0 z_1}{D}$ ), which can be easily satisfied in our hologram recording geometry (see Fig. 2-1).

The derivation discussed above was made for two point scatterers separated by  $2a$ , such that  $c_1\delta(x - a, y) + c_2\delta(x + a, y)$ . The more general form of the partially coherent holographic term (equivalent of Eqs. 2-4.3 and 2-4.4 for a continuous 2D distribution of scatterers) can be expressed as [25,59]:

$$H(x_D, y_D) \propto \frac{S_0}{(\lambda_0 z_1)^2} \left( \frac{z_2}{z_1} \right)^2 \left[ \left\{ s\left(\frac{x_D}{F}, \frac{y_D}{F}\right) * h_c(x_D, y_D) \right\} + c.c. \right] \quad (2-5)$$

where  $S(x_D, y_D)$  refers to the transmitted field after the object of interest, which represents the 2D map of all the scatterers located within the sample. The physical effect of the fringe magnification factor ( $F$ ) on the object hologram can also be visualized in this Eq. 2-5, in harmony with our discussions in the previous paragraphs.

Although multiple in-line holograms are recorded at different illumination angles in lensfree tomographic microscopy, for brevity, the derivation in this section is carried out for vertical illumination case only. Nevertheless, despite the use of tilted illumination angles, the recorded images at each illumination angle are still in-line holograms, and the findings described above apply to all the holograms obtained at varying angles of illumination. As far as the above conclusions are concerned, the most immediate effect of tilted lensfree illumination is the increased  $z_2$  distance. In lensfree optical tomography [57], the illumination is rotated with its center coinciding with the sensor chip. Therefore, the  $z_1$  distance is roughly equal at all angles. Nevertheless, the effective  $z_2$  distance increases by  $1/\cos(\theta)$ , where  $\theta$  is the angle of propagation for the undiffracted wave between the object and the sensor planes. As a result of this, for the largest angle of illumination, e.g.,  $\sim 50^\circ$  in air, the  $z_2$  distance effectively increases by  $\sim 1.3$ - $1.5$  fold, and  $M$  gets slightly smaller. Therefore, the effect of the large aperture becomes slightly more pronounced at large angles. Also, since  $z_1 \gg z_2$  is satisfied at all angles, our unit fringe-magnification geometry is preserved (i.e.,  $F \sim 1$ ), and the imaging FOV is not significantly compromised. Another implication of the increased  $z_2$  distance at larger angles is the elevated need for temporal coherence of illumination, as increased  $z_2$  leads to increased optical path difference between the reference and object waves.

### 2.3. Digital Reconstruction in Lensfree On-Chip Holographic Imaging

Once lensfree in-line holograms are recorded at different directions of illumination, digital reconstruction is necessary to convert these holograms to microscopic images of objects obtained at different viewing angles. For this end, the field at the hologram plane, whose phase is unknown, is digitally propagated back towards the object. Digital beam propagation is achieved using the angular spectrum approach [25,63] that convolves an optical field with the impulse response of free space propagation. In the angular spectrum approach, this convolution is performed in the frequency domain, involving two fast Fourier transforms and multiplication with the transfer function of propagation. This transfer function is given by [63]:

$$H_c(f_x, f_y) = \begin{cases} e^{j2\pi \frac{z}{\lambda} (1 - (\lambda f_x)^2 - (\lambda f_y)^2)^{1/2}} & \sqrt{f_x^2 + f_y^2} > \frac{1}{\lambda} \\ 0 & o.w. \end{cases} \quad (2-6)$$

where  $f_x$  and  $f_y$  are spatial frequencies.

The operation of multiplication by the transfer function given by Eq. (2-6) has a simple physical interpretation: The Fourier transformation decomposes the input complex field into its plane-wave components. The spatial frequencies obtained by this transformation are related to the angle of the plane waves by  $f = \sin(\theta)/\lambda$ . That is, each spatial frequency in the Fourier domain represents a plane wave, in the spatial domain, traveling at an angle  $\theta$  with respect to the optical axis. Then, the transfer function, which is simply a unit amplitude phase function, adds the phase due to propagation to every plane wave component of the complex input field. The final inverse Fourier transformation adds the plane waves to reconstitute the output complex field.

As can be seen in Eqs. 2-4.3 and 2-4.4, digital propagation, performed as described above, will undo the effects of the coherent diffraction and the holographic field will converge so

as to form transmission images of the objects (see Figure 2-2). Nevertheless, after this digital back propagation, the “*c.c.*” terms will diverge even further as opposed to forming images, casting a defocused image, termed as the twin-image, overlapping with the real images of the objects. This twin-image can be eliminated by recovering the phase of the hologram, which effectively gets rid of the complex conjugate terms in Eqs. 2-4.3 and 2-4.4. In this iterative phase recovery approach detailed in Refs. 25, 64 and 65, the square-root of the hologram intensity (i.e., the amplitude) is used as the initial guess of the optical field at the sensor plane with zero phase. This initial field is then propagated back-and-forth between the parallel sensor and object planes while the loose size of the objects is used as a constraint for the extent of the real images in these iterations to recover the phase. Once the phase is recovered (typically in 10-15 iterations), the final back-propagation yields a cleaned digital image that is almost entirely free of the twin-image artifact.

In the case of tilted illumination, the amplitude of the hologram first needs to be digitally multiplied by a tilted plane wave, whose angle is determined such that the hologram field converges toward the actual position of the object when back-propagated using the same transfer function of free-space propagation. The iterative phase recovery algorithm described above can then be utilized to reconstruct images without the twin-image artifact. As a result, the projection images of the sample for different viewing angles can be obtained, which is the key to achieve lensfree optical tomographic imaging. The details of holographic reconstruction for oblique angles will be further described in Section 3.2.



## 2.4. Implementation of Pixel Super-Resolution in Lensfree On-Chip Holography

As suggested by Eqs. 2-4.3 and 2-4.4, for a narrow enough  $p(-x_D \cdot M, -y_D \cdot M)$ , the spatial modulation of the holographic term is proportional to  $\sin\left(\frac{\pi}{\lambda_0 F \cdot z_2}(x_D^2 + y_D^2)\right)$ , which signifies a chirped function that oscillates faster with increasing radial distance from the center of the lensfree hologram. Since  $F \sim 1$  in our hologram recording geometry (Fig. 2-1), this chirped function is not magnified or stretched. As a result of this, the pixel size at the sensor-array plays a critical role to properly sample these holographic oscillations, making the pixel size an important factor determining the achievable spatial resolution.

By employing pixel super-resolution (PSR) techniques [29,31,68,69], however, this pixel size limit is circumvented to achieve deeply sub-micron spatial resolution despite the use of a sensor array with e.g., 1.12  $\mu\text{m}$  or 2.2  $\mu\text{m}$  pixel size. As a result, lensfree on-chip holography with PSR achieves relatively high-resolution without trading off the FOV, in contrast to conventional lens-based microscopes. Utilizing PSR techniques is also critical for lensfree optical tomography as it enables reconstruction of pixel super-resolved (SR) projection images for each viewing angle, which ultimately translates to enhanced lateral and axial resolution.

To implement PSR for a given viewing angle, multiple holograms that are slightly shifted with respect to each other are recorded at a given illumination angle [29,57]. The high-frequency spatial oscillations that are above the noise limit appear to be aliased in each lower-resolution (LR) raw lensfree hologram. The function of PSR is to output a SR hologram where this spatial undersampling is resolved by using the information from all the shifted LR lensfree holograms. To record these shifted LR holograms, the objects themselves can be shifted over the sensor array [56,66], the aperture can be physically translated [29] or alternatively multiple apertures

can be placed at different positions [67], all of which can sufficiently shift the lensfree holograms with respect to each other to achieve PSR. The exact amounts of these shifts are not critical, as almost random shifts can perform equally well. This brings a critical flexibility to lensfree on-chip holography for convenient implementation of PSR, even in field-portable compact telemedicine microscopes [55,67] without using e.g., precise motorized stages.

The first step to digitally achieve PSR is to calculate (with no prior knowledge) the shifts of LR raw holograms with respect to each other using gradient-based iterative shift estimation methods [29]. After this shift estimation, a single SR hologram can be iteratively calculated as detailed in Ref. 29, where a cost-function is defined as the square of the absolute error between the target SR hologram and all the measured LR raw holograms. That is, the synthesized SR hologram needs to be consistent with the LR lensfree measurements when properly shifted and downsampled at the detector plane. Once a SR hologram is calculated, it can be digitally reconstructed using the procedures described in Section 2.3.

To demonstrate the spatial resolution enhancement achieved by PSR, Fig. 2-2 shows a measured LR lensfree hologram and a calculated SR hologram. The SR hologram contains high-frequency fringes that are aliased in the LR raw hologram (see Figs. 2-2a and 2-2b). As a result, the digital reconstruction of the SR hologram yields a higher resolution lensfree image as seen in Fig. 2-2. In lensfree optical tomography of this dissertation, PSR is separately implemented for all illumination angles such that all the projection images input to the tomographic reconstruction algorithm are individually pixel super-resolved, enabling high-resolution tomographic microscopy on a chip.

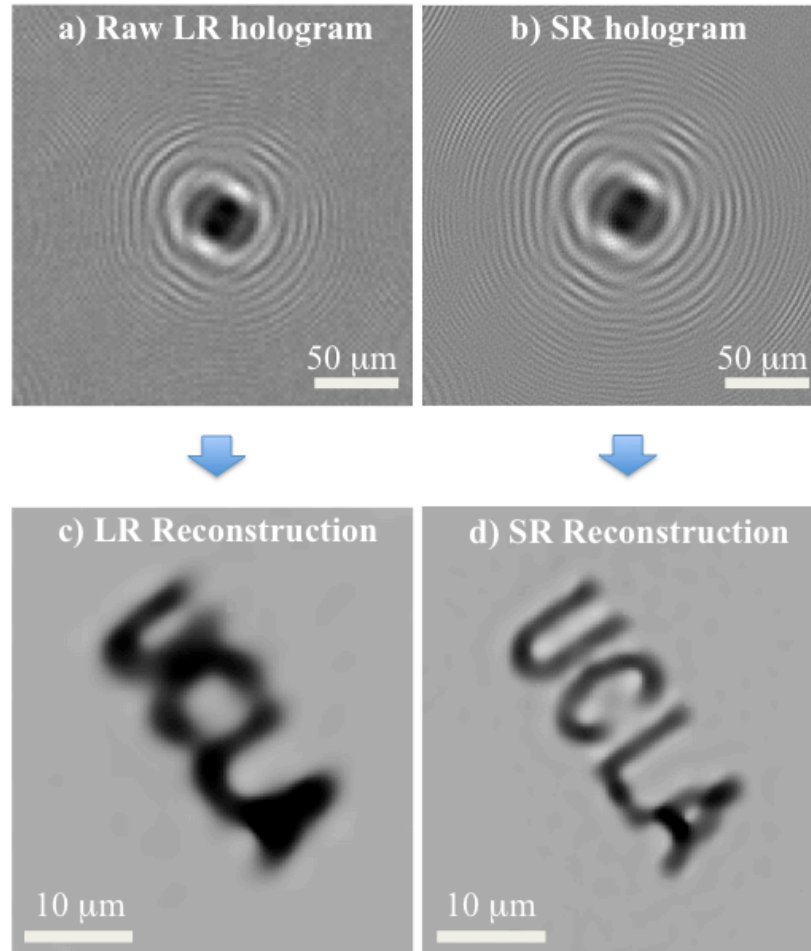


Figure 2-2 (a) Shows a recorded lower-resolution (LR) hologram of a “UCLA” pattern etched on glass using focused-ion beam (FIB) milling. The aliasing artifacts can be observed in the fringes away from the hologram center. (b) Shows the pixel super-resolved (SR) hologram synthesized by using multiple (~15-20) slightly shifted LR holograms, one of which is shown in (a). (c) and (d) show the reconstructed phase images using the LR and SR holograms, respectively. [59]

## 3 LENSFREE OPTICAL TOMOGRAPHY

### 3.1 Introduction

Digital holographic reconstruction enables propagating (digitally) a wavefront to different planes, and therefore different depths along the optic-axis can in principle be reconstructed to obtain 3D imaging of a volume using a single 2D holographic image. Nevertheless, holography cannot be considered a truly tomographic imaging modality owing to its low axial-resolution [70-72]. Particularly for in-line holography, the axial-resolution is practically a strong function of the object size. That is, depth-of-focus (DOF) is in general comparable to the far-field distance of a particle, which is proportional to  $s^2/\lambda$ , where  $s$  is the particle diameter and  $\lambda$  is the wavelength of illumination [72]. Lensfree on-chip holography, as discussed earlier, is also subject to these limitations in axial-resolution. To better illustrate this, Fig. 3-1 shows cross-section images obtained by digitally reconstructing a LR and a pixel super-resolved (SR) hologram of a micro-particle having a diameter of 2  $\mu\text{m}$ . For this experiment, a relatively earlier lensfree imaging setup was used that offers  $<1 \mu\text{m}$  lateral resolution. [29,57] It can be seen from the images in the x-y plane that pixel super-resolution (PSR) improves the lateral resolution to sub-micrometer range. Despite this relatively high resolution, the cross-section images in the x-z and y-z planes reveal significant elongation, which is a manifestation of low axial resolution provided by holographic reconstruction. The full-width-at-half-maximum (FWHM) values of the axial line profiles were also measured as  $\sim 90 \mu\text{m}$  when a single LR lensfree hologram is used for reconstruction, and it is reduced down to only  $\sim 45 \mu\text{m}$  using a SR lensfree hologram [57]. Thus, lensfree on-chip holography cannot normally provide satisfactory

sectional images of samples, regardless of its detection numerical aperture (NA), by simply reconstructing a single hologram at different z distances.

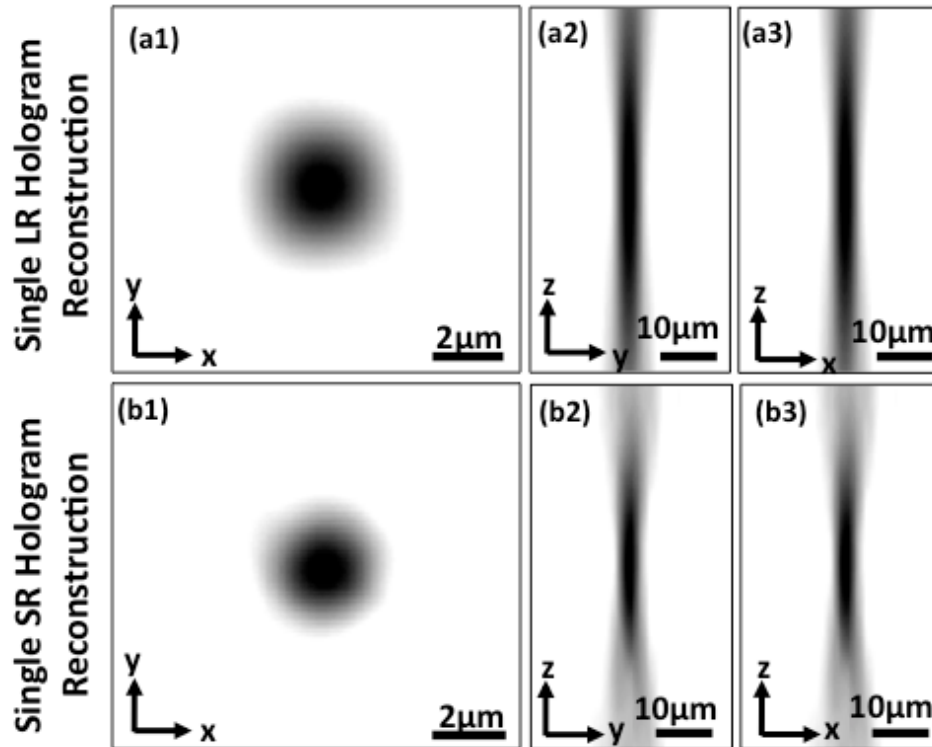


Figure 3-1 (a1-a3) Show slice images (for a micro-sphere with 2  $\mu\text{m}$  diameter) in x-y, y-z and x-z planes, respectively, obtained by reconstructing a raw LR hologram at different depths along the optic axis (z-axis). (b1-b3) Similar to (a1-a3), but obtained by reconstructing an SR hologram of the same micro-particle. [55]

To achieve depth-sectioning using lensfree on-chip holography, we developed lensfree optical tomography (LOT), whose basic configuration is shown in Figure 3-2. [55-59] In its state-of-the-art, LOT offers a 3D spatial resolution of  $<0.35 \mu\text{m} \times <0.35 \mu\text{m} \times \sim 2 \mu\text{m}$  (in x, y and z, respectively) over a large imaging volume of e.g.,  $\sim 5 \text{mm}^3$ . This state-of-the-art system employs a CMOS image sensor with a pixel size of  $1.12 \mu\text{m}$  and a  $z_2$  distance (sample-to-sensor) of  $<300 \mu\text{m}$ . [31,58] There are two key factors that enable achieving this 3D resolution without any lenses and using a sensor-chip with  $2.2 \mu\text{m}$  pixel size: (i) to illuminate the sample from multiple directions to record lensfree in-line holograms at different viewing angles; and (ii) to synthesize separate lensfree SR holograms, using pixel super-resolution (PSR), of the samples

for each illumination angle, obtaining a set of high-resolution projection images of the objects, which are then used to compute tomographic images.

## **3.2 Experimental Methods**

### ***3.2.1 Acquisition of holographic projections***

In lensfree optical tomography, the light source, situated at  $z_1 \sim 70\text{-}80$  mm away from the imaging sensor, provides partially coherent illumination to record inline holograms of the objects, whose distance to the sensor surface ranges between e.g.,  $z_2 = 0.1\text{-}5$  mm depending on the chamber height. (see Figure 3-2) A light source with a center wavelength of  $\sim 450\text{-}550$  nm with a spectral bandwidth of  $\sim 1\text{-}10$  nm is typically used. The choice of the spectral bandwidth of the source affects the temporal coherence properties of illumination, and therefore determines the contrast of high-frequency holographic fringes (which are digitally recovered by the pixel super-resolution algorithm) especially at larger object heights of  $z > 1$  mm above the sensor chip. After being filtered through an aperture of diameter  $\sim 0.1$  mm and propagating over  $z_1$ , the illuminating beam acquires a spatial coherence diameter  $< 0.5\text{-}1$  mm which permits recording the inline holograms of individual objects. [25] In a bench-top system, multi-angle illumination can be achieved by rotating the light source, using a motorized stage, along an arc whose origin is the center of the sensor array. [57,58] It should be noted that, due to our large  $z_1/z_2$  ratio, this alignment is not sensitive and robustness of the setup is maintained. At every illumination angle, a series of sub-pixel shifted holograms are recorded for implementing pixel super-resolution (PSR), which is achieved by linearly translating the light source, using a motorized linear stage, to discrete positions in a  $3 \times 3$  grid in the plane parallel to the sensor surface using step sizes of

$\sim 70 \mu\text{m}$ . Note that because of the large  $z_1/z_2$  ratio, such large shifts at the source plane correspond to sub-pixel shifts at the hologram plane. Since the shifts of holograms are digitally estimated using gradient-based shift estimation algorithms [29], the translation of the light source (or placement of multiple LEDs) does not have to be precisely controlled, nor known *a priori*.

Since most digital sensor arrays are designed to operate in lens-based imaging systems where the angle of incident rays measured from the sensor surface normal does not typically exceed  $\sim 30^\circ$ , the waves incident with large k-vectors are sampled with increased artifacts and reduced SNR. Therefore, even though the detection NA of our system can reach the refractive index of the medium owing to the short  $z_2$ , we have observed that the reconstructed projection images for angles above  $\pm 50^\circ$  exhibit artifacts and including these projections for tomographic reconstruction can deteriorate the final image quality rather than improving it. Consequently, projections are acquired only within a tilt range of  $\pm 50^\circ$ , with  $2^\circ$  angular increments. [57]

As a consequence of the missing angles, the information collected about the micro-objects is limited, which leads to imaging artifacts and lower axial-resolution after tomographic image reconstruction. In order to mitigate these problems, a dual-axis tomography scheme was also adopted. Accordingly, after the completion of recording the projections along one axis, the sensor, with the sample mounted on it, is rotated  $90^\circ$  using a computer controlled rotating stage to record a second set of projections along the orthogonal direction. Although both set of projection holograms, obtained for orthogonal rotations illumination, are limited to  $\pm 50^\circ$ , the dual axis scheme provides more information to the reconstruction algorithm regarding the object's 3D structure. As will be explained in the next sub-section, this additional data set provides significant improvements in tomographic imaging quality. For dual-axis data

acquisition, a custom developed LabView interface is used to automate the data acquisition process and a total of 918 wide FOV lensfree projection holograms are recorded.

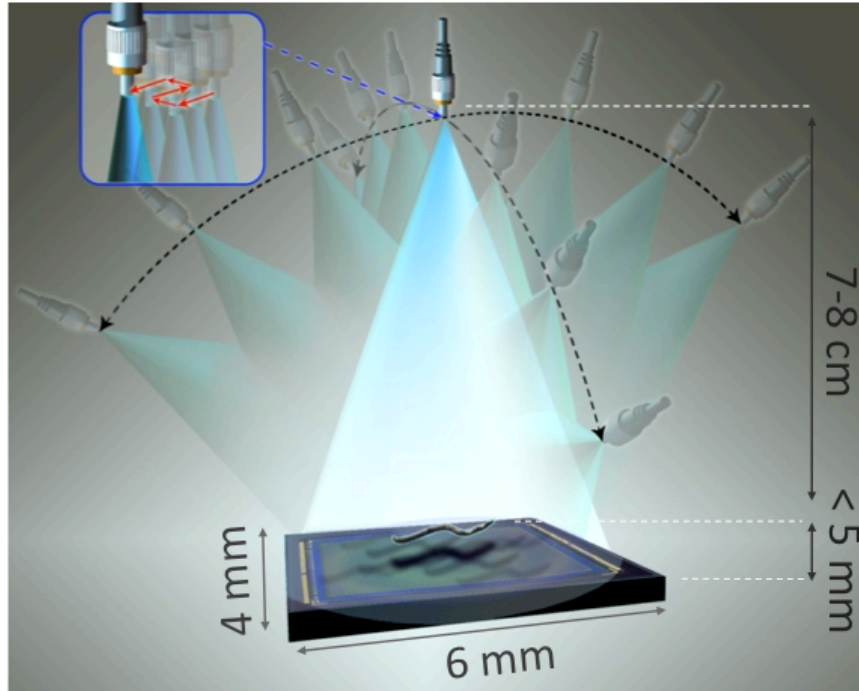


Figure 3-2 Shows the schematic diagram of the lensfree tomography setup. The sample is placed directly on the sensor array with  $< 5\text{ mm}$  distance to the active area. A partially coherent light source with spectral bandwidth of e.g.,  $\sim 1\text{-}10\text{ nm}$  is filtered through a large aperture with diameter  $\sim 0.1\text{ mm}$ . The light source is rotated to record lensfree holograms of the micro-objects from multiple viewing angles. To digitally achieve pixel super-resolution, 9 holograms are recorded, at each angle, by translating the aperture in the plane parallel to the sensor within a  $3\times 3$  grid with discrete shifts of  $\sim 50\text{-}300\mu\text{m}$  (see the inset in (a)). [57]

### ***3.2.2 Reconstruction of the holograms to obtain lensfree projection images***

After recording the projection holograms, PSR is used to obtain one high-resolution (SR) holographic images for each angle of illumination as shown in Fig. 3-4(a-b). Digitally synthesized SR holographic projections are then reconstructed, as described in Chapter 2, to obtain lensfree projection images of the objects at various illumination angles. It should be emphasized that the holograms recorded with oblique illumination angles are still in-line holograms due to co-axial propagation of the scattered object wave and the unperturbed



reference wave toward the sensor array. Consequently, digitally reconstructed images are contaminated by the twin-image artifact, which is a manifestation of the fact that the phase of the complex field in the detector plane is lost during the recording process. In order to obtain faithful projection images, a size-constrained iterative phase recovery algorithm is utilized [25,64,65], which enables recovering the phase of the complex field detected by the sensor. Similar to the conventional vertical illumination case described in Chapter 2, holograms recorded with oblique illumination angles are multiplied with a reference wave that is the digital replica of the reference wave utilized for recording the holograms, which translates to using a plane reference wave tilted with respect to sensor normal. It should be noted that the tilt angle of this reconstruction wave is not equal to the tilt of the illuminating beam, due to refraction of light in the chamber. In fact, the digital reconstruction angle for projection holograms are determined by calculating the inverse tangent of the ratio  $\Delta d/z_2$ , where  $\Delta d$  denotes the lateral shifts of the holograms of objects with respect to their positions in the vertical projection image, and  $z_2$  is either experimentally known, or is iteratively determined by the digital reconstruction distance of the vertical hologram.

For iterative phase recovery, the complex field is digitally propagated back and forth between the parallel detector and object planes. In order to obtain the projection image in the plane normal to the illumination, as in Fig. 3-2(c1-c3), the recovered field is also interpolated on a grid whose dimension along the tilt direction is rescaled by  $\cos(\theta)$ , where  $\theta$  is the angle of digital reconstruction. In addition, the projection images need to be aligned with respect to a common center-of-rotation before computing the tomograms. To achieve that, we implemented an automated two-step cross-correlation based image registration algorithm. Since the projection images obtained with successive illumination angles, e.g.  $50^\circ$  and  $48^\circ$ , are very similar to each

other, the first step of image registration is performed by cross-correlating the projection images obtained at adjacent angles. In most cases, especially when the object is a large connected structure such as *C. elegans* worm, this step yields a successfully registered set of projections. However, if the FOV contains distributed small objects such as beads, the slight differences in projection images due to perspective change, even for adjacent angles, may deteriorate the registration accuracy. In this case the bead at the center of the projection images, which is also assumed to be the center-of-rotation, walks off the center of projection images, indicating poor image registration. Then, a second step of registration is utilized following the first one, where the bead at the center of the vertical projection image is used as a global reference, and all other projection images are automatically aligned with respect to that particular bead. Since the reference bead is already roughly aligned in the first step, the second correlation step is performed only on the reference bead by correlating cropped projection images with the cropped global, i.e. vertical, projection image. Fig. 3-2(c1-c3) shows accurately registered projection images obtained for  $-50^\circ$ ,  $0^\circ$  and  $50^\circ$ .

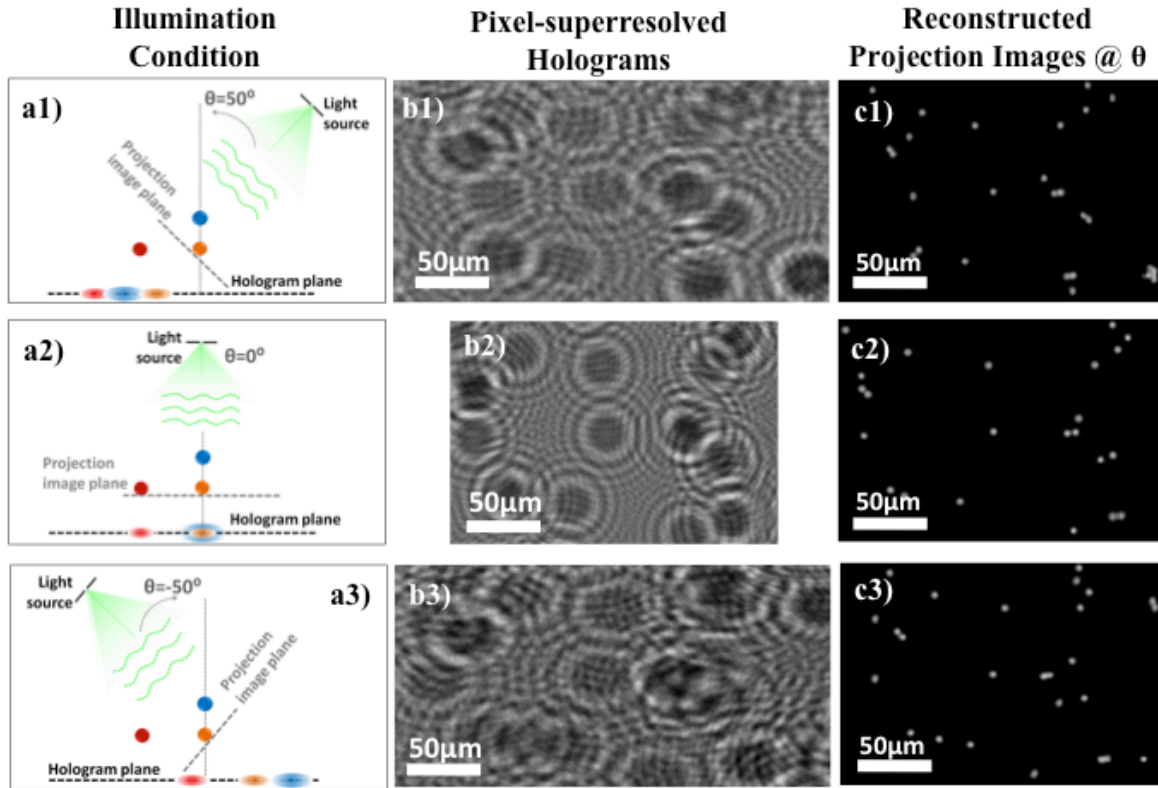


Figure 3-2 (a1-3) Schematic illustration of the holographic recording condition for three angles,  $50^\circ$ ,  $0^\circ$  and  $-50^\circ$ , respectively. (b1-b3) Cropped images from corresponding super-resolved holograms of  $5\mu\text{m}$  beads (at  $z\sim 0.8\text{mm}$ ) measured at illumination angles shown in a1-a3. The holograms of individual beads have an elliptical shape, as expected, since detection plane is not normal to beam propagation. (c1-c3) Digitally reconstructed lensfree projection images using the corresponding holograms in (b1-b3). After perspective correction, the ellipticity is removed as revealed by the circular shape of the reconstructed beads. The reconstructed projection images are registered with respect to the bead at the center of the images, which is assumed to be the center-of-rotation. [57]

### 3.2.3 3D image reconstruction in lensfree optical tomography

Fourier-projection theorem allows reconstructing the 3D transmission function of an object from its 2D projections along different directions. Accordingly, digitally reconstructed lensfree projection images are used to compute 3D tomograms of micro-objects using a filtered back-projection algorithm. [73] A detailed derivation of the filtered back-projection algorithm is also provided in Appendix 2.

A fundamental requirement for this technique, commonly referred to as the “projection assumption”, is that the projection images should represent a linear summation of a certain property of the object, [73] for which tomograms can be computed. It is much easier to satisfy this condition in traditional X-Ray Computed Tomography as X-Ray images represent absorption projections of the objects exhibiting negligible diffraction at that part of the electromagnetic spectrum. On the other hand, computed tomography in the optical regime requires weakly scattering objects. [34,41] Similarly, lensfree optical tomography also requires that the majority of the photons experience at most a single scattering event over the volume of each stack of tomograms. [57] For weakly scattering objects, together with the long depth-of-focus of this system, the scattering potential can be approximated to be additive along the direction of illumination for a tomogram slice thickness of  $\Delta z \sim 50 \mu\text{m}$  (refer to the next subsection on the validity of projection assumption in lensfree optical tomography). Consequently, tomograms of the scattering potential of an object can be computed by applying a filtered back-projection algorithm whose inputs are the projection images calculated by holographic reconstruction of pixel super-resolved lensfree holograms at each illumination angle.


Since holograms are recorded for a limited angular range of  $\pm 50^\circ$ , there is a missing region in the Fourier space of the object, commonly known as the missing wedge. [74,75] The main implication of the missing wedge is reduced axial resolution, which limits the axial resolution to a value larger than the lateral. Further, in the lateral plane, ringing artifacts are observed as well as narrowing of the point-spread function (PSF) along the direction of rotation of the illumination such that the PSF in the x-y plane becomes elliptical. For objects that are close to edges of the sensor, or that are located at a depth  $> 1$  mm above the imaging sensor, the angular range of projection holograms further decreases since holograms of these objects start to

shift out of the active area of the sensor-chip ( $24\text{mm}^2$ ). As a result, the missing wedge further enlarges, leading to a decrease in achievable 3D resolution.

In order to minimize these imaging artifacts, a dual-axis tomography scheme is implemented in this work. Projection images obtained along each tilt direction are separately back-projected to compute two sets of tomograms. These tomograms are merged in Fourier space following the numerical recipe given in Ref. 73. Accordingly, the regions where both sets of tomograms have data for are averaged, while regions where only one set has useful data in its Fourier space, are filled by the data of the corresponding tomograms. As a result, the missing wedge is minimized to a missing pyramid [75], significantly reducing the aforementioned limited angle tomography artifacts. To further reduce the artifacts outside the support of the object, the mask (i.e. prior size information regarding the objects) that is utilized for digital reconstruction (described in Chapter 2) of the vertical projection hologram is applied to all tomograms. The missing wedge could also be iteratively filled to improve resolution and reduce artifacts (although not implemented in this research) by using iterative constraint algorithms based on a priori information of the 3D support or transmission function of the object.

#### ***3.2.4 Validity of the projection assumption for lensfree images of weakly scattering objects***

Assuming that for each one of these tomogram volumes, the weakly scattering object can be represented using a complex scattering function, denoted by  $s(x_\theta, y_\theta, z_\theta)$ , where  $(x_\theta, y_\theta, z_\theta)$  defines a coordinate system whose z-axis is aligned with the illumination angle,  $\theta$ , at a particular projection, then we can ignore the cross-interference among the scattered optical fields arising

from different depth layers or within the same layer. This is a safe assumption in lensfree on-chip holography for two reasons: (1) when compared to the strength of interference of the scattered fields with the unscattered background light, these cross-interference terms are much weaker for a weakly scattering object, i.e.,  $|s(x_\theta, y_\theta, z_\theta)| \ll 1$ ; and (2) the limited temporal and spatial coherence of illumination also spatially gates these cross-interference terms in 3D, further weakening their contribution to the *real holographic heterodyne terms* which only encode the interference of the scattered fields generated by  $s(x_\theta, y_\theta, z_\theta)$  with the unscattered background light. With this in mind, *after successful twin-image elimination (or phase recovery) at each illumination angle*, for each projection image within a single tomogram volume (spanning e.g.,  $\Delta z \sim \pm 25 \mu\text{m}$ ), the reconstructed image contrast will yield the information of , which forms the basis for tomographic reconstruction using a filtered back-projection algorithm. This last equation is further justified by the fact that, regardless of their detection numerical apertures, digital in-line holography schemes in general have a very long depth of focus, as a result of which the scattering coefficients along a given  $z_\theta$  direction can be approximated to become additive for a tomogram slice thickness of  $\Delta z \sim 50 \mu\text{m}$ , satisfying the *projection assumption* of computed tomography, after appropriate twin-image elimination of that particular super-resolved projection hologram at  $\theta$ . Therefore, the reconstructed projection images can be back-projected to compute tomograms of the scattering potential of the objects. This weakly scattering object assumption, however, is shown to cause aberrations in the reconstructed tomographic images for relatively thick objects, and more involved reconstruction schemes have been proposed as a solution, which do not rely on the Born approximation. Implementation of such techniques in lensfree tomographic image reconstruction could further improve these results, which we leave as future work to explore.

### 3.3 Experimental Results

To quantify the lateral resolution of lensfree on-chip holography set-up based that employs a CMOS sensor-array with a pixel size of  $1.12\ \mu\text{m}$ , a grating with  $350\ \text{nm}$  lines etched on glass (i.e.,  $700\ \text{nm}$  period), which was fabricated using focused ion beam (FIB) milling, was used. Fig 3-4.a shows a pixel super-resolved hologram of the grating placed on the imaging sensor.

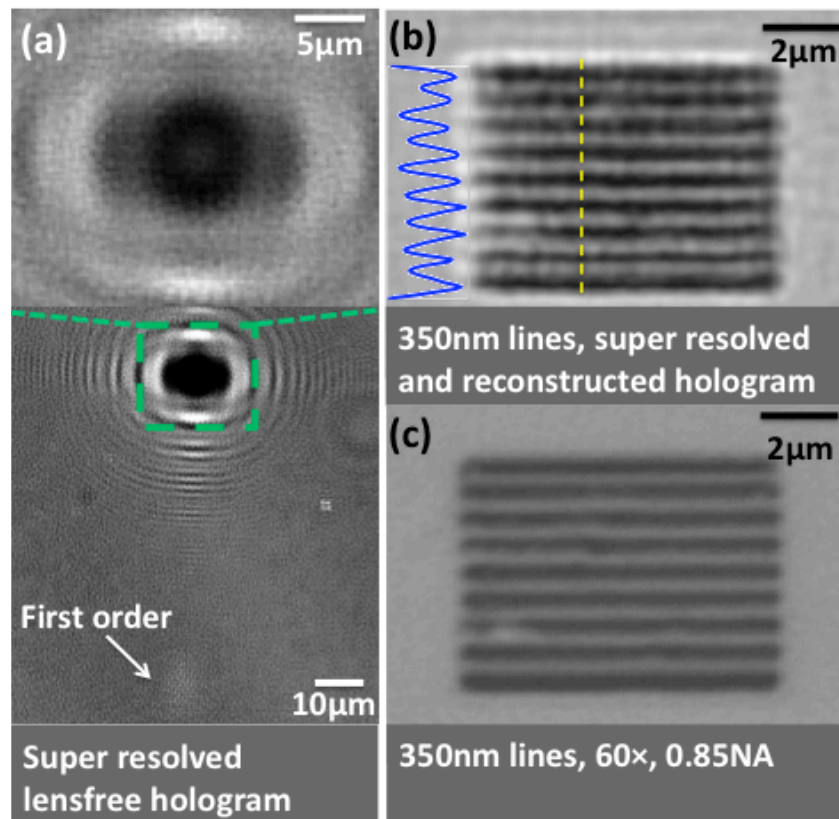


Figure 3-4 (a) Shows a pixel super-resolved (SR) hologram of the grating with  $350\ \text{nm}$  wide lines etched on glass. The fringes on the first diffraction order are now resolved. (b) Shows the lensfree image obtained by reconstructing the SR hologram, demonstrating that the grating lines can be clearly resolved. (c) Shows a bright-field microscope image ( $60\times$ ,  $0.85\text{-NA}$ ) of the same grating for visual comparison. [58]

Despite the fact that the sampling period of the sensor is  $1.12\ \mu\text{m}$ , PSR reduces the effective pixel size, as described in Chapter 2. Consequently, the grating object with a half-period of  $350\ \text{nm}$  could be reconstructed, as shown in Fig. 3-4.b. A conventional bright-field

microscope image ( $60\times$ ,  $0.85\text{-NA}$ ) of the same grating is also provided for comparison (Fig. 3-4.c). This result demonstrates the lateral resolving power of the lensfree on-chip imaging platform is  $< 350\text{ nm}$ , achieving a numerical aperture (NA) of  $\sim 0.8$ .

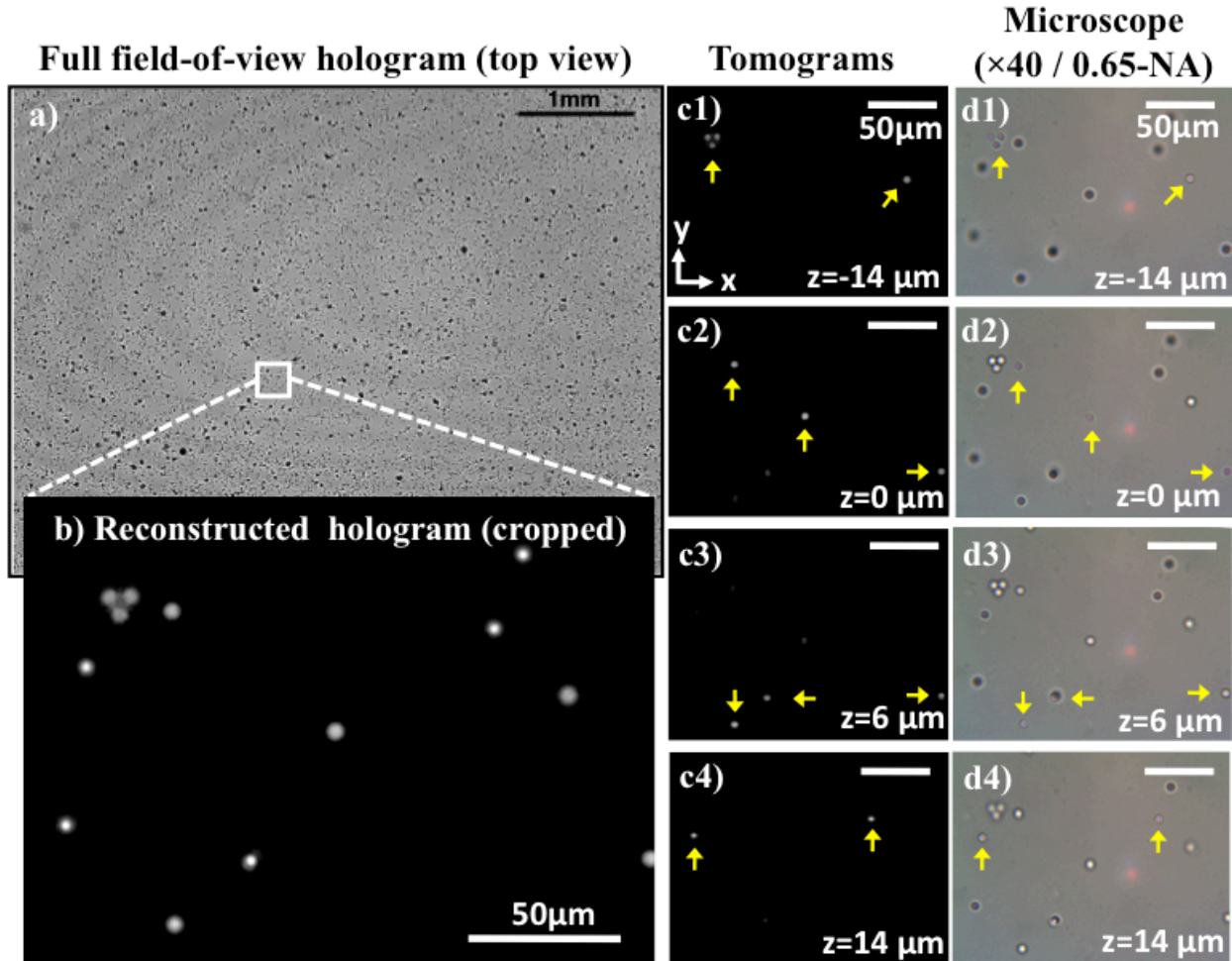


Figure 3-5 (a) Shows a recorded hologram with  $24\text{ mm}^2$  FOV for the case of vertical illumination. (b) Shows the holographic reconstruction for a small region-of-interest within the large imaging FOV, where all the beads appear in-focus. (c1-c4) Shows depth-resolved slice images in the x-y plane for different depths, obtained by tomographic reconstruction. The sectioning results provided by lensfree optical tomography can be compared against the section images in (d1-d4) obtained using a conventional bright-field microscope ( $0.65\text{-NA}$ ). [59]

To demonstrate depth sectioning with lensfree optical tomography, we performed experiments with micro-spheres having  $5\text{ }\mu\text{m}$  diameter, randomly distributed in a chamber with  $\sim 50\text{ }\mu\text{m}$  thickness. This sample was placed directly on the top of the CMOS image sensor to record lensfree holograms with unit fringe magnification as seen in Fig. 3-5a. The distance of the



bottom of the chamber to the sensor surface was  $\sim 0.8$  mm. As seen in Fig. 3-5.b, a regular holographic reconstruction of a region of interest shows all the beads in focus, and it is not possible to discern the micro-particles located at separate layers. After computing the tomographic images as presented in Figs. 3-5(c1-c4), however, the same region of interest can be successfully sectioned, the results of which are also validated against a conventional microscope ( $40\times$  objective-lens with 0.65-NA) as shown in Figs. 3-5(d1-d4). Even though these results are presented for a small region of interest, the data for the entire FOV shown in Fig. 3-5.a is collected in a single data acquisition step, and the entire sample volume can be tomographically imaged. [57,59]

In order to estimate the axial resolution of this platform, spherical micro-particles that have a diameter of  $2\ \mu\text{m}$  were imaged in 3D. To this end, melamine micro-particles (refractive index: 1.68) were randomly distributed in a chamber filled with an optical adhesive gel (refractive index: 1.56). The chamber had a thickness of  $\sim 80\ \mu\text{m}$ . The sample was placed on the CMOS sensor with  $\sim 100\ \mu\text{m}$  distance to its active area for lensfree tomographic imaging. Figures 8.a1-a2 show the cross-sectional images of an arbitrary micro-particle obtained by tomographic reconstruction as described in Section 3.2. While the bead appears circular in the x-y plane passing through its centre, the x-z plane reveals that the bead appears axially elongated (along the z direction). This is a manifestation of the limited angular range that is used in lensfree optical tomography set-up, as a result of which the axial resolution is lower than the lateral. [57]

In order to estimate axial resolution, the line profile through the centre of the bead (along the z direction) was plotted, and its full-width-at-half-maximum (FWHM) value was measured as  $\sim 3.1\ \mu\text{m}$  (Fig. 3-6.c). Moreover, we also calculated the one-dimensional spatial derivative of this axial line profile, which can be used to estimate the edge sharpness of these tomograms [77,78].

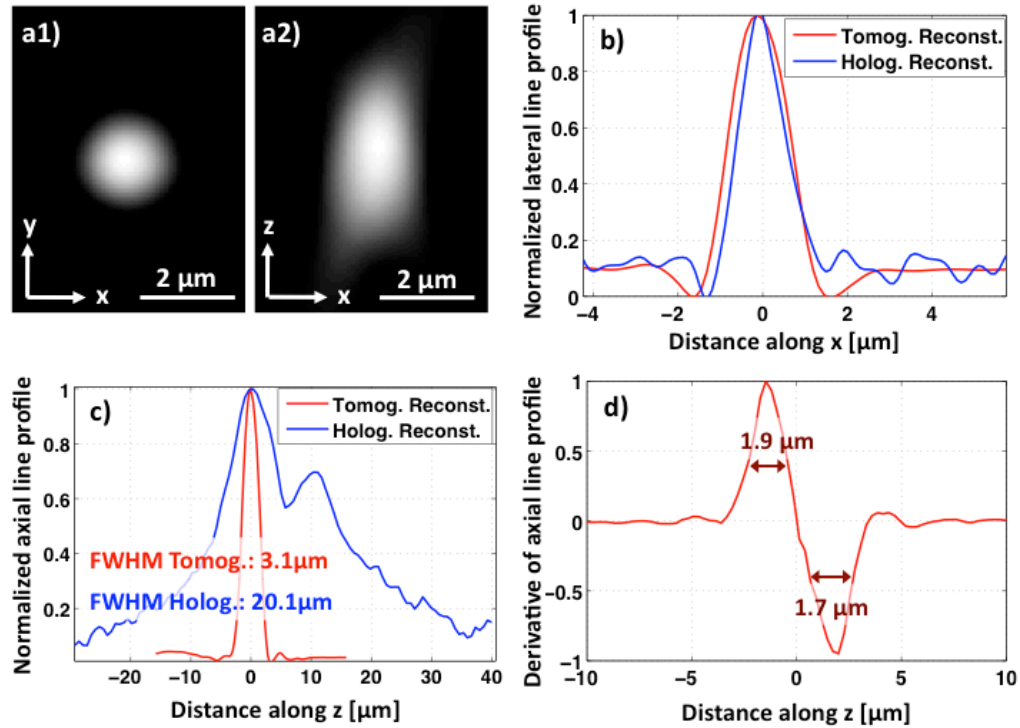


Figure 3-6 (a1) Shows a tomogram in the x-y plane (lateral slice image) through the centre of a micro-particle having a diameter of  $2\mu\text{m}$ . (a2) Shows a tomogram in the x-z plane (ortho-slice image). The axial elongation is a manifestation of the limited angular range used in tomographic reconstruction. (b) Shows line profiles along the x direction through the centre of the micro-particle's tomographic (red curve) and holographic images (blue curve). (c) Shows axial line profiles through the centre of the micro-particle's tomographic (red curve) and holographic images (blue curve). The significant improvement in axial resolution can be observed, as the FWHM of the axial line profile after tomographic reconstruction is much smaller. (d) Shows the derivative of the tomographic axial line profile in (c). Based on this edge response result, an axial resolution of  $\sim 2\mu\text{m}$  can be estimated. [58]

Based on the FWHM values of this spatial derivative plot shown in Fig. 3-6.d, the axial resolution can be estimated to be  $\sim 2\mu\text{m}$ . Due to the relatively lower axial resolution of in-line holography, merely reconstructing a single in-line hologram of the same micro-particle does not provide the same level of axial resolution. As shown in Fig. 3-6.c, the axial line profile obtained by reconstructing a single vertical hologram at different depths exhibits an FWHM value of  $\sim 20\mu\text{m}$ . Therefore, it can be concluded that the multi-angle tomographic imaging approach provides a significant improvement on the sectioning ability of lensfree on-chip microscopy. It is important to note that with a single data acquisition step, a large imaging volume having an area

of e.g.,  $\sim 20.5 \text{ mm}^2$  and a thickness of e.g., 0.3 mm can routinely be probed, while the depth-of-field can be further increased to  $>1 \text{ mm}$  at the cost of reduced spatial resolution, which will be shown next.

In addition to enabling 3D imaging of objects over a wide FOV owing to its lensfree unit-magnification geometry (Fig. 3-2), LOT also enjoys a significantly extended DOF compared to imaging systems where conventional microscope objectives are used. To demonstrate this extended DOF, we imaged a multilayer chamber composed of  $10 \text{ }\mu\text{m}$  beads which has four layers stacked with  $\sim 1 \text{ mm}$  separation, i.e., having a total thickness of  $\sim 3.3 \text{ mm}$ . The chamber is then elevated above the sensor active area, and the furthest layer is situated  $\sim 4 \text{ mm}$  away from the sensor chip. Holographically recorded set of projections for this thick multilayer sample, one of which is illustrated in Figure 3-7(a), comprise the entire 3D volumetric information of the thick sample, and arrows of different colors point to beads located at different layers within the multilayer chamber. One important challenge for tomographic reconstruction of such a large DOF is actually the implementation of pixel super-resolution at each illumination angle.

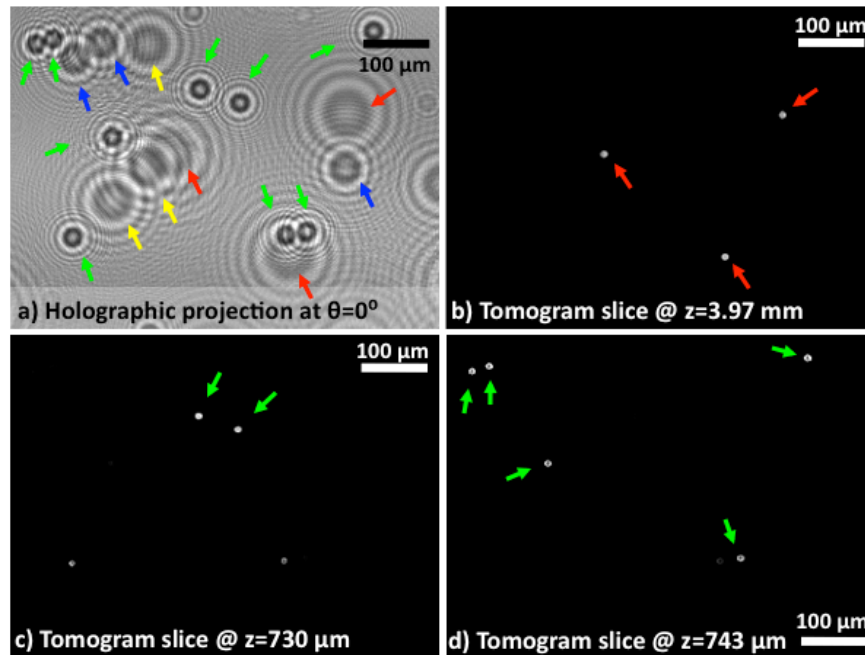


Figure 3-7 (a) Measured hologram of 10 $\mu$ m beads distributed in a 4-layer chamber with total thickness of  $\sim$ 3.3mm. (b) The hologram of beads only in a given layer (e.g., layer 1 located at  $z\sim$ 0.7mm) has been digitally extracted, by reconstructing the measured hologram at the undesired depths, and removing their contribution from the total holographic field. (c) The difference hologram, obtained by subtracting the digitally obtained single-layer hologram from the measured multi-layer hologram, does not exhibit any spurious details, which reveals that the digital extraction process does not introduce artifacts to measured data. This numerical recipe would not have been as successful as demonstrated here for a temporally coherent source (e.g., a laser) since cross-interference between different layers would constitute errors. A broadband partially coherent light source as employed here is advantageous for this technique due to its short coherence length. Note that these results are obtained using an earlier tomography system that employs a sensor with 2.2  $\mu$ m pixel size. [57]

Since the raw holograms of particles/objects that are located at considerably separated depths will create different shifts, if their holograms overlap at the detector plane, blind realization of pixel super-resolution will create errors for at least some of the overlapping particle holograms. Computing the super-resolved holographic projections for axially overlapping objects in thick samples requires additional digital processing due to the fact that the holograms of objects with an axial separation  $>200\text{-}300\mu\text{m}$  shift significantly different amounts over the sensor-chip. As a result, the raw holograms obtained by shifting the light source are essentially different two-dimensional functions rather than translated versions of the same 2D raw

hologram, which is a requirement to be met for pixel super-resolution. Consequently, a single super-resolved projection hologram at a given illumination angle cannot be calculated for the entire sample depth of e.g.,  $>0.2$  mm. Instead, separate super-resolved holograms are calculated for each depth layer. To achieve this, the measured holographic projections (such as the one shown in Figure 3-7(a)) are digitally reconstructed at each depth that is to be deleted, and the reconstructed objects are removed from the hologram field by multiplication with a binary mask, which is zero inside the support of the objects and unity outside. Successively doing this operation for all the layers to be deleted within a thick volume, the digital hologram for only the layer of interest is obtained (see e.g., Figure 3-7(b)). Since the masking operation is applied to undesired layers only, no artifact is introduced to the hologram for the layer of interest, as illustrated by Figure 3-7(c), which shows the difference between the original hologram and the digitally derived hologram for the layer of interest. Once the shifted holograms for a short depth range ( $< 200\text{-}300\mu\text{m}$ ) are digitally obtained, a super-resolved hologram can be calculated specifically for the depth layer of interest. [57] As shown in the reconstructed images (Figs. 3-7(b-d)), an entire DOF of  $\sim 4\text{mm}$  can be sectioned since separate tomograms calculated for a given depth range (e.g.,  $\sim 50\mu\text{m}$  in  $z$ ) are now merged together to obtain a stack of tomograms over an extended DOF.

Next, tomographic imaging quality was quantified as a function of the depth of the object from the sensor-array. For this purpose, tomograms of  $4\mu\text{m}$  diameter opaque micro-particles (made of iron) were acquired at different depths, i.e., at  $z=0.7\text{mm}$ ,  $1.8\text{mm}$ ,  $2.8\text{mm}$  and  $3.8\text{mm}$  from the sensor-chip surface. By using the edge sharpness of the reconstructed particle tomograms, spatial resolution in all three dimensions was estimated as a function of the particle depth, the results of which are summarized in Figure 3-8.

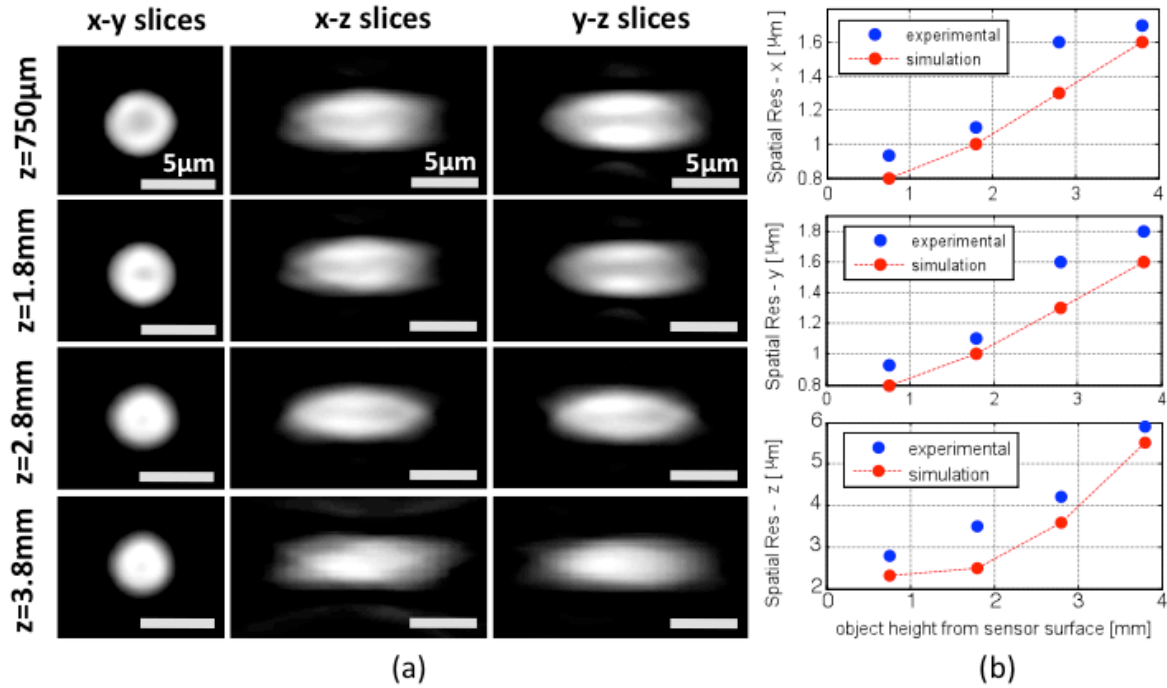


Figure 3-8 (a) shows tomograms for 4 $\mu$ m diameter opaque micro-beads in x-y, y-z and x-z planes, for different axial positions of the objects, i.e.  $z=750\mu\text{m}$ , 1.8mm, 2.8mm and 3.8mm. (b) shows the spatial resolution along the x, y and z dimensions as a function of object height from the sensor surface. Blue markers show experimentally obtained resolution values and red markers connected with dashed lines show the simulation results, which provide the upper limit for achievable resolution. These results reveal that a spatial resolution of  $<1\mu\text{m} \times <1\mu\text{m} \times <3\mu\text{m}$  over a DOF of  $\sim 1$  mm can be achieved using dual-axis tomography scheme; and that the DOF can be further extended to  $\sim 4$ mm at the cost of reduced spatial resolution (e.g.,  $\sim 1.8\mu\text{m} \times \sim 1.8\mu\text{m} \times <6\mu\text{m}$  at a height of  $z\sim 4$ mm). Note that these results are obtained using an earlier tomography system that employs a sensor with 2.2  $\mu\text{m}$  pixel size; hence spatial resolution is lower than the state-of-the-art system that employs a sensor with a pixel size of 1.12  $\mu\text{m}$ . [57]

The same figure also illustrates x-y, y-z and x-z cross-sections of the reconstructed particles that are located at different depths from the sensor-chip. These results also confirm the previous conclusions that a resolution of  $<1\mu\text{m} \times <1\mu\text{m} \times <3\mu\text{m}$  (in x, y and z, respectively) can be achieved up to a DOF of  $\sim 1$ mm. As the depth reaches  $\sim 4$ mm, the resolution of the lensfree tomograms degrades to  $\sim 1.8\mu\text{m} \times \sim 1.8\mu\text{m} \times <6\mu\text{m}$  (see Figure 3-8), which is mainly due to reduced detection SNR at such larger depth values. This point will be further explored in the Discussion Section. Note that these results are obtained using an earlier tomography system that

employs a sensor with 2.2  $\mu\text{m}$  pixel size; hence spatial resolution is lower than the state-of-the-art system that employs a sensor with a pixel size of 1.12  $\mu\text{m}$ .

Providing deeply sub-micron lateral resolution, and micron-scale axial resolution, lensfree optical tomography can be rather useful for biomedical imaging application, e.g. 3D imaging of model organisms for drug development and developmental biology research, where high-throughput is desirable. [79-85] To this end, we also imaged a wild-type *C. elegans* worm in L4 stage ( $\sim 650 \mu\text{m}$  in length) in deionized water. The worm was temporarily immobilized with 4 mM levamisole (Sigma Aldrich L9756) solution to avoid undesired motion during the image acquisition process. Since the worm was aligned parallel to y-axis during data acquisition, only the projections obtained by tilts along the x-axis were utilized to compute the tomograms of the worm, which took  $\sim 4$  min using a single GPU. Fig. 3-9(a) shows a slice through the whole worm corresponding to the  $z=3 \mu\text{m}$  plane. The worm was observed to be slightly tilted out-of-plane with respect to the sensor surface, with its anterior elevated by  $\sim 8 \mu\text{m}$ . Figs. 3-9(b1-b3) show three reconstructed depth sections through the anterior region of the worm at the  $z=2 \mu\text{m}$ ,  $z=8 \mu\text{m}$  and  $z=13 \mu\text{m}$  planes, respectively. As shown in these figures, the pharyngeal tube of the worm, which is a long cylindrical structure with  $< 5 \mu\text{m}$  outer diameter, is clearly visible at the  $z=8 \mu\text{m}$  plane while it quickly disappears at depths away from the center of the pharynx. Figures 3-9(c1-c3) also show the tomograms at different depths through the center and anterior regions of the same worm. Further, Figures 3-9(d1-d2, e1-e2) show its x-z and y-z ortho-slices. In all these results, the appearance of distinct details at different sections can clearly be observed, demonstrating a significantly improved sectioning ability that is otherwise unattainable with wide-field lensfree holographic microscopy, regardless of its detection numerical aperture or coherence properties. Note that the *C. elegans* results presented here are obtained with a previous

generation lensfree optical tomography system that employs a CMOS sensor-array with a pixel size of 2.2  $\mu\text{m}$ .

### **3.4 Discussion**

Lensfree optical tomography (LOT) provides a unique on-chip microscopy modality that can probe a wide FOV of  $\sim 20\text{mm}^2$  and a long DOF of  $\sim 0.3\text{ mm}$  (corresponding to a sample volume of  $>5\text{ mm}^3$ ) at a lateral resolution of  $<350\text{ nm}$  and an axial resolution of  $\sim 2\text{ }\mu\text{m}$ . [58] This makes LOT particularly suitable for high-throughput imaging and screening applications such as 3D model animal imaging. Also note that an extended depth-of-field of  $\sim 4\text{-}5\text{ mm}$  can indeed be imaged by LOT at the cost of a reduction in spatial resolution, as shown in Figures 3-7 and 3-8.



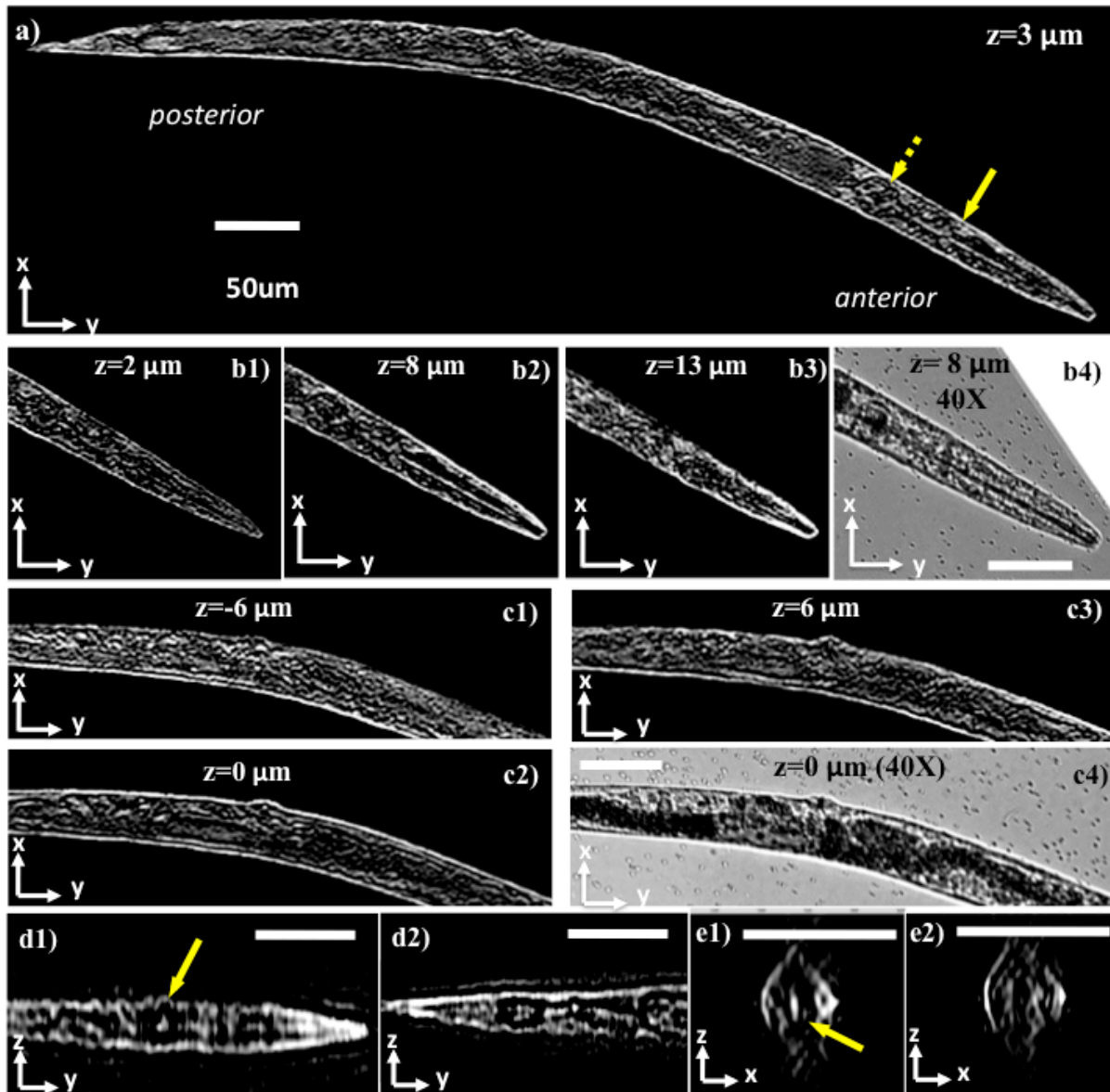


Figure 3-9 Demonstrates the application of lensfree on-chip tomography toward 3D imaging of *C. Elegans*. (a) shows a tomogram for the entire worm corresponding to a plane that is  $3\mu\text{m}$  above the center of the worm. (b1-b3) show tomograms at different layers for the anterior of the worm. The pharyngeal tube of the worm, which is a long cylindrical structure with  $<5\mu\text{m}$  outer diameter, is clearly visible at  $z=8\mu\text{m}$  plane, and disappears at outer layers. (b4) shows a microscope image (40X, 0.65NA) for comparison. (c1-c3) show tomograms at different layers for the middle part of the worm, and a microscope image is provided in (c4) for comparison. (d1) and (d2) show y-z ortho slices from the anterior and posterior regions of the worm, respectively. (e1) and (e2) show x-z ortho slices along the direction of the solid and dashed arrow in (a), respectively. The 3D structure of the anterior bulb of the worm, pointed by the solid yellow arrows, can be probed by inspecting (a), (d1) and (d3). All the scale bars are  $50\mu\text{m}$ . [57]

There are several unique aspects of this lensfree incoherent holography scheme that enable achieving on-chip tomographic imaging over such a wide FOV and an extended DOF.

For instance, choosing a large  $z_1/z_2$  ratio of  $\sim 20-100$  allows holographic imaging with unit fringe magnification, which brings the large FOV to this imaging modality. The limited hologram resolution dictated by this unit magnification and the pixel-size at the sensor-chip is balanced by a pixel super-resolution approach, which increases the lateral numerical aperture to  $>0.8$  without a trade off in imaging FOV. [31] The same large  $z_1/z_2$  ratio also permits the use of unusually large illumination apertures, which significantly simplifies the illumination end without the need for any light-coupling optics, a sensitive alignment or a trade-off in achievable resolution. As a result, projections are easily acquired by tilting the light source rather than having to rotate the object, which would unnecessarily complicate the setup, and perturb the sample. Moreover, the simplicity of the optics and the alignment-free structure of the lensfree setup also permit straightforward implementation of dual-axis tomography.

Another unique aspect of LOT is the use of partially coherent light, both temporally and spatially. The spectral width of the illumination in this technique can be e.g.,  $\sim 1-10\text{nm}$  with a center wavelength of e.g.,  $\sim 450-650\text{nm}$ , which limits the coherence length to be on the order of  $\sim 20-350\mu\text{m}$ . This relatively short coherence length of the technique significantly reduces two major sources of noise, i.e., the speckle and multiple-reflection interference noise terms. The latter one would especially have been a nuisance under laser illumination at oblique angles. In addition, such a limited coherence length also partially eliminates the cross-talk of different depths with each other. Such cross-interference terms are undesired and in fact are entirely ignored in most holographic reconstruction schemes. The same cross-interference also occurs within a given depth layer. In other words, scattering centers within the sample volume actually interfere with each other at the detector plane, which once again is a source of artifact as far as holographic reconstruction (e.g., twin-image elimination) is concerned. The limited spatial

coherence also helps us to mitigate this issue by choosing a spatial coherence diameter (e.g., <math><0.5-1\text{ mm}</math>) that is sufficiently large to record individual holograms of the objects, and yet that is significantly smaller than the entire imaging FOV. This spatial coherence diameter is rather straightforward to engineer in this geometry by changing the illumination aperture (e.g., 0.05-0.1mm) as well as by changing the distance between the source aperture and the sample volume.

The extended DOF (up to  $\sim 1-4$  mm) of this platform [57], as shown in Figure 8, is a direct outcome of the lensfree holographic recording geometry, which is not restricted by the limited DOF of high NA objective lenses. Lensfree holographic recording at multiple angles enables digital reconstruction of projection images at any given depth of interest, around which tomograms can be computed. This paves the way to tomographic imaging with an extended DOF (e.g.,  $\sim 1-4\text{ mm}$ ) by combining such tomograms that are separately computed for different depths.

Finally, we should also discuss the limitations of this presented lensfree tomography approach. First, it is restricted to transmission geometry and therefore would be limited in performance by scattering properties of the sample volume. In other words, an extended DOF of  $\sim 4$  mm demonstrated with our instrument should not be confused with the thickness of a continuous scattering object (such as a tissue sample) that can be optically sectioned in transmission mode. In general, determination of the 3D structure of an object from the knowledge of the scattered optical fields requires a weakly scattering object. [86,87] This assumption also forms the basis of our technique in recovering the 3D scattering potential of the objects similar to existing optical tomography platforms. [34-41] Therefore, the bulk of the photons incident on an object should encounter at most a single scattering event before being detected in our transmission holographic imaging geometry. Whether an object satisfies this condition or not depends on the scattering properties of the specimen as much as the total

thickness of its connected structure. [88] A further limitation is that for weakly scattering sub-resolution objects, the detection SNR would limit reconstruction of their weak holograms, especially if they are located at higher depths of e.g.,  $>2$  mm from the sensor-chip. This also partially explains the resolution loss that is observed in Figure 3-7 as the depth increases from 1mm to 4mm, i.e., the SNR of the acquired holograms degrade at longer depth values since the modulation depth of some of the holographic fringes start to get closer to the noise level. Please note that the effect of sample-to-sensor distance on spatial resolution, as shown in Figure 3-7, was explored using a previous generation tomography system that employs a sensor with  $2.2 \mu\text{m}$  pixel size. Therefore, spatial resolution is lower than the numbers quoted earlier for the state-of-the-art system that employs a sensor with a pixel size of  $1.12 \mu\text{m}$ . To combat this issue, active cooling of the detector-array together with an increased illumination power (and reduced integration time) could be used to enhance the SNR and the available dynamic range of the sensor-chip. On a related note, the detection SNR also partially limits the extent that pixel super-resolution algorithms can digitally reduce the effective pixel size at the hologram domain.

Another limitation of LOT is that for objects located within a micro-fluidic chip, uncontrolled motion of the objects within the channel during the image acquisition could degrade the achievable 3D resolution. To deal with this issue, non-invasive immobilization of the objects by using special micro-fluidic trap designs could be utilized. [79] Another method to partially handle such uncontrolled motion of the objects during image acquisition could be digital estimation of their shifts and rotations to accordingly use these estimates in our reconstructions. As will be described in Chapter 5, this has also been implemented in Holographic Opto-fluidic Tomography, [56] where the motion of the objects was utilized to synthesize super-resolved holograms of the flowing sample without an external shift of the source.

## 4 FIELD-PORTABLE LENSFREE TOMOGRAPHIC MICROSCOPE

### 4.1 Introduction

The lensfree optical tomography (LOT) technique presented in Chapter 3 relies on a rather simple architecture. Owing to this architectural simplicity, LOT also lends itself to a compact, cost-effective and field-portable imaging device. Toward this end, here I also demonstrate a portable lensfree tomographic microscope for use in low-resource settings and in lab-on-a-chip applications. This compact and light-weight design, shown in Figure 4-1, is identical to the bench-top setup of Chapter 3, except that: (i) multi-angle illumination is provided by devoting individual LEDs (butt-coupled to multi-mode optical fibers) for each angle instead of mechanically rotating a light source; and (ii) hologram shifts (to implement PSR) are achieved by electromagnetically actuating the tips of the optical fibers using low-cost and small coils and magnets, as opposed to using mechanical stages. This tomographic microscope weighs only ~110 grams and has low power consumption that could enable battery-powered operation in the field. This microscope utilizes a single axis (as opposed to two in the bench-top version) along which the illumination angle is varied, and has  $\sim 4^\circ$  increments between projections (as opposed to  $2^\circ$  in the bench-top version). Therefore, the axial-resolution was limited to  $\sim 7 \mu\text{m}$  in this portable microscope, while sub-micron lateral resolution could still be achieved, over a large imaging volume of  $\sim 20\text{mm}^3$ . Furthermore, this volume can also be extended up to  $\sim 80\text{mm}^3$  (for a depth-of-field of  $\sim 4 \text{mm}$ ) at the cost reduced spatial resolution. Offering a decent spatial resolution over such a large imaging volume, this compact, lightweight ( $\sim 110$  grams) and cost-effective lensfree tomographic microscope could provide a valuable tool for telemedicine and high-throughput imaging applications in remote locations.

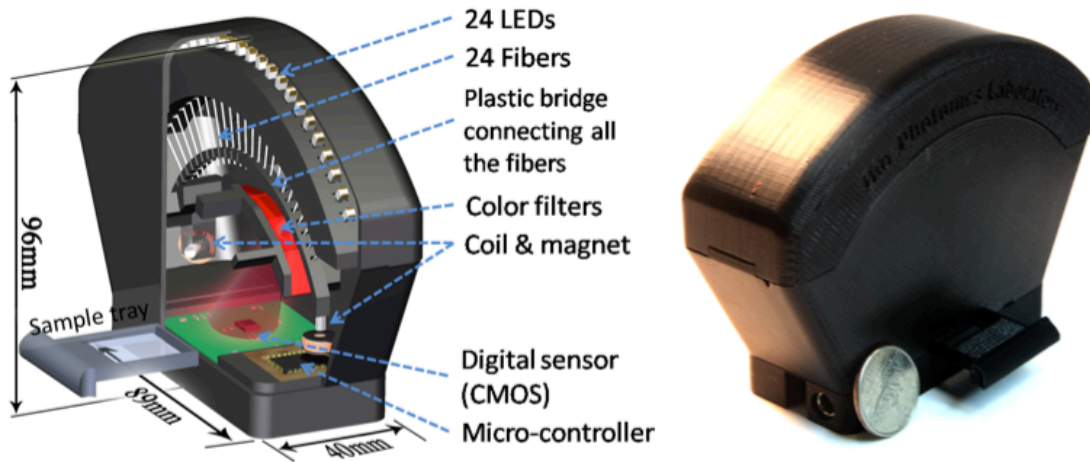


Figure 4-1 (a) Illustrates the field-portable tomographic microscope that weighs only ~110 grams, particularly designed for low-resource settings. Multi-mode optical fibers (with ~0.1 mm core diameter) are electromagnetically actuated to record sub-pixel shifted holograms and achieve pixel super-resolution. (b) A photograph of the field-portable tomographic microscope is shown. [55]

## 4.2 Experimental Methods

For implementation of this tomographic on-chip microscope, 24 light-emitting diodes (LEDs) - each with a cost of <0.3 USD) are used. These LEDs are individually butt-coupled to an array of fiber-optic waveguides tiled along an arc as illustrated in Fig. 4-1.a. In this scheme, since the diameter of each fiber core is ~0.1mm, there is no need for a focusing lens or any other light coupling tool, which makes butt-coupling of each LED to its corresponding fiber-end rather simple and mechanically robust. To increase the temporal coherence of our illumination source, we narrowed the spectrum of the LEDs down to ~10 nm (centered at ~640 nm) using interference based color filters (<50 USD total cost, Edmund Optics) mounted on a piecewise arc that matches the geometry of the fiber-optic array (see Fig. 4-1.a). After this spectral filtering, the coherence length of the illuminating beam increases to ~30 $\mu$ m, which permits obtaining

holograms with a numerical aperture (NA) of  $\sim 0.3-0.4$  up to an object height of  $\sim 1$  mm from the sensor-chip surface.

As illustrated in Fig. 3-2, the sample to be imaged can be placed on a standard coverglass, which is positioned on the top of the sensor array using a sample tray inserted from one side of our portable tomographic microscope. Since the sample is much closer to the active area of the sensor-array ( $<4-5$  mm) compared to its distance to the light source ( $\sim 60$  mm), lensfree holograms of objects can be recorded over a wide FOV of e.g.,  $\sim 24\text{mm}^2$ , which is  $>20$  fold larger than the FOV of e.g., a typical  $10\times$  objective-lens. A low-cost micro-controller is then used to automatically (and sequentially) turn on the LEDs (one at a time) to record lensfree projection holograms of the sample within an angular range of  $\pm 50^\circ$ .

In order to perform pixel super-resolution (PSR) for enhancing our spatial resolution at each illumination angle, the fiber-optic waveguide ends are mechanically displaced by small amounts ( $<500$   $\mu\text{m}$ ) through electromagnetic actuation. In this scheme, the fibers are connected to a common bridge (arc-shaped plastic piece shown in Fig. 3-1a) with low-cost Neodymium magnets (radius: 3.1 mm, length: 6.2 mm) attached on both ends. Compact circular electro-coils (radius: 5 mm, height: 5 mm) are mounted inside the plastic housing, which are used to electromagnetically actuate the magnets, resulting in simultaneous shift of all the fibers along both the x and y directions. Therefore, the entire structure can be modeled as a spring-mass system, where all the fibers collectively act as a spring, and the bridge piece is the mass load.

There are several critical specifications that need to be taken into account for the design of this structure: (1) to keep the form factor of the instrument small, the overall architecture of the actuator should be as compact as possible; (2) the structure should be stiff enough to stay rigid by itself such that small external perturbations do not randomly move the fiber tips during

image acquisition, which would otherwise cause blurring of the recorded holograms; (3) the natural mechanical resonant frequency of the lowest vibrational mode of the structure should be as high as possible such that the structure does not move due to coupling of external vibrations, which also helps the fiber ends to reach the steady-state displacement rapidly without swinging for a long duration; and (4) sufficient actuation should be achieved with reasonable current and voltage values that can be supplied using standard batteries for field use. While (1), (2) and (3) can be achieved by keeping the fibers short, which makes the structure compact and stiff (also increasing the resonant frequencies), this would unfortunately demand a significant increase in the required electromagnetic force, and thereby would result in high electrical power consumption.

To better analyze this mechanical system, we assume a simple model where each fiber-optic waveguide acts as a cantilever beam with a cylindrical cross-section such that the stiffness ( $k$ ) of our structure can be written as [89]:

$$k = \frac{3E\pi r^4}{4L^3} \quad (4-1)$$

where  $E$  is the Young's modulus of the silica fiber ( $=72\text{GPa}$ ),  $r$  is the radius of the fiber ( $r \approx 62.5 \mu\text{m}$ ) and  $L$  is the length of the fibers. In our lensfree tomographic microscope design, we chose a fiber length of  $L = 14 \text{ mm}$ , which is the distance between the plastic bridge to the fixed-end of the fibers. Assuming that these fibers act as parallel springs forming a lumped system of  $N=24$  fibers, we can calculate the mechanical frequency of our structure as:

$$f_0 = \frac{1}{2\pi} \sqrt{\frac{N \cdot k}{m}} \quad (4-2)$$



Equation (4-2) yields an expected value of ~24Hz when we plug-in the measured mass of =1.7 grams for the plastic bridge and the two magnets. According to this calculation, the time to reach the steady-steady displacement for the fibers once a force is applied can be estimated as ~300 ms assuming a quality factor of e.g., ~45. [90] During our experiments we did not observe any undesired swinging of the fiber-array due to external perturbations, and the entire structure is quite robust and sturdy making it suitable for field use.

To achieve electromagnetic actuation of the illumination fibers, we mounted two Neodymium magnets at each end of the plastic bridge. One of these magnets is aligned such that, when a DC current is applied to the coil mounted across it with ~1-2 mm distance, the electromagnetic force moves the fibers along the direction of the arc. The other magnet is placed to generate an orthogonal displacement when its corresponding coil is operated. Therefore, displacements of the fiber-ends in *both x and y* directions can be achieved to generate super-resolved projection holograms of the samples. These coils are placed such that their cylindrical axes are aligned with the magnetization vector of the magnets. In this configuration, the force generated on the magnets ( $F_{mag}$ ) can be calculated as: [91]

$$F_{mag} = S \cdot M \cdot (H_{z1} - H_{z2}) = S \cdot M \cdot \Delta H_z \quad (4-3)$$

where  $S$  is the cylindrical cross-sectional area (in units of  $m^2$ ) of the magnet,  $M$  is the magnetization (in Tesla),  $H_{z1}$  and  $H_{z2}$  (in A/m) are the axial components of the magnetic field intensity at the top and bottom of the magnet, respectively. As Equation (4-3) suggests, the generated force is directly proportional to the magnetic field difference,  $\Delta H_z$  across the two ends of the magnet, and it can be used to pull or push the magnet along the cylindrical axis depending on the polarity of the applied current.

It is quite important to emphasize that the exact amounts of displacement for these fiber-ends do not need to be known beforehand or even be repeatable or accurately controlled. As a matter of fact, the individual displacement of each fiber-end can be digitally calculated using the acquired lensfree hologram sequence. Once the fibers are shifted to a new position by driving the coils with a DC current, a new set of lensfree projection holograms are recorded, each of which is slightly shifted in 2D with respect to the sensor array. A maximum current of 80 mA is required for the largest fiber displacement (i.e.,  $<500\ \mu\text{m}$ ), with  $\sim 4$  volts of potential difference applied across the electro-coil ( $50\ \Omega$ ). Standard alkaline batteries (with a capacity of e.g., 3000 mAh) could be used to actuate the fibers without the need for replacement for at least several days of continuous use of the tomographic microscope.

The digital processing is identical as described in Chapter 3. Accordingly, with the above described set-up, 10-15 projection holograms are recorded at each illumination angle to digitally synthesize one SR hologram for a given illumination angle. These lensfree SR holograms are digitally reconstructed to obtain projection images of the samples, which can then be merged together using a filtered back-projection algorithm [55,57] to compute tomograms of the objects located on the sensor-chip.

### **4.3 Experimental Results**

First, the reconstructed depth ( $z$ ) profiles obtained by reconstruction of the LR and SR holograms were investigated. By digitally reconstructing [25] vertical LR and SR lensfree holograms at several different depth ( $z$ ) values, we obtained the  $y$ - $z$  and  $x$ - $z$  profiles, and analyzed the full-width-at-half-maximum (FWHM) values of axial line profiles, which gives a good indication of the axial resolution achievable by inline holography without multi-angle

based tomography. Accordingly, as shown in Figure 4-2, the full-width-at-half-maximum (FWHM) of the axial line profile for the micro-particle is measured as  $\sim 90 \mu\text{m}$  (for a single LR hologram) and  $\sim 45 \mu\text{m}$  (after pixel super-resolution). Upon tomographic reconstruction, the FWHM is then reduced down to  $\sim 7.8 \mu\text{m}$ . As a result, it is concluded that field-portable tomographic microscope improves the axial resolution by a factor of  $>13\times$  and  $\sim 6\text{-}7\times$  compared to what is achievable with a single LR hologram and a single SR hologram, respectively.

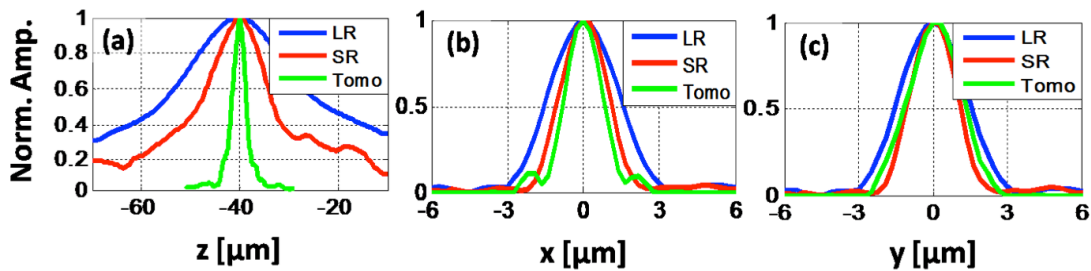


Figure 4-2 (Colour available online only) (a-c) Comparison of the line profiles along x, y and z, respectively, through the centre of a  $2\mu\text{m}$  diameter micro-particle image, obtained by reconstructing a single LR hologram (blue curves), an SR hologram (red curves) and by tomographic reconstruction (green curves). [55]

Also note that, the FWHM of the line profiles along the x and y directions for the computed tomograms, shown by Figs. 4-2(b-c), are  $1.7\mu\text{m}$  and  $2.3\mu\text{m}$ , respectively. The fact that the FWHM value along the x direction is smaller than the diameter of the particle is due to the well-known artifact in limited angle single-axis tomography [74], where the main lobe of the point-spread-function (PSF) gets narrower along the direction of the source tilt. Similarly, the axial elongation of the PSF along the z direction is also partially due to the limited angular range of our illumination (i.e.,  $\pm 50^\circ$ ), which degrades the axial resolution compared to the lateral. These artefacts can be minimized by using iterative back-projection algorithms as well as by using a dual-axis tomography scheme where two sets of projection images are obtained by tilting the illumination along two orthogonal axes. [75]

To further demonstrate the depth sectioning capability of our field-portable lensfree tomographic microscope, depth sectioning of a thick sample of 5  $\mu\text{m}$  diameter spherical micro-beads (refractive index  $\sim 1.68$ , Corpuscular Inc.) was imaged. Micro-beads were randomly distributed within a  $\sim 50$   $\mu\text{m}$  thick chamber filled with an optical adhesive (refractive index  $\sim 1.52$ , Norland NOA65). Fig. 4-3 shows the tomographic reconstruction results for a small region of interest that is digitally cropped from a much larger image area to match the FOV of a 40 $\times$  objective lens (NA: 0.65) that is used for comparison purposes. These lensfree tomograms for the entire chamber depth were computed within  $<1$  min using a Graphics Processing Unit (NVidia, Geforce GTX 480). Arrows in Figs. 4-3(b1-b5) indicate micro-beads that are in focus at the corresponding depth layer of the image, which can also be cross validated using conventional microscope images that are acquired at the same depths as shown in Figs. 4-3(a1-a5). To further quantify our tomographic imaging performance, in Fig. 4-3.c we show x and y line profiles for an arbitrary micro-bead located within the same FOV, where the full-width-at-half-maximum (FWHM) of the particle can be calculated as  $\sim 5$   $\mu\text{m}$  and  $\sim 5.5$   $\mu\text{m}$  along x and y directions, respectively, very well matching with its diameter (5  $\mu\text{m}$ ). The axial line-profile of the same bead tomogram (along the z direction) has a FWHM of  $\sim 12.9$   $\mu\text{m}$  as seen in Fig. 4-3.d with the blue curve. It is important to note that, without the use of multi-angle illumination and tomographic digital reconstruction, using just a single SR hologram, the computed image of the same micro-particle would have an axial FWHM of  $>75$   $\mu\text{m}$ , which is expected for an in-line holographic imaging platform due to its long depth of focus. Following a similar approach as in Refs. 77 and 78, by taking one-dimensional spatial derivative of the axial line-profile shown in Fig. 4-3.d (i.e., the blue curve), the FWHM of the point-spread function of our tomographic microscope along the z direction can be estimated to be  $\sim 6$   $\mu\text{m}$  (refer to the red curve in Fig.

14(d)). Although Fig. 4-3 presents sectional images for a small region of interest, tomograms for the entire FOV ( $> 20 \text{ mm}^2$ ) can be computed without a significant change in the imaging performance. [55]

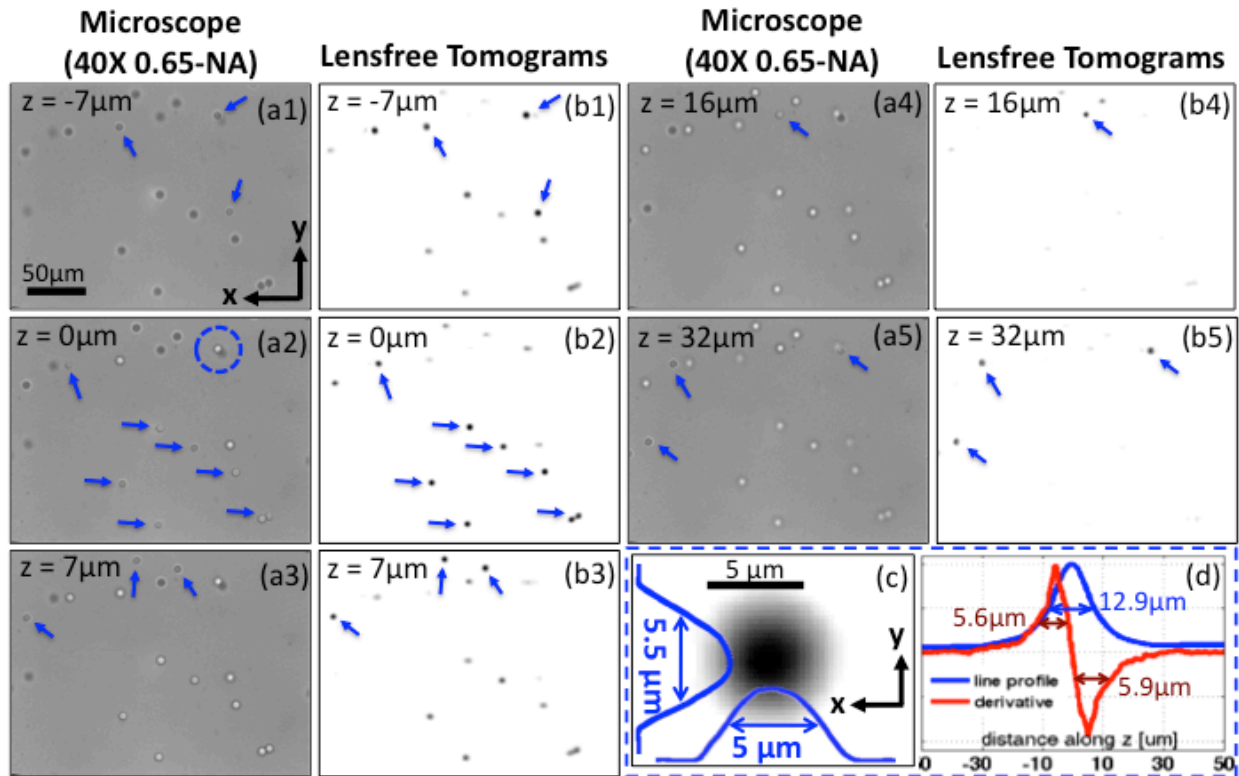


Figure 4-3 (a1-a5) show the microscope images (40X, 0.65-NA) for different depth sections of a chamber filled with randomly distributed micro-beads with  $5 \mu\text{m}$  diameter. (b1-b5) show our lensfree computed tomograms for the corresponding layers, which demonstrate successful depth sectioning with our tomographic microscope. The arrows in each images show the beads that are in-focus at a given depth. (c) shows a zoomed tomographic image through the centre of an arbitrary bead together with its line profiles along x and y. (d) shows the axial line profile and its derivative for the same bead as in (c), suggesting an axial resolution of  $\sim 6 \mu\text{m}$ . The inset in the figure, enclosed with the dashed rectangle, shows sectioning of two axially overlapping micro-beads, shown by the dashed circles in (a1) and (b5), both by lensfree tomography and conventional microscopy (40X, 0.65-NA). Notice that at  $z=12 \mu\text{m}$  plane (shown at the centre of this inset) our lensfree tomographic image does not show anything since  $z=12 \mu\text{m}$  refers to the depth layer that is between the two axially overlapping beads. This provides an independent validation for our significantly improved depth resolving capability. [55]

The field-portable lensfree hologram recording geometry shown in Fig. 4-1 has several advantages especially toward high-throughput imaging needs, achieving both a long depth-of-field (e.g.,  $\sim 1\text{-}4 \text{ mm}$ ) and a wide field-of-view (e.g.,  $> 20 \text{ mm}^2$ ). In specific, lensfree holographic

projections can be reconstructed at any depth of interest; and the tomograms can then be computed around that depth region without introducing spatial aberrations. This approach enables 3D imaging of any arbitrary region of interest within a long depth-of-field and hence a large imaging volume. To specifically demonstrate this capability, we imaged a multilayer chamber (four layers stacked together with  $\sim 1$  mm separation in between, i.e., a total thickness of  $\sim 3.5$  mm) that is composed of  $10\ \mu\text{m}$  beads embedded in an optical adhesive. This thick object is placed at  $\sim 0.7$  mm away from the active area of the sensor-chip with its furthest layer situated at  $\sim 4.2$  mm from the sensor plane (see Figure 4-4(a, b1-b3)). Figures 4-4(c1-c5) show the computed tomograms of different layers within this thick object, which demonstrate optical sectioning capability of our lensfree tomography approach within a long DOF. Tomograms of the entire DOF and the object volume can then be obtained by digitally merging such separate tomograms calculated at different layers. Lensfree holograms of the objects in the furthest layer ( $\sim 4.2$  mm away from the sensor) shift out of the sensor active area for illumination angles above  $40^\circ$  and below  $-40^\circ$ , as a result of which our angular range was limited to  $\pm 40^\circ$  only for the top layer. As described in Chapter 3, a modified PSR algorithm was used for thick sample imaging, where super-resolved holograms are specifically calculated for a given depth layer (independent of the other layers) as illustrated in Figs. 4-4(b1-b3)

And finally, in order to validate the performance of our field-portable lensfree tomographic microscope for potential applications in bio-medicine, we also imaged a *Hymenolepis Nana* (*H. Nana*) egg, which is an infectious parasitic flatworm of humans having an approximately spherical structure with  $\sim 40\ \mu\text{m}$  diameter. Due to the long depth-of-focus of lensfree in-line holography, optical sectioning of this egg is not possible by merely reconstructing its recorded hologram at any given illumination angle. However, as demonstrated in Fig. 4-5, separate depth

sections of this parasite egg can be created using our tomographic handheld microscope (shown in Fig. 4-1), exhibiting distinct details/features at each depth layer.

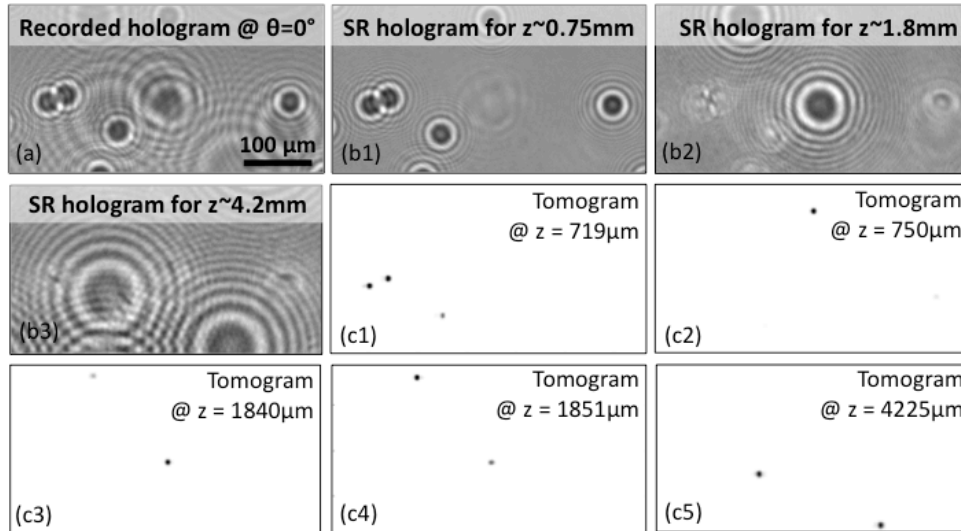


Figure 4-4 Shows the tomographic imaging performance for a multilayer chamber (mounted with 0.7mm elevation above the sensor) of 10µm beads, suspended over 4 layers with a total thickness of ~3.5mm. (a) shows a recorded hologram of this multi-layer object, where the holograms of beads at different depths are visible (with varying sizes as a function of the distance from the sensor-chip). (b1-b3) Digitally cleaned holograms, which comprise the information of objects in only a selected layer, are shown (see the Methods Section for details). (c1-c5) Computed tomograms for different depths are shown to demonstrate depth sectioning over a large DOF of ~4.2mm. [55]

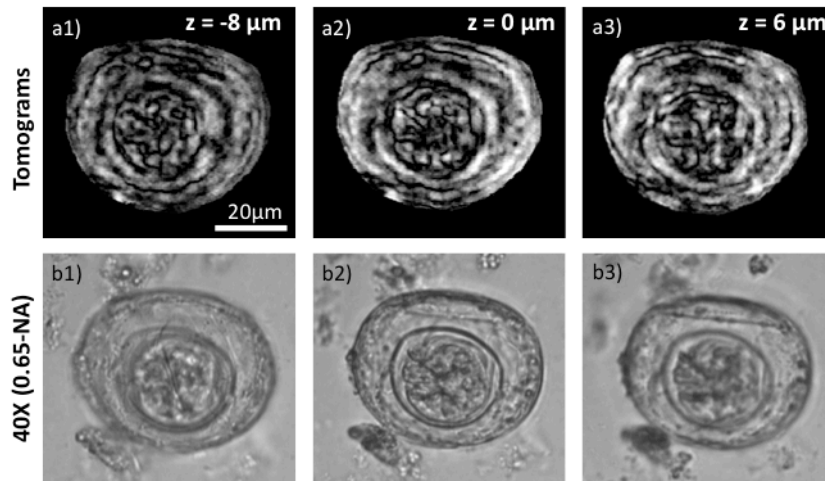


Figure 4-5 (a1-a3) show the computed tomograms for different depths of a *H. Nana* egg, which can also be compared against 40X microscope images shown in (b1-b3). [55]

## 5 OPTOFLUIDIC TOMOGRAPHIC MICROSCOPY

### 5.1 Introduction

The field of opto-fluidics has been growing steadily in recent years due to the great potential lying at the intersection between microfluidics and optics. The integration of microfluidic and optical techniques allows the manipulation of fluids and light in highly integrated, yet compact lab-on-a-chip platforms. Such optofluidic devices could enable sensitive optical interrogation of fluids for biological or chemical detection and sensing, as well as lead the way to tunable and reconfigurable micro-scale optical devices. Some of these recently introduced optofluidic technologies include tunable dye laser, reconfigurable lenses, and flow cytometers [92-96], among others. One other major optofluidic platform that has been added to this emerging set of tools is optical microscopy. [92,93,97-99] Its integration with microfluidic devices would allow the miniaturization and simplification of optical imaging instruments for applications in e.g., telemedicine and global health.

Several attempts have been made to do away with lenses and other bulky optical components to achieve optical imaging within a compact and cost-effective platform. One such approach, termed Opto-Fluidic Microscope (OFM), is based on a slanted array of nano-apertures (e.g.,  $<1 \mu\text{m}$  in diameter) placed at the bottom of a microfluidic channel [98-100]. As an object flows over and in close proximity to these nano-apertures, light is collected from each aperture, and by digitally processing each aperture's intensity signal (through time-to-space conversion) a microscopic image of the specimen within the micro-channel can be synthesized. The major contribution of this work is to get around the pixel size limitation of digital sensors (e.g., CCD or



CMOS chips) through fabrication of sub-micron apertures so that a decent lensfree spatial resolution can be achieved within the optofluidic chip.

The compact and simple architecture of lensfree imaging renders it a very suitable platform for such microfluidic applications. By using simple light sources such as Light Emitting Diodes (LEDs) and no other optical components in this optofluidic microscope, the lensfree hologram of an object flowing within a microfluidic channel can be recorded. In fact, the flow of the object within the micro-channel is utilized for capturing multiple slightly different lensfree holograms of the same object, which allows lateral resolution enhancement using Pixel Super-Resolution (PSR) algorithms. This is an important example of how combining microfluidics with optics can indeed enhance the performance and versatility of a lab-on-a-chip device. In this Chapter, the integration of in-line holography and microfluidics will be explained first. This technique, termed Holographic Optofluidic Microscopy (HOM), [101] is the basis of holographic optofluidic tomography (HOT). Building on the principles of HOM and lensfree optical tomography, HOT will be described next, and experimental results will be provided. [102]

## **5.2 Experimental Methods for Holographic Optofluidic Microscopy (HOM)**

A schematic of the holographic optofluidic microscope (HOM) is shown in Figure 5-1. A microfluidic channel is placed directly atop a CMOS sensor with a pixel size of  $2.2\ \mu\text{m}$  and an FOV of  $24\ \text{mm}^2$ . The channel can be 1-2 mm wide and e.g.,  $80\ \mu\text{m}$  high. Typically, microfluidic channels have smaller cross-sections for better control of the flow, which restricts the size of the objects that can be imaged, and makes the channel susceptible to clogging. In holographic optofluidic microscopy platform, however, the flow need not be uniform in speed or direction. A

light source with a wavelength of e.g., 500-600 nm and a bandwidth of e.g., ~10-15 nm (e.g., an LED) is placed approximately 5 cm away from the micro-channel and is filtered by a large aperture with a diameter of e.g., 100  $\mu\text{m}$ . The large pinhole allows efficient and robust coupling of the light source through the pinhole, while the 5 cm distance to the sample allows the wavefront to develop spatial coherence by the time it reaches the sample, despite being weakly coherent at the pinhole due to the limited spatial coherence of the source.

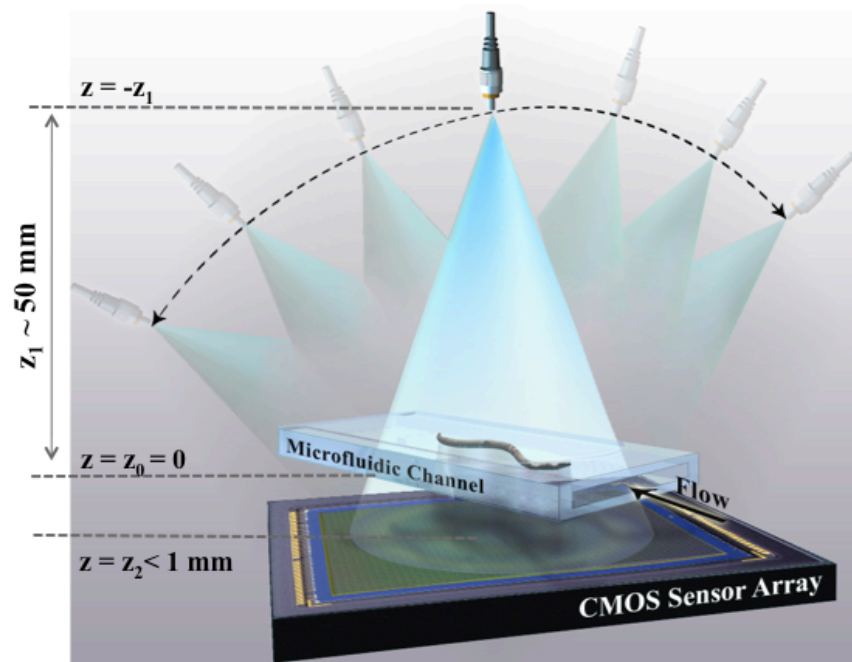


Figure 5-1 Schematic drawing of the holographic optofluidic microscopy and tomography setup. The object to be imaged is placed close to the image sensor, and the illumination aperture is placed several centimeters away. If the object is placed in a microfluidic channel, then multiple shifted lensfree holograms can be captured and processed using PSR algorithms. If the source is rotated, then multiple illumination angles can be adopted to recover a tomographic 3D image of the object. [103]

The flow within the channel can be controlled either by applying an electric field across the channel or by creating a pressure difference between the ends of the channel. Since the object can be tracked directly from its hologram without knowing the details of the flow, the flow need not be uniform. The requirements on the movement of the object to be imaged within the channel are that the hologram is not blurred in a single captured frame (due to motion) and that the object

is rigid and does not rotate out of plane during its flow. The first requirement translates to the requirement that the object moves a distance much smaller than a sensor pixel length within the exposure time of a single frame of the sensor. The exposure time can always be made shorter by using a brighter light source, and does not pose a fundamental limitation. In the figures below, the exposure time of a single frame was  $\sim 50$  ms, and the objects were moving at a speed of 1-2  $\mu\text{m/s}$ , satisfying the above requirements regarding flow speed. The sensor used in our imaging experiments reported below is a 5 Mega-pixels sensor with a pixel size of 2.2  $\mu\text{m}$  and an active area of 24  $\text{mm}^2$ , and was operated at 5 full-frames per second. Note, however, that over a smaller region of interest the same sensor chip can provide more than an order of magnitude faster frame rate, which could help us to significantly increase the flow speed of the objects within the micro-channel, without sacrificing spatial resolution.

As the object is flowing through the channel, its hologram shifts along the sensor plane. The sensor continuously captures frames, each containing a low-resolution lensfree hologram of the object. If a single hologram is processed following the algorithm (as described in Chapter 2), it will recover a microscopic image of the object, but with a lower resolution of e.g., 1.5-2.0  $\mu\text{m}$ . When a higher imaging resolution is desired, the PSR algorithm (described in Chapter 2) can be employed. The shift estimation algorithm discussed above is used to track the movement of the object as it flows through the channel. In Figure 18, the trajectory of the object is tracked for  $\sim 50$  seconds, corresponding to  $\sim 250$  consecutive frames. The microfluidic channel was placed at a small angle with respect to the sensor edges, so that the trajectory has components along both sensor axes (x and y). The flow in this particular case was due to an applied voltage of  $\sim 2\text{V}$  over the length of the channel, approximately 5 cm. The object imaged here is a *C. elegans* worm, a widely studied model organism in life sciences, which has been temporarily paralyzed using a

solution containing Levamisole for achieving rigidity during the imaging period. The velocity of the worm during the imaging period was not constant, as can be seen from the 3 highlighted sets of frames in Figs. 5-2(a-b), each representing 3 seconds of imaging, though the worm covers different distances in each case. The angle estimation (Fig. 5-2(b)) also shows a slow rotation of the worm coinciding with the change of velocity. This irregular flow does not pose challenge for HOM and it is due to the large cross-section of our micro-channel, the surface defects and impurities in the channel, since it was made with simple glass without additional treatment or passivization steps.

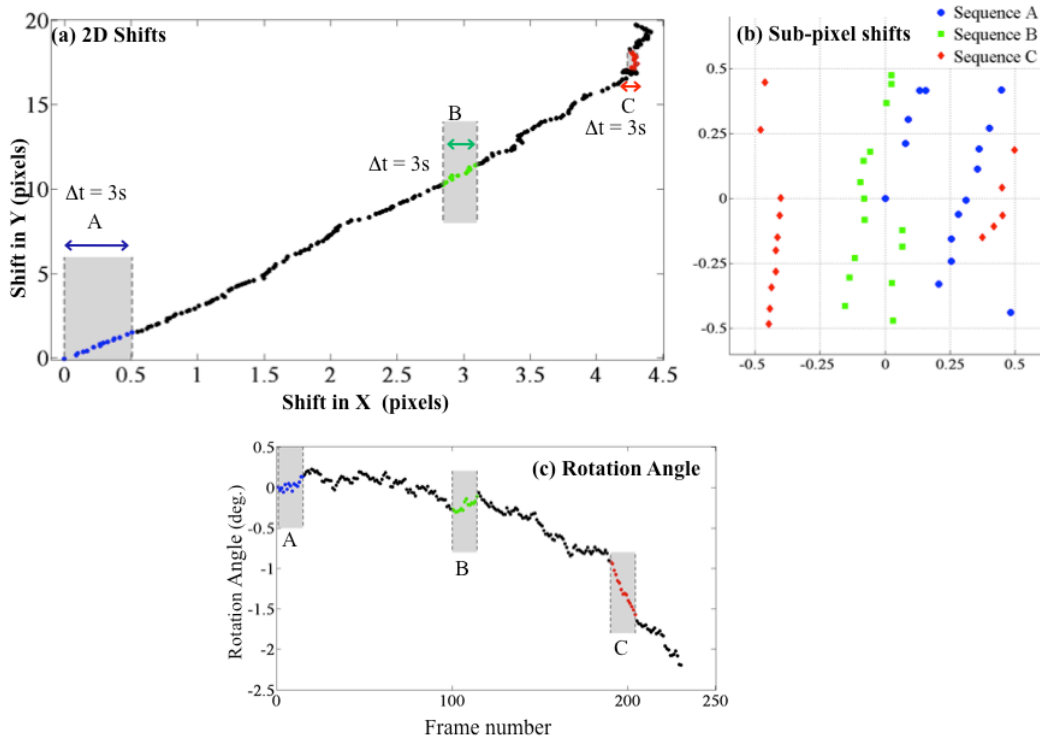


Figure 5-2 As the object flows through a microfluidic channel (due to, e.g., electro-kinetic motion or a pressure gradient) lensfree in-line holograms are captured by a digital sensor-array. Acquisition of  $\sim 15$  consecutive digital frames is sufficient to generate a high-resolution image, but for comparison,  $\sim 230$  frames were captured during  $\sim 45$  s. (a) 2D lateral shifts of consecutive frames with respect to the first one. (b) In-plane rotation angles of consecutive frames with respect to the first one. (c) Sub-pixel shifts of 3 sequences (A, B, and C; each composed of 15 consecutive frames) are shown. These three sequences of lensfree raw holograms are used independently to generate three different microscopic images of the same flowing specimen. [103]

It is also important to emphasize that it is not necessary to track the object for a long period of time. In fact, for the flow conditions described above, it was possible to achieve a decent imaging performance with only 15 consecutive frames, chosen at any random point in the long sequence of frames (see Fig. 5-2). This corresponds to ~3 seconds of imaging time at 5 frames per second, but a faster sensor (or selection of a smaller FOV on the same chip) can scale down the imaging time significantly. Given any 15 consecutive frames, shifts between the frames are estimated, and the integer pixel part of the shifts is discarded. The remaining sub-pixel shifts are shown in Figure 5-2.c, for 3 different sets of 15 frames each.

The PSR algorithm, as discussed earlier, combines a set of 15 shifted lower resolution holograms into a single high-resolution one. PSR processing of a set of low-resolution holograms of the worm shown in Figure 5-3 and Figure 20 took 2.5 seconds to converge running in Matlab on a 3.2GHz PC. The code was also converted to run on a Graphics Processing Unit (GPU), which reduced the processing time by an order of magnitude to 0.25 seconds. In Figure 5-3, the results of PSR are demonstrated and compared to simple interpolation of a single low-resolution hologram. The super-resolved hologram contains interference fringes that cannot be captured with the physical pixel size of the CMOS sensor.

Figure 5-4 demonstrates the imaging capability of HOM. The microscopic image obtained from a single lensfree raw hologram is compared to the image obtained from PSR processing of 15 consecutive frames, and to an image obtained from a traditional bright-field benchtop microscope with a 40× objective lens ( $NA = 0.65$ ). The PSR images show a clear enhancement of spatial resolution over the single frame image, and compare well to the bright-field image obtained with a benchtop microscope. The different sequences (A, B, and C in Fig. 5-4) correspond to different sets of 15 consecutive frames taken from different parts of the larger

set of frames (see Fig. 5-3), and they all compare well to each other. The holographic nature of this microscope also allows phase imaging in addition to amplitude imaging, which is particularly useful for transparent biological samples, which do not absorb or scatter light strongly.

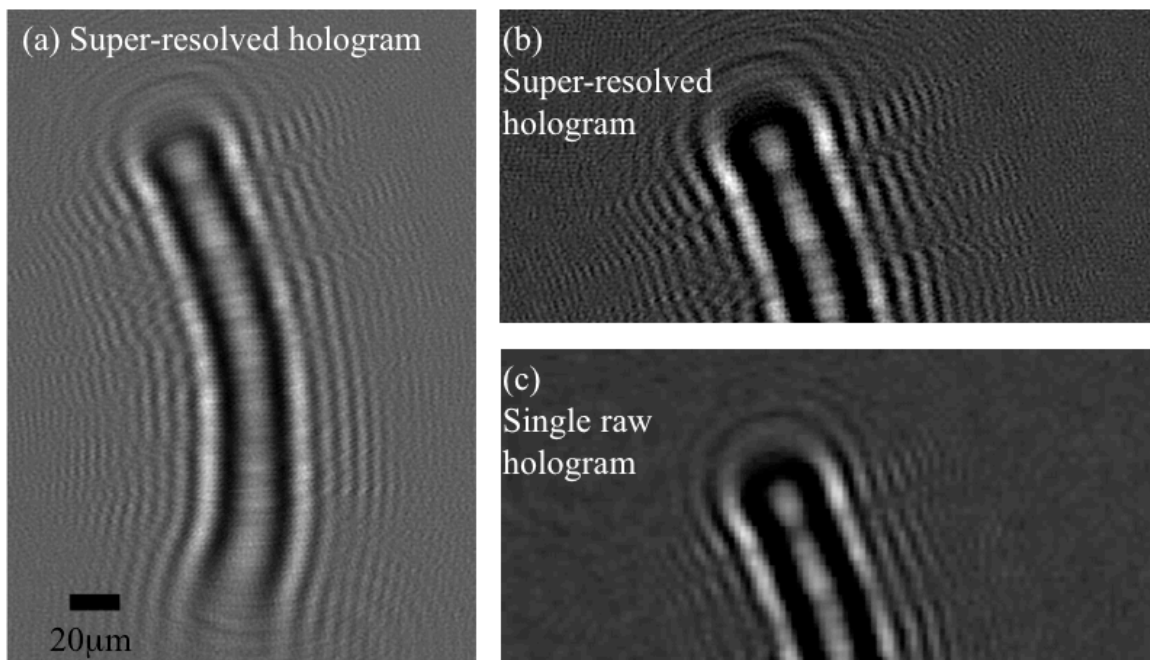


Figure 5-3 (a) A super-resolved hologram of a *C. elegans* sample is shown, synthesized from 15 low-resolution frames, i.e., sequence A of Fig. 5-2.b. An enlarged section of (a), where sub-pixel holographic oscillations are clearly visible. (c) An enlarged section of one of the raw holograms is shown, after interpolation. [103]

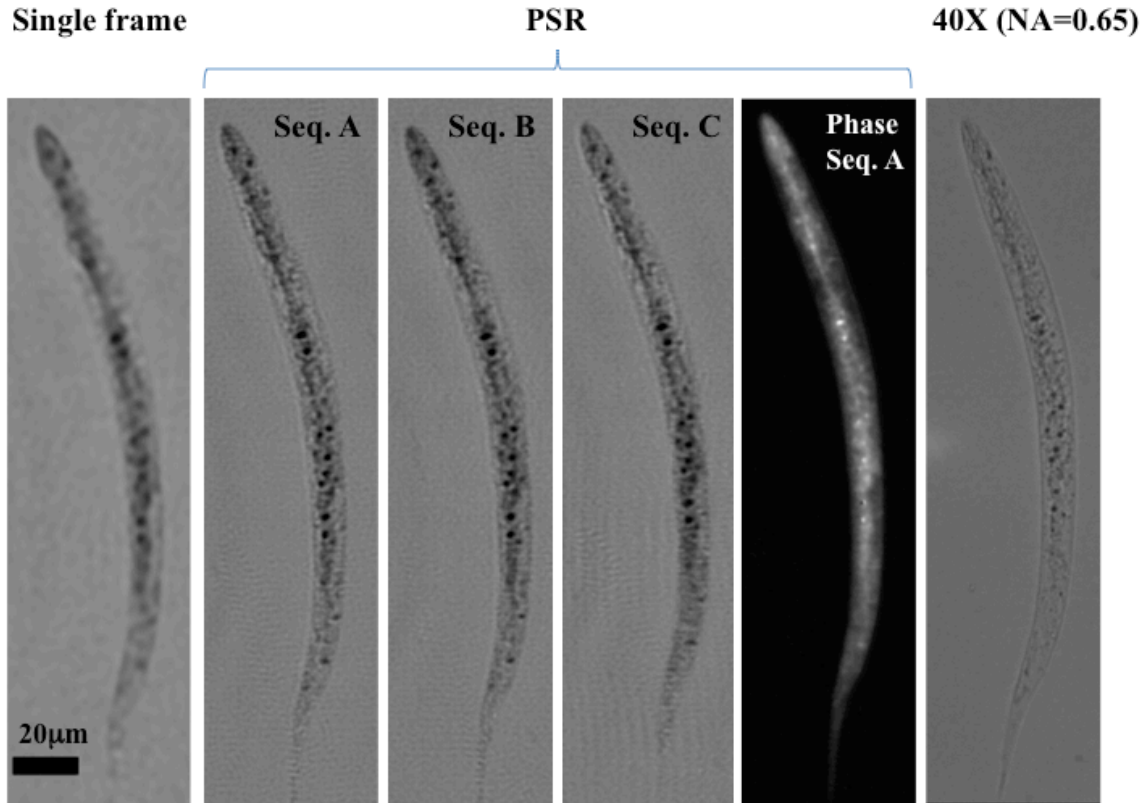


Figure 5-4 HOM images of a *C. elegans* sample are shown. Without PSR, a single low-resolution hologram gives a lower resolution image of the object, as shown in the far left image. When using 15 consecutive holographic frames of sequence A (Fig. 5-2) a super-resolved hologram is synthesized to create higher-resolution amplitude and phase images of the same object. To demonstrate the robustness of this method, two additional sequences (B and C) were independently used to generate similar reconstructed images, all of which match the conventional microscope image of the same worm acquired under a 40× objective lens (NA: 0.65) [103]

The optofluidic microscopy modalities discussed thus far lacks the ability to perform sectional imaging of the specimen. We developed holographic optofluidic tomography (HOT) to provide a new imaging modality for sectional imaging in microfluidic applications [102].

### 5.3 Experimental Methods for Holographic Optofluidic Tomography (HOT)

The imaging principle of holographic optofluidic tomography (HOT) is similar to holographic optofluidic microscopy in the sense that pixel super-resolved images of flowing objects are obtained using lensfree on-chip holography. The key difference is that HOT relies on

multi-angle illumination to record multiple lensfree views of objects that can be used to obtain volumetric structural information (see Figure 5-1). Accordingly, HOT utilizes partially-coherent illumination (e.g., ~600 nm center wavelength with ~10 nm spectral bandwidth, filtered by an aperture of diameter ~0.1 mm) placed ~50 mm away from the sensor array to record digital in-line holograms of the sample. As described in the previous sections, PSR techniques are utilized to digitally generate high-resolution holograms of the objects. Since illumination is provided without any sensitive alignment either with respect to the pinhole or the sensor-array, the architecture of lensfree on-chip holography conveniently permits imaging of the flowing objects using multiple illumination angles as shown in Figure 5-1, which is the key to achieve tomographic optofluidic microscopy on a chip.

In HOT, multiple shifted projection holograms (e.g. 10-15 frames) are recorded at each illumination angle (spanning a range of e.g.,  $\theta = -50^\circ:50^\circ$ ) as the sample is driven through a micro-channel placed on the sensor array. These lower-resolution (LR) lensfree holograms are then digitally synthesized into a single super-resolved (SR) hologram by using the above-mentioned PSR techniques to obtain a higher lateral resolution in the plane parallel to the sensor. These SR projection holograms are digitally reconstructed to obtain projection images of the same object for different viewing directions with a lateral imaging resolution of  $<1 \mu\text{m}$ . For weakly scattering objects that are not thicker than the depth-of-focus of the projection images, these lensfree projection images represent rectilinear summation of the object's transmission function (e.g., scattering strength) along the direction of illumination. In other words, if scattering is not very strong inside an object whose thickness is  $<40\text{-}50\mu\text{m}$  (i.e. the typical depth-of-focus of our lensfree projection images), the diffraction within the object can be ignored, and the projection assumption can be satisfied [57]. Therefore, the 3D transmission function of the



object can be computed using a filtered back-projection algorithm as described in Chapter 3, where all the complex projection images (i.e., 51 super-resolved images for  $\theta = -50^\circ : 2^\circ : 50^\circ$ ) are used as input.

### 5.3 Experimental Results

As a proof of concept for optofluidic tomography, sectional imaging of a wild-type *C. elegans* worm is demonstrated here using HOT. To achieve that, holograms of the worm, flowing through a microfluidic channel, were acquired at various illumination angles spanning  $\theta = -50^\circ : 50^\circ$  in discrete increments of  $2^\circ$ . The main reason for not using larger illumination angles, e.g.  $70^\circ - 80^\circ$  is the degradation in pixel-response for large incidence angles. That is, digital sensors are designed for lens-based imaging systems, where incidence angles do not typically exceed  $20^\circ - 30^\circ$ . Therefore holograms recorded at illumination angles larger than  $\pm 50^\circ$  exhibit significant artifacts and including them in the back-projection process leads to spatial aberrations. For each illumination angle,  $\sim 15$  holographic frames of the flowing object (in  $< 3$  seconds) were recorded, leading to a total imaging time of  $\sim 2.5$  minutes under the electro-kinetic flow condition. The data collected within 2.5 minutes enables tomographic imaging of all the objects that were above the sensor during the data acquisition time. Multi-angle illumination was automatically provided by a computer-controlled rotation stage holding the light source. The center of rotation for the light source was roughly adjusted to coincide with the center of the sensor that is located at the x-y plane. Exemplary LR holograms recorded with this set-up at different illumination angles are illustrated in Figure 5-5.

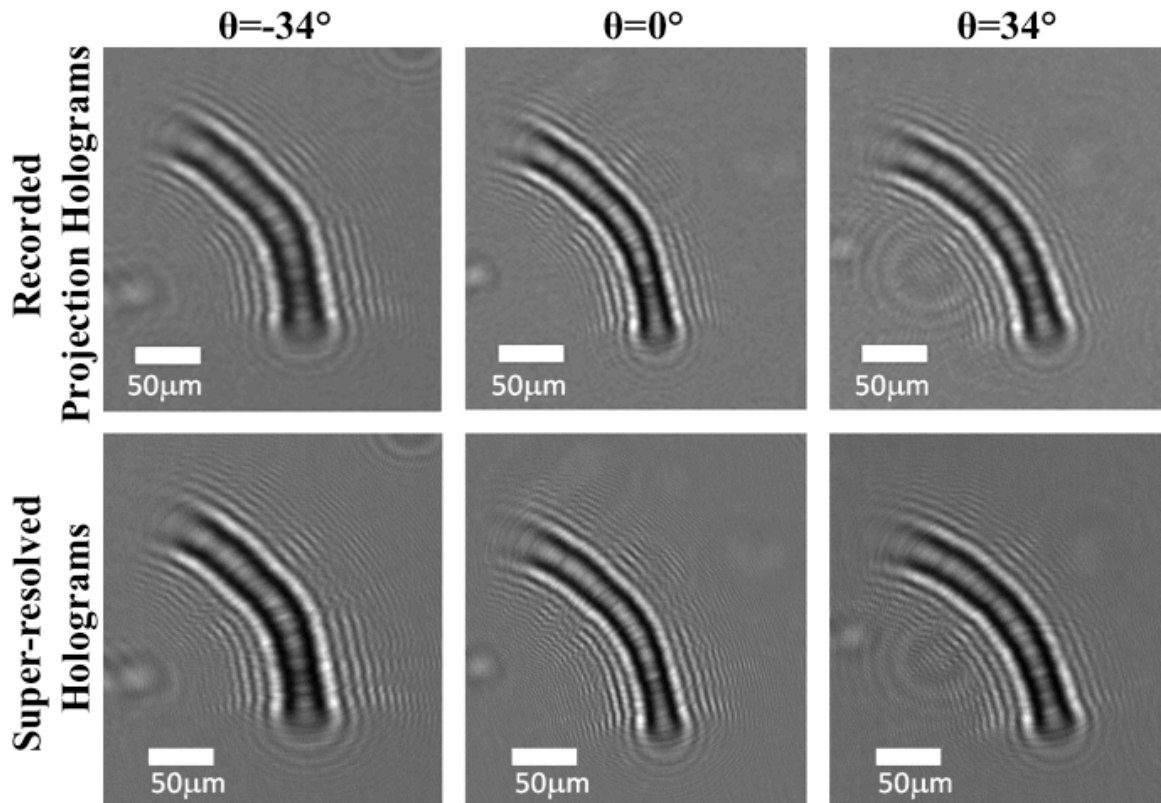


Figure 5-5 (Top) Recorded holograms of a *C. elegans* sample at three different illumination angles ( $\theta = 0^\circ$ ,  $34^\circ$ , and  $-34^\circ$ ). (Bottom) Pixel super-resolved holograms of the worm for the same illumination angles, which exhibits higher-frequency holographic fringes that are otherwise undersampled in the holograms. Lensfree holograms are naturally wider for the tilted illumination angles when compared to the vertical illumination hologram. [103]

As expected, the extent of the holograms along  $x$  gets wider at larger angles. By using the sub-pixel shifts of the worm during its flow within the micro-channel together with PSR techniques, super-resolved holograms of the sample at each illumination angle were obtained as presented in Figure 5-5. These SR holograms exhibit high spatial frequency fringes that were normally under-sampled in their corresponding raw lensfree holograms.

The SR holograms obtained at each angle are digitally reconstructed as described in Chapter 3. The projection images, some of which are shown in Figure 5-6 for various  $\theta$  values, are digitally obtained, which can be now back-projected to compute tomograms of the flowing objects.

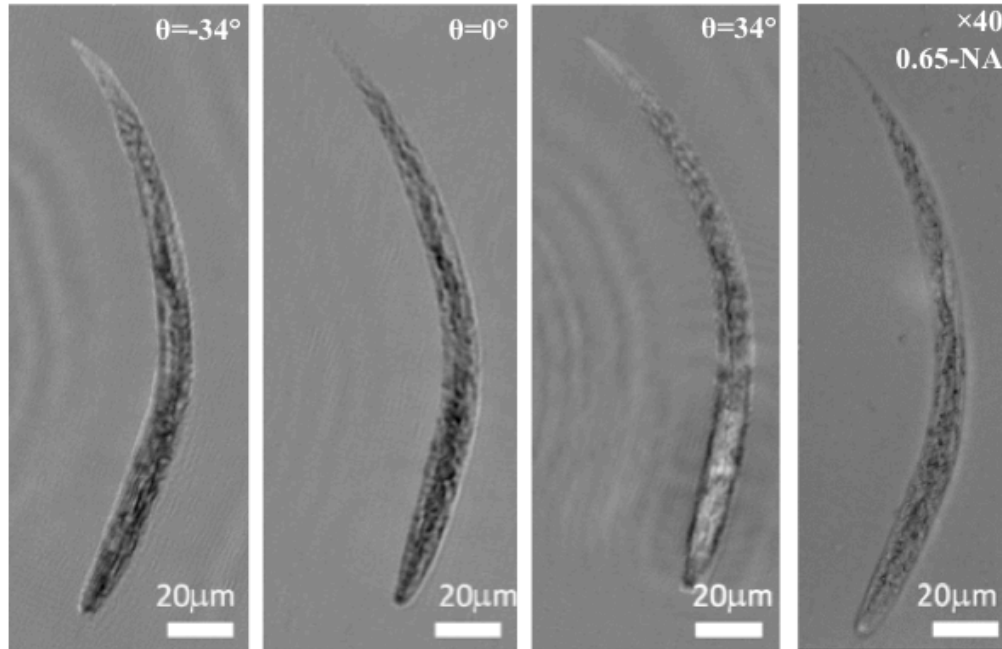


Figure 5-6 Digitally reconstructed amplitude images of the worm in Fig. 5-5 at illumination angles of  $\theta = -34^\circ$ ,  $0^\circ$ ,  $+34^\circ$ . A brightfield microscope image, obtained by a  $40\times$  objective lens, is also provided for visual comparison. [103]

Figure 5-7 demonstrates the tomographic imaging performance of HOT using a *C. elegans* sample by showing several slice images through the worm body. Different depth sections of the worm reveal distinctly details regarding the structure of the worm, which is otherwise unattainable by using a single SR image. In other words, the tomographic imaging approach significantly mitigates the well-known depth-of-focus problem (which indeed becomes beneficial for tomographic imaging by satisfying the projection approximation) inherent in holographic reconstruction modalities, and allows optofluidic sectional imaging with significantly improved axial resolution. The entire tomographic reconstruction process (including the synthesis of the SR holograms and the filtered back-projection) takes less than 3.5 minutes using a single GPU, which can be significantly improved by using several GPUs in parallel.

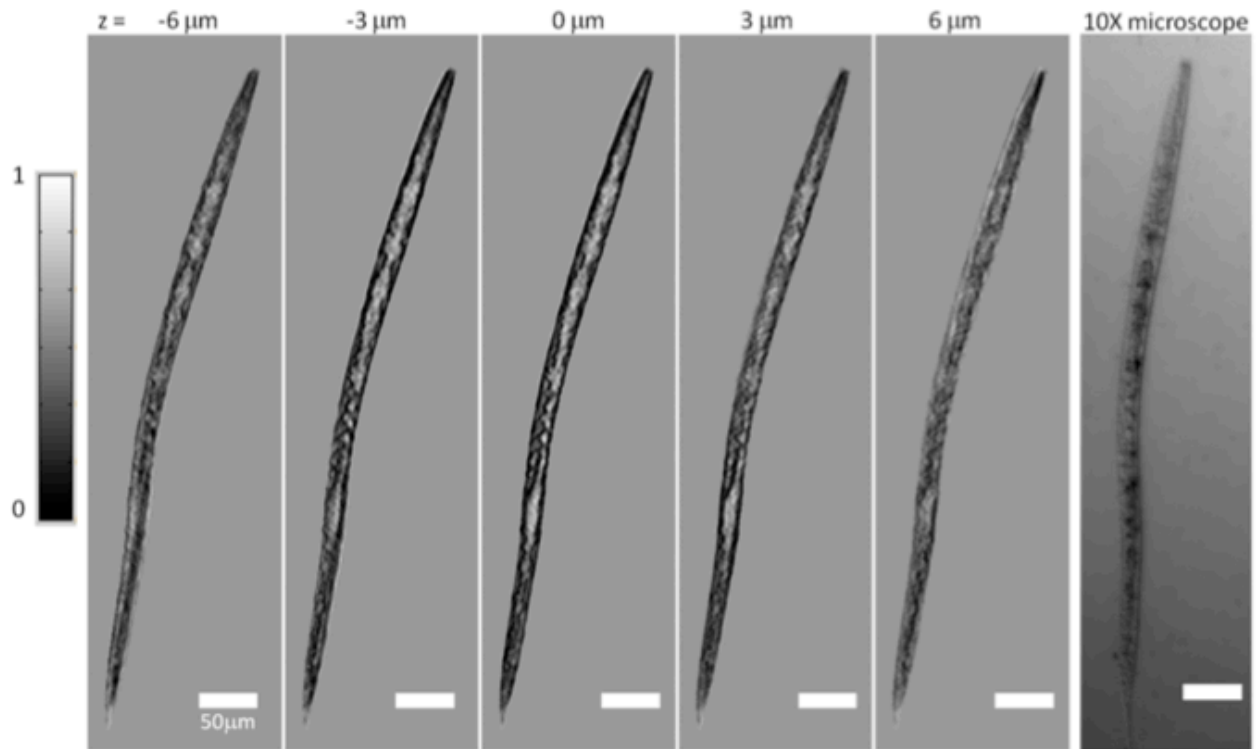


Figure 5-7 Tomographic optofluidic imaging of *C. Elegans* is illustrated at different depth slices (from  $z=-6\mu\text{m}$  to  $+6\mu\text{m}$ ). The FWHM of the amplitude of the line profile of the worm along  $z$  direction is  $\sim 30\mu\text{m}$ , which roughly agrees with the thickness of its body. The colorbar applies only to the tomographic images. Scale bars:  $50\mu\text{m}$ . [56]

The lensfree holographic on-chip imaging approach taken in HOT is one of the key enablers for obtaining multiple views of the flowing objects within a microfluidic channel. That is, the distance traversed by the object-wave until it reaches the sensor rapidly increases for large illumination angles, e.g.  $40-50^\circ$ , which further necessitates a “capability” to propagate the recorded image back to the object plane to prevent artifacts due to increased blurring (or defocusing) at large angles. Fortunately, HOT can digitally correct for this varying distance between the sensor and the object as a function of the illumination angle. Similarly, potential fluctuations of the object along the  $z$  direction (normal to the sensor plane) can also be digitally corrected for. This brings robustness to this optofluidic tomography platform as the vertical position of objects may vary during the flow. Therefore, the channel height can be increased to avoid clogging issues, which is an important practical advantage of this platform.

In summary, we have presented the demonstration of optofluidic tomographic microscopy using partially coherent lensfree digital in-line holography. This on-chip tomographic imaging modality would be quite valuable for micro-fluidic lab-on-a-chip platforms where high-throughput 3D imaging of the specimen is needed.

## 6 CONCLUSION

Existing optical tomography platforms, some of which are summarized in this dissertation, rely on relatively costly, complex and bulky optical setups that are challenging to miniaturize and integrate with microfluidic systems. Moreover, these platforms rely on lenses to achieve optical magnification. Therefore, they typically suffer from the trade-off between spatial resolution and imaging area, which leads to limited field-of-views (FOVs). Therefore, an alternative tomographic microscopy platform that offers both high resolution and a large imaging volume in a small form factor could provide an important imaging toolset in various fields including cell and developmental biology, neuroscience and drug discovery, and in global health applications. Toward this end, here I presented a new imaging modality, termed lensfree optical tomography (LOT). [55-59] LOT achieves  $\sim 0.35 \mu\text{m}$  lateral resolution together with an axial resolution of  $\sim 2 \mu\text{m}$  over a large FOV of  $\sim 20 \text{ mm}^2$  and a depth-of-field (DOF) of  $\sim 0.3 \text{ mm}$ , which could be further increased to e.g.,  $\sim 1\text{-}5 \text{ mm}$  at the cost of reduced spatial resolution. [57,58] Consequently, LOT merges high resolution in 3D with a large imaging volume, offering an exceedingly high 3D space-bandwidth product for high-throughput imaging applications.

The results presented in this dissertation constitute a number of novelties: (1) optical tomographic imaging has been extended to lensfree on-chip imaging modalities; and (2) dual-axis tomography has been applied to the visible spectrum; and (3) pixel super-resolution techniques have been applied for optical tomographic imaging. [57]

It should also be noted that lensfree holographic imaging techniques have a significant advantage over conventional microscopes in terms of scalability. That is, as the performance of optoelectronic sensor arrays improve (in terms of metrics such as pixel sizes, quantum efficiency, noise figures and imaging speed), it will directly translate to better performing lensfree on-chip microscopes. As importantly, this transition will be straightforward as the algorithms do not need to be modified.

Owing to its architectural simplicity, LOT also lends itself to a compact, cost-effective and field-portable imaging device. Toward this end, here I also demonstrated a field-portable lensfree tomographic microscope for use in resource-limited settings and in lab-on-a-chip applications. This tomographic microscope weighs only ~110 grams and has low power consumption so as to realize battery-powered operation in the field settings. This microscope utilizes a single axis (as opposed to two in the bench-top version) along which the illumination angle is varied, and has  $\sim 4^\circ$  increments between projections (as opposed to  $2^\circ$  in the bench-top version). Therefore, the axial-resolution was limited to  $\sim 7 \mu\text{m}$  in this portable microscope, while sub-micron lateral resolution could still be achieved, over a large imaging volume of  $\sim 20 \text{ mm}^3$ . Furthermore, the imaging volume can also be extended up to  $\sim 80 \text{ mm}^3$  (for a depth-of-field of  $\sim 4 \text{ mm}$ ) at the cost reduced spatial resolution. Offering a decent spatial resolution over such a large imaging volume, this compact, lightweight ( $\sim 110 \text{ grams}$ ) and cost-effective lensfree tomographic microscope could provide a valuable tool for telemedicine and high-throughput imaging applications in low-resource environments.

The compact and simple architecture of lensfree imaging also renders it a very suitable platform for microfluidic applications. By using simple light sources such as Light Emitting Diodes (LEDs), lensfree imaging can be integrated with microfluidic chips. Accordingly,

lensfree holograms of objects flowing within a microfluidic channel can be recorded. In fact, the flow of objects within the micro-channel is utilized for capturing multiple slightly different lensfree holograms of the same object, which allows lateral resolution enhancement using Pixel Super-Resolution (PSR) algorithms. This is an important example of how combining microfluidics with optics can indeed enhance the performance and versatility of a lab-on-a-chip device.

Overall, offering micron-scale spatial resolution over a large imaging volume, lensfree optical tomography could in general be quite useful for high-throughput imaging applications in e.g., cell and developmental biology, for global health applications where cost-effective and field-portable imaging devices can be desirable, and for integration with microfluidic chips in future lab-on-a-chip platforms.



# APPENDIX 1: Color and Monochrome Lensless On-chip Imaging of *Caenorhabditis Elegans* Over a Wide Field-of-View

## A1.1 Introduction

*Caenorhabditis Elegans* (*C. Elegans*) has been extensively studied as a model organism to better understand the underlying mechanisms of various human diseases. [105] It has several important features that justify this widespread use. First, *C. Elegans* is easy to culture in laboratory environments, growing and reproducing rapidly and cost-effectively. Further, it is a transparent, optically accessible organism with well-developed nervous and reproductive systems, intestine, skin and muscles. As a result, high-throughput phenotypical characterization of *C. Elegans* samples, which primarily involves optical imaging in the form of conventional microscopy, has led to important discoveries in biomedical research and specifically in drug discovery, significantly impacting genetics, oncology and neurobiology. [106-109] Motivated by these advances, various high-throughput platforms were demonstrated for phenotypical screening of this model organism. [110-112] Nevertheless, in all these existing systems, phenotype characterization still relies on conventional lens-based light microscopy, which has a limited imaging field of view, despite the use of bulky and expensive objective lenses.

To provide a high-throughput system for on-chip imaging of *C. Elegans* samples, I also developed a lensfree imaging platform capable of performing color and monochrome imaging. [104] When compared to the state of the art, our approach does not utilize any lenses, lasers or other bulky optical components or any mechanical scanning, making it highly compact and simple to use. This imaging approach is based on incoherent lensless in-line holography, as described in Chapter 2, which provides a significantly larger field-of-view (FOV), permitting

simultaneous imaging of *C. Elegans* samples over an area of e.g.  $>24 \text{ mm}^2$ , i.e.,  $\sim 10$  fold larger than a typical  $10\times$  objective-lens FOV. Digital reconstruction of the recorded lensless holograms rapidly creates the *C. Elegans* images within less than 1 sec; and by digitally combining these reconstructed images at three different wavelengths (red, green and blue) color images of the samples that are labeled with functional dyes are also acquired. Furthermore, this lensless holographic microscope requires almost no sensitive optical alignment, making it quite easy to operate, even for non-technical personnel. Through its integration with micro-fluidic systems, this lensless on-chip imaging platform, being much simpler and more compact than conventional optical microscopes, together with a significantly larger FOV, could especially be important for high-throughput imaging of *C. Elegans* samples providing a new tool for biomedical research in various fields including genetics, oncology and neurobiology.

## **A1.2 Experimental Methods and Results**

Similar to the system described in Chapter 2, a spatially incoherent light source (with a relatively broad bandwidth of  $\sim 15 \text{ nm}$ ) filtered through an aperture ( $50\text{-}100\mu\text{m}$ ) is used here. This light source is situated  $z_1=5\text{-}10 \text{ cm}$  above the sample plane. The *C. Elegans* samples, either placed within a microfluidic channel or simply onto a cover-glass, are placed with  $z_2<1\text{-}2 \text{ mm}$  distance to the sensor-array. The incoherent light picks up spatial coherence as it propagates over  $z_1$ , which permits recording of lensfree in-line holograms of each *C. Elegans* sample, individually. The fact that the coherence diameter at the sample plane is much smaller than the entire FOV ( $>24 \text{ mm}^2$ ) does not pose a limitation, since each *C. Elegans* sample is “effectively” illuminated by a coherent plane wave for digital recording of its lensless hologram. When compared to existing in-line holographic imaging platforms, the presented incoherent approach

has a rather un-conventional hologram recording geometry that has orders of magnitude larger  $z_1/z_2$  ratio, a unit fringe magnification and an unusually large source aperture ( $\sim 50\text{-}100\ \mu\text{m}$ ). These striking differences form the key to achieve lensfree holographic imaging over a wide FOV of  $>24\ \text{mm}^2$ , while using an incoherent source without the need for any mechanical alignment or light-coupling optics. This also enables significant reduction of speckle noise and undesired interference effects among objects of the same FOV. The trade-off for these advantages is that the pixel size of the sensor chip now starts to be the bottleneck for spatial resolution. However, as we illustrate in this manuscript, the reconstructed lensfree C. Elegans images still permit an imaging performance comparable to a  $10\times$  objective-lens ( $\text{NA}\sim 0.2$ ), while improving the FOV by  $\sim 10$  fold, without the use of any lenses or mechanical scanning.

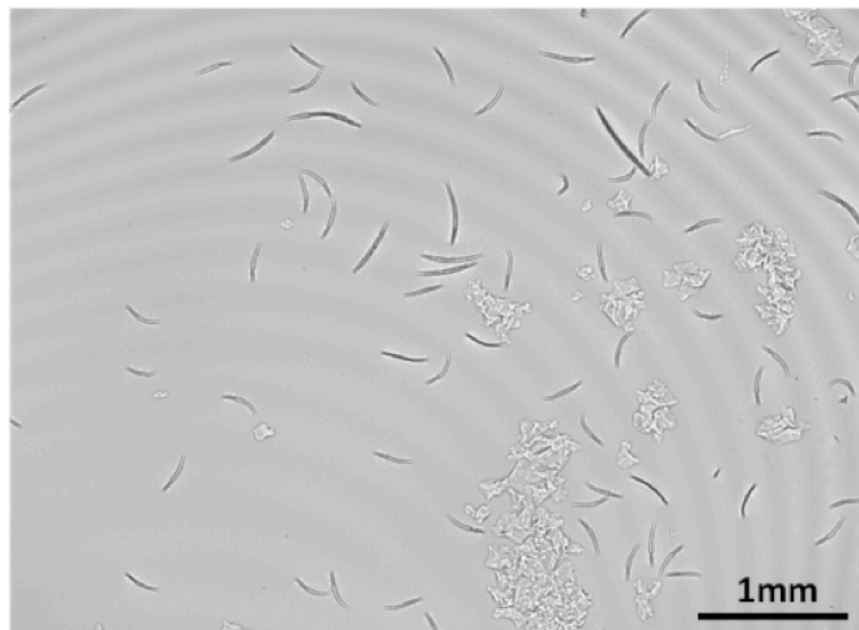


Figure A1-1 A lensfree hologram that is captured with the lensfree on-chip microscope is shown. Digital processing of this raw hologram permits simultaneous on-chip imaging of C. Elegans samples over  $>24\ \text{mm}^2$  FOV. Using a state of the art GPU, this digital reconstruction process takes  $<1$  sec over the entire imaging FOV. [104]

To illustrate its proof of concept, Fig. A1-1 shows a full FOV hologram recorded with this lensfree on-chip imaging system. Through digital reconstruction of the captured holograms, all

the *C. Elegans* samples within this large FOV can be simultaneously imaged and tracked for long-term observation of the animals.

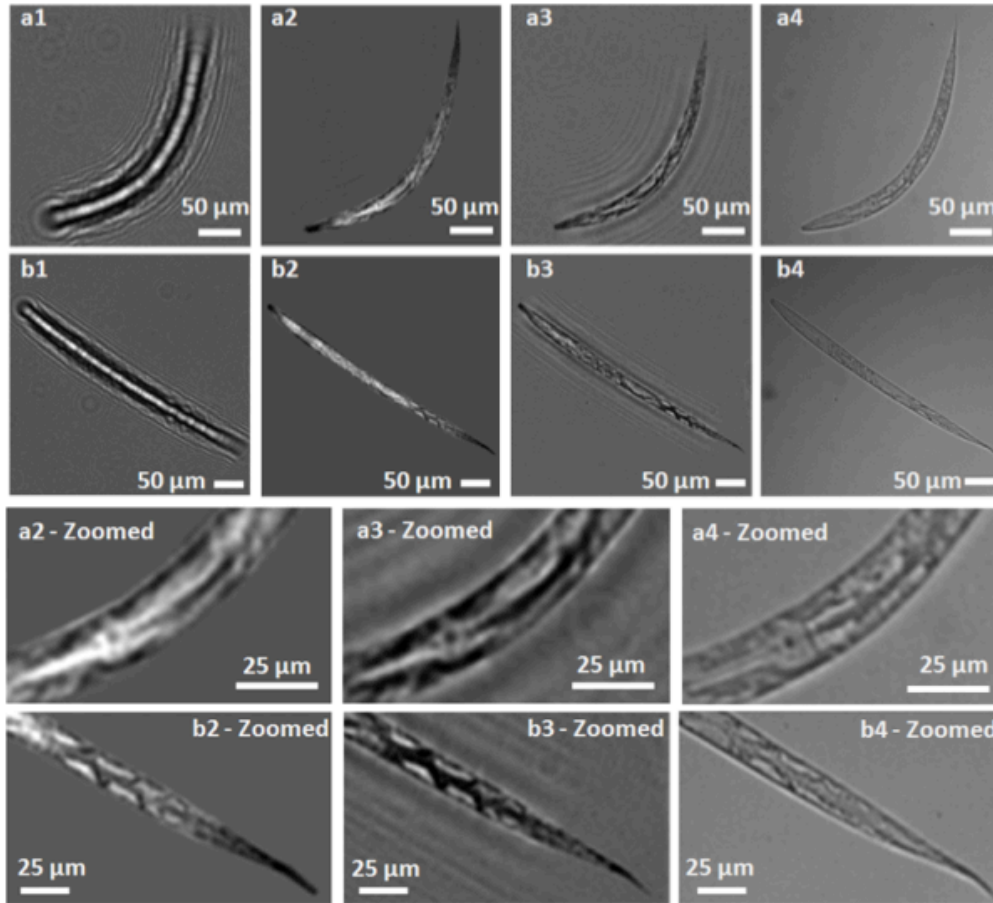


Figure A1-2 Incoherent lensfree on-chip imaging of two different *C. Elegans* samples. (a1, b1) Raw lensless holograms captured by the sensor-array. (a2, b2) Intensity images of the reconstructed holograms using method 1. (a3, b3) Intensity images of the reconstructed holograms using method 2. (a4, b4) Conventional 10X (NA=0.2) transmission microscope images of the same samples for comparison. The bottom two rows show the zoomed-in images to better illustrate the comparison. Experimental parameters:  $z_1=10\text{cm}$ ,  $z_2=1\text{mm}$ ,  $D=50\mu\text{m}$ , spatially incoherent light source at  $\lambda=500\text{nm}$  and a bandwidth of  $\sim 15\text{nm}$ . Exposure time  $\sim 30\text{ms}$ . [104]

Fig. A1-2 illustrates the imaging performance of the system for two different *C. Elegans* samples that are immobilized between two cover glasses. In this figure, (a1) and (b1) show the digitally cropped raw holograms from the larger FOV, whereas (a2), (b2) and (a3), (b3) show the intensity of the reconstructed images using two different methods. Both of these reconstruction methods recover the lost hologram phase through iterative constraint algorithms. Method #1 is a

twin-elimination algorithm for inline holograms [25] that utilizes the fact that the object information is present in two different planes, namely the real and virtual image planes of inline holography. On the other hand, method #2 is a more general phase recovery technique [25], which does not necessarily require a hologram as an input, and can work for the recovery of any complex optical field. As illustrated in Fig. A1-2, method #1 has stronger twin-image elimination capabilities while method #2 is more reliable for recording geometries with large Fresnel numbers ( $>10$ ). To better illustrate the imaging performance of the system, Fig. A1-2 also provides zoomed images of the worms. These reconstructed images agree very well with transmission microscope images (a4), (b4) that are obtained by a 10 $\times$  (NA=0.2) objective lens.

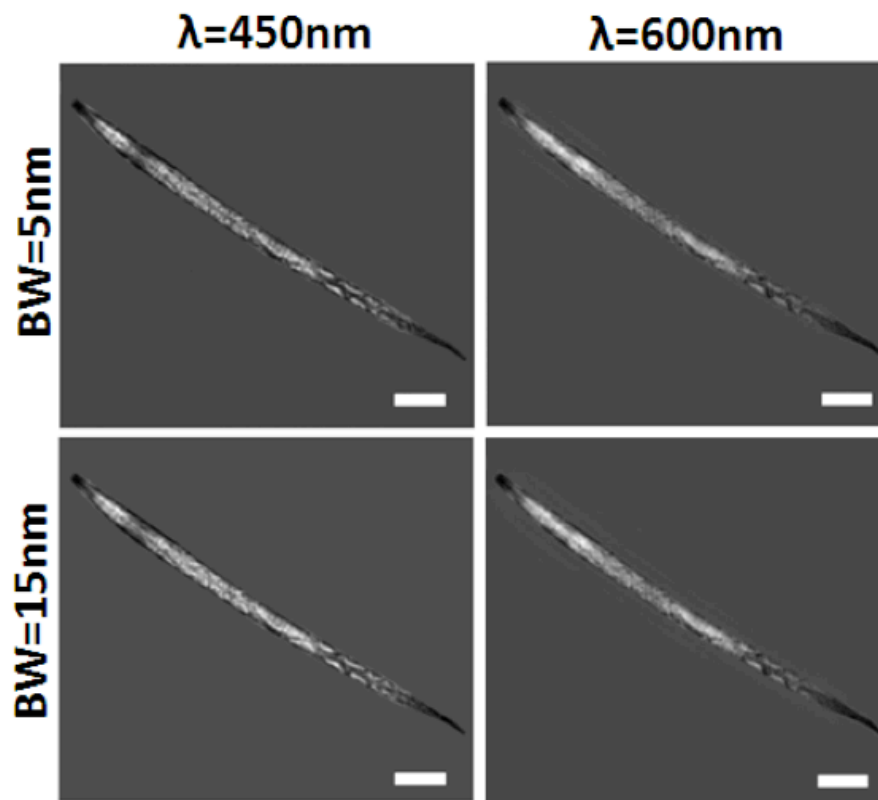


Figure A1-3 Reconstruction results (based on Method 1) of the *C. Elegans* sample shown in Figure A1-2(b) are illustrated with respect to two different illumination wavelengths and two different spectral bandwidths. All the other imaging conditions are the same as in Fig. A1-2. For comparison purposes, a microscope image of the same sample is shown in Figure A1-2(b4). Exposure times of the raw holographic images are  $\sim 200$ ms and  $\sim 30$  ms for the 5 nm and 15 nm bandwidth illumination, respectively. Scale bars, 50 $\mu$ m. [104]

Fig. A1-3 further illustrates the imaging performance of the lensless holographic on-chip imaging system under different illumination wavelengths and spectral bandwidths (BW)s. The results are shown only for method #1 since similar results are also obtained for method #2. The reconstructed images exhibit quite strong contrast to resolve the fine spatial features of the *C. elegans* samples in all cases.

It is important to note that pixel super-resolution was not used for the imaging experiments presented in Figures A1-2 and A1-3. As a result, the spatial resolution was mostly limited by the pixel size of the image sensor rather than temporal resolution. Therefore, using a wideband illumination did not degrade the imaging performance, as demonstrated in Fig. A1-3. Nevertheless, the state-of-the-art in lensfree on-chip imaging is to apply pixel super-resolution. In this case, however, the temporal resolution plays an important role, and a bandwidth of <5-10 nm is typically preferred. [29,31]

For various applications, the phenotype characterization is achieved by staining of the *C. Elegans* samples with functional dyes [113], and therefore color imaging is an important need for *C. Elegans* imaging. Towards this end, we also demonstrate the color imaging capability of our lensfree on-chip imaging platform using *C. Elegans* samples stained with Ponceau S red stain, which mostly marks the proteins in the middle and tail sections of the worms. After the labeling steps, by sequentially illuminating the samples with incoherent light at 450nm (Blue), 550nm (Green) and 650nm (Red), three holograms were obtained using the same set-up. Figs. A1-4(a), (b) and (c) show the separately reconstructed intensity images for each of these wavelengths for a given worm. After digitally fusing these reconstructed images at blue, green and red illumination wavelengths, a pseudo-color image is obtained as shown in Fig. A1-4(d), which

clearly reveals the red stained regions and compares successfully to the microscope image in Fig. A1-4(e).

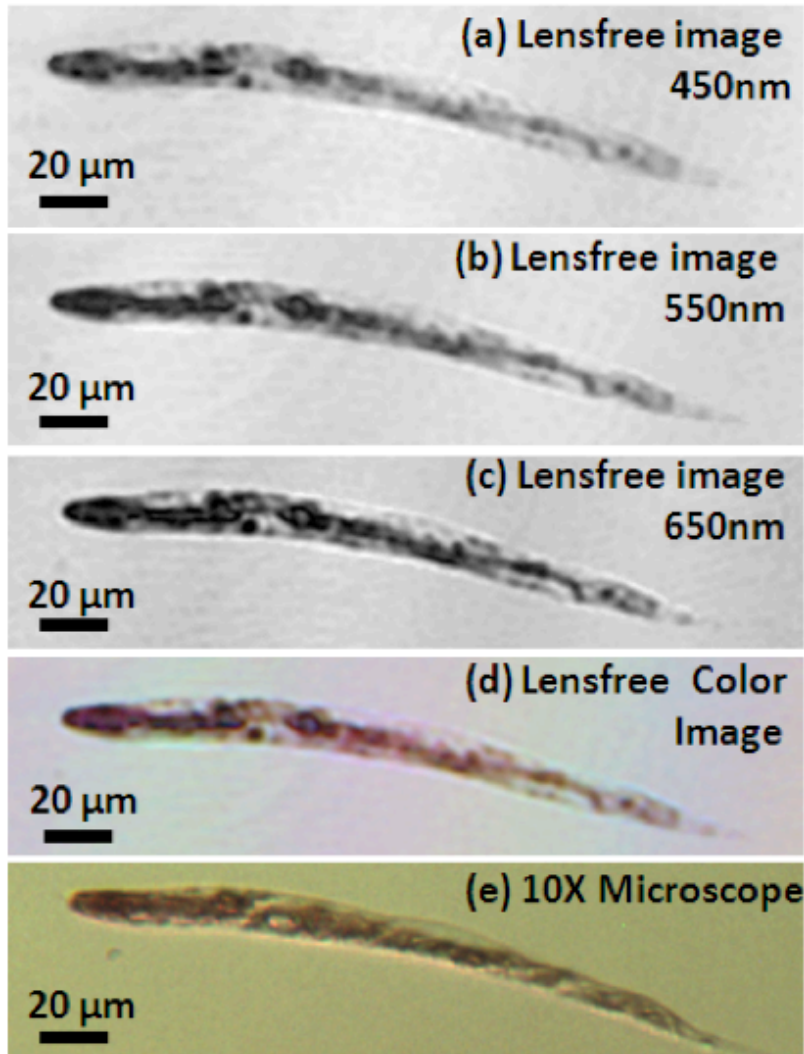


Figure A1-4 (a, b, c) Digitally reconstructed holographic images of a stained *C. Elegans* sample using Ponceau S red stain, captured with illumination wavelengths at 450nm, 550nm and 650nm, respectively (FWHM  $\sim$ 15 nm in each case). (d) Color image obtained by fusing the reconstructions at each wavelength. (e) Bright-field microscope image obtained with a 10 $\times$  objective lens for comparison purposes. [104]

In conclusion, we have demonstrated color and monochrome lensfree on-chip imaging of *C. Elegans* samples over a large FOV. Using incoherent lensfree in-line holography, diffraction holograms of *C. Elegans* samples are recorded on a chip, where digital reconstruction of these

lensless holograms rapidly creates the sample image with an FOV of  $>24 \text{ mm}^2$ , which constitutes ~10 fold improvement over the FOV of a typical 10 $\times$  objective-lens. Employing multi-wavelength illumination, we also demonstrated the color imaging performance of the system using *C. Elegans* samples dyed with nonspecific red Ponceau-S stain.



## APPENDIX 2: Tomographic Image Reconstruction using Filtered Backprojection

In this Appendix, the mathematical basis of tomographic image reconstruction using filtered backprojection will be provided. The fundamental goal in computed tomography is to determine the object function from its projections, as illustrated in Figure A2-1.

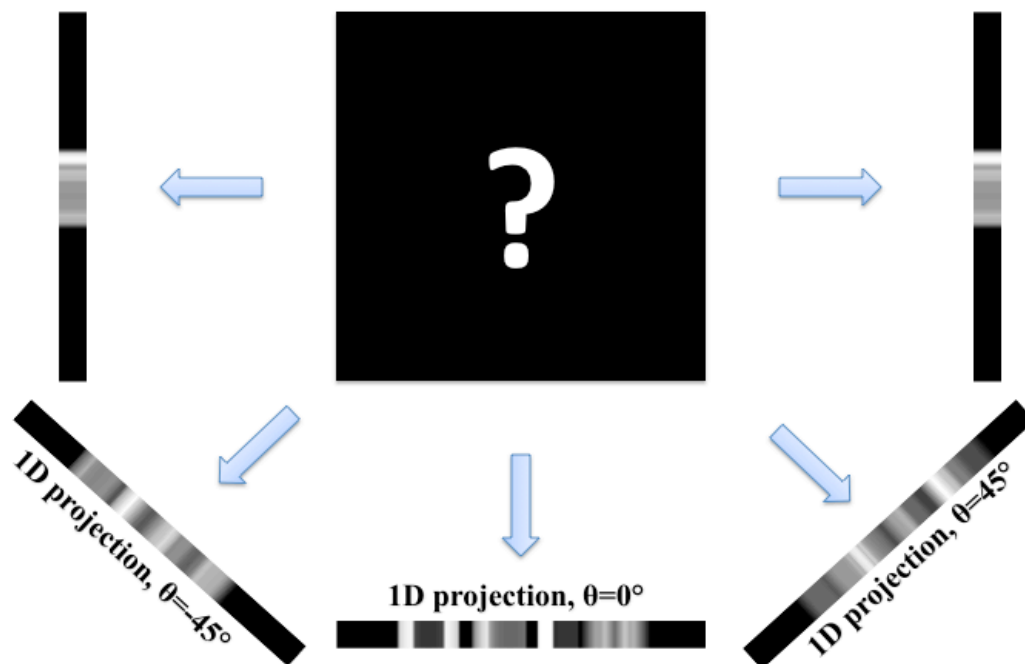


Figure A2-1. The fundamental goal in computed tomography is to determine the object function from its projections

Filtered backprojection is a mathematical operation that recovers the object function from its line integrals (projections) obtained along lines passing through the object at different angles. At the heart of this operation is the Fourier Slice theorem, which will be explained first. The following derivations are carried out for two-dimensional objects for the sake of simplicity, as

extension of the technique to 3D is straightforward. This derivation follows the approach presented in Ref. 114.

### A2.1 Fourier Slice Theorem

According to the Fourier slice theorem, the Fourier transform of the line integral (projection) of a two-dimensional function  $f(x,y)$  (e.g. a 2D object) obtained at angle  $\theta$  gives a slice, subtending an angle  $\theta$  with the  $u$ -axis, of the two-dimensional transform,  $F(u, v)$ , of the function  $f(x,y)$  (see Figure A2-2 for a pictorial definition).

This can be proven by first writing the definition of the 2D Fourier transform:

$$F(u,v) = \int_{-\infty}^{\infty} \int_{-\infty}^{\infty} f(x,y) e^{-j2\pi(ux+vy)} dx dy \quad (\text{A2-1})$$

where  $(x,y)$  are spatial coordinates in the space domain, and  $(u,v)$  are the spatial frequency components in the Fourier domain. The Fourier transform of the line integral of  $f(x,y)$  is given by:

$$S_{\theta}(w) = \int_{-\infty}^{\infty} P_{\theta}(t) e^{-j2\pi wt} dt \quad (\text{A2-2})$$

where  $w$  is the spatial frequency and  $P_{\theta}$  is the line integral of  $f(x,y)$  along  $\theta$ . Defining  $(t,s)$  as the rotated spatial coordinate system,

$$\begin{bmatrix} t \\ s \end{bmatrix} = \begin{bmatrix} \cos(\theta) & \sin(\theta) \\ -\sin(\theta) & \cos(\theta) \end{bmatrix} \begin{bmatrix} x \\ y \end{bmatrix} \quad (\text{A2-3})$$

we can rewrite  $P_{\theta}$  as:

$$P_{\theta}(t) = \int_{-\infty}^{\infty} f(t,s)ds \quad (\text{A2-4})$$

From (A2-2) and (A2-4), we can write:

$$S_{\theta}(w) = \int_{-\infty}^{\infty} \int_{-\infty}^{\infty} f(t,s)e^{-j2\pi w t} ds dt \quad (\text{A2-5})$$

Equation (A2-5) can be converted to the (x,y) coordinate system using coordinate transformation. Since the Jacobian of this transformation in (A2-3) is unity, we can write:

$$S_{\theta}(w) = \int_{-\infty}^{\infty} \int_{-\infty}^{\infty} f(x,y)e^{-j2\pi w [x \cos(\theta) + y \sin(\theta)]} dx dy \quad (\text{A2-6})$$

In (A2-6), the right hand side is simply the Fourier transform of  $f(x,y)$  evaluated along  $\theta$ , and left hand side is the Fourier transform of the projections as given by (A2-2). Then, equation (A2-6) is the definition of the Fourier slice theorem. Then, one can conclude that the 2D Fourier spectrum of the object can be obtained by synthesizing the 1D Fourier transforms of measured 1D projections, slice by slice. Then, the inverse transform of this 2D Fourier spectrum gives the object function,  $f(x,y)$ . While this approach is feasible, its implementation is challenging as the projections are sampled along different lines. That is, since each slice is uniformly sampled along a line, their combination is radially uniformly sampled. Therefore, the combined Fourier spectrum needs be resampled to obtain a Cartesian grid. Nevertheless, interpolation in frequency domain is prone to artifacts, and a space-domain approach proves to be more practical. This approach, known as filtered backprojection, will be described next.

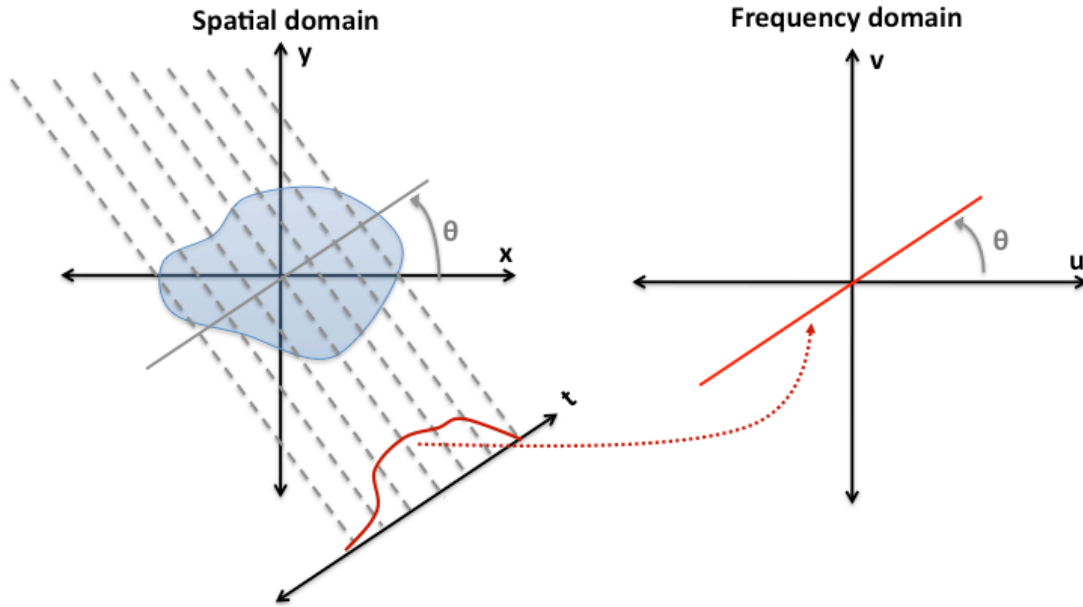


Figure A2-2 Pictorially explains the Fourier slice theorem.

## A2.2 Filtered Backprojection Algorithm

Since the projections are uniformly sampled along radial lines, it is helpful to write the definition of 2D inverse Fourier transformation in polar coordinates using the below coordinate transformation.

$$u = w \cos(\theta)$$

$$v = w \sin(\theta)$$

$$dudv = wdwd\theta$$

Then the definition of 2D inverse Fourier transformation can be written by,

$$f(x,y) = \int_0^{2\pi} \int_{-\infty}^{\infty} F(w,\theta) e^{j2\pi w(x \cos(\theta) + y \sin(\theta))} wdwd\theta \quad (\text{A2-7})$$

The above integration can be written as two separate integrations, one from  $[0,\pi]$ , and one from  $[\pi, 2\pi]$ :

$$f(x, y) = \int_0^{\pi} \int_{-\infty}^{\infty} F(w, \theta) e^{j2\pi w(x \cos(\theta) + y \sin(\theta))} w dw d\theta + \int_{\pi}^{2\pi} \int_{-\infty}^{\infty} F(w, \theta) e^{j2\pi w(x \cos(\theta + \pi) + y \sin(\theta + \pi))} w dw d\theta \quad (\text{A2-8})$$

Since  $F(w, \theta + \pi) = F(-w, \theta)$ , we can write:

$$f(x, y) = \int_0^{\pi} \int_{-\infty}^{\infty} F(w, \theta) |w| e^{j2\pi w(x \cos(\theta) + y \sin(\theta))} dw d\theta \quad (\text{A2-9})$$

From (A2-5), we know that  $F(w, \theta)$  is equal to  $S_{\theta}(w)$ . Then, we can finally write (A2.9) as:

$$f(x, y) = \int_0^{\pi} \left[ \int_{-\infty}^{\infty} S_{\theta}(w) |w| e^{j2\pi w(x \cos(\theta) + y \sin(\theta))} dw \right] d\theta \quad (\text{A2-10})$$

Interestingly, equation (A2-10) has a simple geometric interpretation. Basically, it can be interpreted as below:

- (1) *Inside the integration in the brackets:* Take the Fourier transform of a projection along  $\theta$ , and multiply it by a frequency ramp,  $|w|$ , which emphasizes the high frequencies.
- (2) *The integration in the brackets:* Obtain the inverse Fourier transform of this filtered spectrum along the slice subtending an angle  $\theta$ , which yields filtered 1D projections.

(3) *The outer integration:* Smear and linearly add the filtered 1D projections towards the 2D space, back towards the object; hence the name *filtered backprojection*.

This smearing, or backprojection, operation is pictorially seen in Figure A2-3.

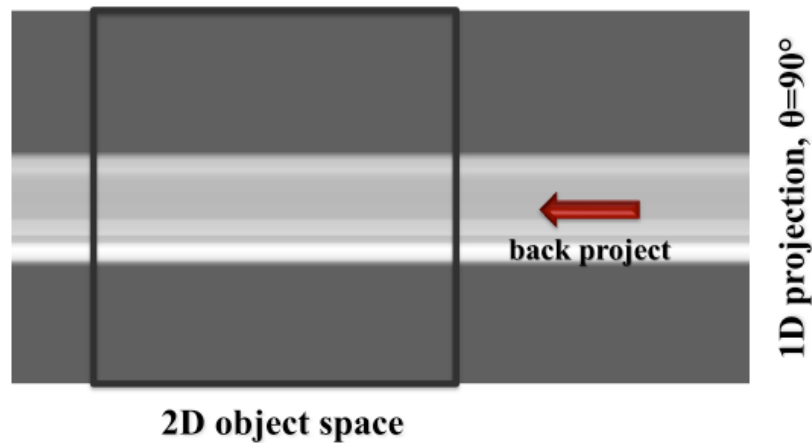


Figure A2-3 Pictorially explains the backprojection operation, which involves smearing a 1D projection towards the 2D object space.

As expected, smearing a single filtered projection is not sufficient to obtain a high quality image of the object. Nevertheless, continuously adding such projections in the object space eventually yields the reconstructed image (which is a white “UCLA” text on black background), as shown in Figure A2-4.



Figure A2-4 Shows that continuously adding projections, as shown in Fig. A2-3, in the object space eventually yields the reconstructed image (top) Reconstructed image by adding projections from  $[0, 60]$  degrees. (bottom) Reconstructed image by adding projections from  $[0, 180]$  degrees where the object (white UCLA text on black background) is reconstructed accurately.

## References

1. Melton L (2005) Imaging: The big picture. *Nature* 437:775-779
2. Dittrich PS, Manz A (2006) Lab-on-a-chip: microfluidics in drug discovery. *Nature Reviews Drug Discovery* 5:210-218
3. Squires TM and Quake SR (2005) Microfluidics: Fluid physics at the nanoliter scale *Rev. Mod. Phys.* 77, 977-1026
4. Whitesides G (2006) The origins and the future of microfluidics. *Nature* 442:368-373
5. Haeberle S and Zengerle R (2007) Microfluidic platforms for lab-on-a-chip applications. *Lab Chip* 7:1094-1110
6. Chin CD, Linder V and Sia SK (2007) Lab-on-a-chip devices for global health: Past studies and future opportunities. *Lab Chip* 7:41-57
7. Chabert M, Viovy JL (2008) Microfluidic high-throughput encapsulation and hydrodynamic self-sorting of single cells. *Proc. Nat. Acad. Sciences* 105:3191-3196
8. Oheim M (2007) High-throughput microscopy must re-invent the microscope rather than speed up its functions. *British J. of Pharmacology* 152:1-4
9. Rohde CB, Zeng F, Gonzalez-Rubio R, Matthew A, and Yanik MF (2007) Microfluidic system for on-chip high-throughput whole-animal sorting and screening at subcellular resolution. *Proc. Nat. Acad. Sciences* 104:13891-13895
10. Chung K, Crane MM and Lu H (2008) Automated on-chip rapid microscopy, phenotyping and sorting of *C. elegans*. *Nature Methods* 5:637-643



11. Hulme SE et al. (2010) Lifespan-on-a-chip: microfluidic chambers for performing lifelong observation of *C. elegans*. *Lab Chip*. 10:589–597
12. Sanz MA, Jong L, Tavernarakis N (2006) *Caenorhabditis elegans*: A versatile platform for drug discovery. *Biotechnology Journal* 1:1405-1418
13. Kaletta T, Hengratner M (2006) Finding function in novel targets: *C. elegans* as a model organism. *Nature Reviews Drug Discovery* 5:387-399
14. Hulme SE, Shevkoplyas SS, Apfeld J, Fontana W and Whitesides GM (2007) A microfabricated array of clamps for immobilizing and imaging *C. elegans*. *Lab Chip* 7:1515–1523
15. Kimmel CB (1995) Stages of Embryonic Development of the Zebrafish. *Developmental Dynamics* 203:255-310
16. Xu W, Jericho MH, Meinertzhagen IA and Kreuzer HJ (2001) Digital in-line holography for biological applications. *Proc. Natl. Acad. Sci. USA*, 2001, 98:11301-11305.
17. Xu W, Jericho MH, Kreuzer HJ and Meinertzhagen IA (2003) Tracking particles in four dimensions with in-line holographic microscopy. *Opt. Letters* 28:164-166
18. Pedrini G and Tiziani HJ (2002) Short-Coherence Digital Microscopy by Use of a Lensless Holographic Imaging System. *Appl. Optics* 41:4489-4496.
19. Repetto L, Piano E and Pontiggia C (2004) Lensless digital holographic microscope with light-emitting diode illumination. *Opt. Lett.* 29:1132-1134.
20. Garcia-Sucerquia J, Xu W, Jericho MH and Kreuzer HJ (2006) Immersion digital in-line holographic microscopy. *Opt. Lett.* 31:1211-1213.

21. Heng X, Erickson D, Baugh LR, Yaqoob Z, Sternberg PW, Psaltis D and Yang C (2006) Optofluidic microscopy—a method for implementing a high resolution optical microscope on a chip. *Lab Chip* 6: 1274-1276.
22. Psaltis D, Quake SR and Yang C (2006) Developing optofluidic technology through the fusion of microfluidics and optics. *Nature* 442:381-386.
23. Lew M, Cui X, Heng X and Yang C (2007) Interference of a four-hole aperture for on-chip quantitative two-dimensional differential phase imaging. *Opt. Lett.* 32:2963-2965
24. Gopinathan U, Pedrini G and Osten W (2008) Coherence effects in digital in-line holographic microscopy. *J. Opt. Soc. Am. A* 25:2459-2466
25. Mudanyali O et al. (2010) Compact, Light-weight and Cost-effective Microscope based on Lensless Incoherent Holography for Telemedicine Applications. *Lab Chip* 10:1417-1428
26. Oh C, Isikman SO, Khademhosseini B and Ozcan A (2010) On-chip differential interference contrast microscopy using lensless digital holography. *Opt. Express*, 18:4717-4726
27. Su T, Isikman SA O, Bishara W, Tseng D, Erlinger A and Ozcan A (2010) Multi-angle lensless digital holography for depth resolved imaging on a chip. *Opt. Express* 18:9690-9711
28. Seo S et al. (2010) High-throughput Lensfree Blood Analysis On a Chip. *Analytical Chemistry* 82:4621-4627
29. Bishara W, Su T, Coskun A F and Ozcan A (2010) Lensfree on-chip microscopy over a wide field-of-view using pixel super-resolution. *Optics Express* 18:11181-11191

30. Su TW, Xue L and Ozcan A (2012) High-throughput lensfree 3D tracking of human sperms reveals rare statistics of helical trajectories”, Proc. Nat. Acad. Sci., DOI: 10.1073/pnas.1212506109
31. Greenbaum A, Luo W, Su TW, Göröcs Z, Xue L, Isikman SO, Coskun AF, Mudanyali O, and Ozcan A (2012) ”Imaging without lenses: achievements and remaining challenges of wide-field on-chip microscopy,” Nature Methods, vol. 9, no.9.
32. Meng H and Hussain F (1995) In-line recording and off-axis viewing technique for holographic particle velocimetry. *Applied Optics* 34:1827-1840
33. Sheng J, Malkiel E and Katz J (2003) Single Beam Two-Views Holographic Particle Image Velocimetry. *Applied Optics* 42:235-250
34. Sharpe J et al. (2002) Optical Projection Tomography as a Tool for 3D Microscopy and Gene Expression Studies. *Science* 296:541-545
35. Fauver M and Seibel EJ (2005) Three-dimensional imaging of single isolated cell nuclei using optical projection tomography. *Optics Express* 13:4210-4223
36. Choi W et al. (2007) Tomographic Phase Microscopy. *Nature Methods*, 4:717 - 719
37. Choi W et al. (2008) Extended depth of focus in tomographic phase microscopy using a propagation algorithm. *Optics Letters* 33:171-173
38. Sung Y, Choi W, Fang-Yen C, Badizadegan K, Dasari RR, Feld MS (2008) Optical Diffraction Tomography for high resolution live cell imaging. *Opt. Express* 17:266-277
39. Fang-Yen C, Choi W, Sung Y, Holbrow CJ, Dasari RR, Feld MS (2011) Video Rate Tomographic Phase Microscopy. *J. of Biomed. Opt.* 16:011005(1-5)

40. Debailleul M, Simon B, Georges V, Haeberle O and Lauer V (2008) Holographic microscopy and diffractive microtomography of transparent samples. *Meas. Sci. Technol.* 19:074009 (8pp)
41. Charrière F et al. (2006) Living specimen tomography by digital holographic microscopy: morphometry of testate amoeba. *Optics Express* 14:7005-7013
42. Poon TC, Wu MH, Shinoda K and Suzuki Y (1996) “Optical Scanning Holography”, *Proc. of IEEE*, 84, 753-764
43. Lin YC, Cheng CJ and Poon TC (2011) “Optical sectioning with a low-coherence phase-shifting digital holographic microscope”, *App. Opt.*, 50, B25-B30
44. León LM, Pedrini G and Osten W (2005) “Applications of short-coherence digital holography in microscopy”, *App. Opt.*, 44, 3977-3984
45. Kuhn J et al. (2009) Submicrometer tomography of cells by multiple wavelength digital holographic microscopy in reflection. *Optics Letters* 34:653-655
46. Yu L and Kim MK (2005) Wavelength-scanning digital interference holography for tomographic three-dimensional imaging by use of the angular spectrum method. *Optics Letters* 30, 2092-2094
47. Hahn J, Lim S, Choi K, Horisaki R and Brady DJ (2011) “Video-rate compressive holographic microscopic tomography”, *Opt Exp*, 19, 7289–7298.
48. Moon I and Javidi B (2008) 3-D visualization and identification of biological microorganisms using partially temporal incoherent light in-line computational holographic imaging. *IEEE Trans. Med. Imaging* 27, 1782–1790.

49. Moon I, Daneshpanah M, Javidi B and Stern A (2009) “Automated three dimensional identification and tracking of micro/nano biological organisms by computational holographic microscopy” *Proc. IEEE*, 97, 990–1010.
50. Javidi B, Moon I, Yeom S and Carapezza E (2005) “Three-dimensional imaging and recognition of microorganism using single-exposure on-line (SEOL) digital holography”, *Opt Exp*, 13, 4492–4506.
51. Rosen J and Brooker G (2008) “Non-scanning motionless fluorescence three-dimensional holographic microscopy”, *Nat. Photon.*, 2, 190-195.
52. Rosen J and Brooker G (2007) “Fluorescence incoherent color holography”, *Opt Exp*, **15**, 2244-2250.
53. Rosen J, Katz B, Brooker G (2009) “Review of Three-Dimensional Holographic Imaging by Fresnel Incoherent Correlation Holograms”, *3D Research* **1**, 010103.
54. Huisken J et al. (2004) Optical Sectioning Deep Inside Live Embryos by Selective Plane Illumination Microscopy. *Science* 305:1007-1009
55. Isikman SO, Bishara W, Sikora U, Yaglidere O, Yeah J, et al. (2011) Field-portable lensfree tomographic microscope. *Lab on a Chip* 11: 2222. doi:10.1039/c1lc20127a.
56. Isikman SO, Bishara W, Zhu H, Ozcan A (2011) Optofluidic Tomography on a Chip. *Applied Physics Letters* 98: 161109. doi:10.1063/1.3548564.
57. Isikman SO, Bishara W, Mavandadi S, Yu FW, Feng S, et al. (2011) Lens-free optical tomographic microscope with a large imaging volume on a chip. *Proceedings of the National Academy of Sciences* 108: 7296–7301. doi:10.1073/pnas.1015638108.

58. Isikman SO, Greenbaum A, Luo W, Coskun AF, and Ozcan A (2012) "Giga-Pixel Lensfree Holographic Microscopy and Tomography using Color Image Sensors", PLoS ONE, 7(9), e45044.
59. Isikman SO, Bishara W, Ozcan A (2011) "Partially Coherent Lensfree Optical Tomographic Microscopy", Applied Optics, vol. 50, iss. 34, 253-264.
60. Garcia-Sucerquia J, Xu W, Jericho SK, Klages P, Jericho MH, and Kreuzer JH (2006) "Digital in-line holographic microscopy," Appl. Opt., **45**, 836-850.
61. Xu W, Jericho MH, Meinertzhagen IA, and Kreuzer HJ (2001) "Digital in-line holography for biological applications", Proc. Nat. Acad. Sci., **98**, 11301-11305.
62. Brady DJ, :Optical Imaging and Spectroscopy", John Wiley & Sons, Hoboken, NJ, USA, (2009).
63. Goodman JW, "Introduction to Fourier Optics", Roberts & Company Publishers, Greenwood Village, CO, USA, (2005).
64. Koren G, Polack F and Joyeux D (1993) "Iterative algorithms for twin-image elimination in in-line holography using finite-support constraints", J. Opt. Soc. Am. A, vol.10, pp. 423–433.
65. Fienup JR (1978), "Reconstruction of an object from the modulus of its Fourier transform", Opt. Lett., 3, 27–29.
66. Bishara W, Zhu H, and Ozcan A (2010) "Holographic Opto-fluidic Microscopy," Optics Express, vol. 18, iss. 26.

67. Bishara W, Sikora U, Mudanyali O, Su TW, Yaglidere O, Luckhart S, and Ozcan A (2011) “Holographic pixel super-resolution in portable lensless on-chip microscopy using a fiber-optic array,” *Lab Chip*, vol.11, pp. 1276-1279.
68. Hardie RC (1998), “High-resolution image reconstruction from a sequence of rotated and translated frames and its application to an infrared imaging system”, *Optical Engineering*. 37:247.
69. Park SC, Park MK, and Kang MG (2003), “Super-resolution image reconstruction: a technical overview”, *IEEE Signal Processing Magazine*. 20:21-36.
70. Lam EY, Zhang X, Vo H, Poon TC, and Indebetouw G (2009) “Three-dimensional microscopy and sectional image reconstruction using optical scanning holography”, *App. Opt.*, 48, H113-H119.
71. Brady DJ, Choi K, Marks DL, Horisaki R, Lim S (2009) “Compressive holography”, *Opt Exp*, 17, 13040–13049.
72. Meng H, Hussain F (1995) “In-line recording and off-axis viewing technique for holographic particle velocimetry”, *Appl Opt*, 34, 1827–1840.
73. Radermacher M (2006) in *Weighted back-projection methods. Electron Tomography: Methods for three dimensional visualization of structures in the cell*, (Springer, New York, 2nd ed.) pp 245-273
74. Mastrorarde DN (1997) *Dual-Axis Tomography: An Approach with Alignment Methods That Preserve Resolution*. *Journal of Structural Biology* 120:343–352
75. Arslan I, Tong JR, Midgley PA (2006) *Reducing the missing wedge: High-resolution dual axis tomography of inorganic materials*. *Ultramicroscopy* 106:994–1000

76. Verhoeven D (1993) Limited-data computed tomography algorithms for the physical sciences. *App. Optics* 32:3736-3654
77. Oh WY, Bouma BE, Ifimia N, Yelin R, Tearney GJ (2006) Spectrally-modulated full-field optical coherence microscopy for ultrahigh-resolution endoscopic imaging. *Optics Express* 14: 8675. doi:10.1364/OE.14.008675.
78. Sung Y, Choi W, Fang-Yen C, Badizadegan K, Dasari RR, et al. (2009) Optical diffraction tomography for high resolution live cell imaging. *Optics Express* 17: 266. doi:10.1364/OE.17.000266.
79. Rohde C B, Zeng F, Gonzalez-Rubio R, Matthew A, and Yanik MF (2007) Microfluidic system for on-chip high-throughput whole-animal sorting and screening at subcellular resolution. *Proc. Nat. Acad. Sciences* 104:13891-13895
80. Chung K, Crane MM and Lu H (2008) Automated on-chip rapid microscopy, phenotyping and sorting of *C. elegans*. *Nature Methods* 5:637-643
81. Hulme SE et al. (2010) Lifespan-on-a-chip: microfluidic chambers for performing lifelong observation of *C. elegans*. *Lab Chip*. 10:589–597
82. Sanz MA, Jong L, Tavernarakis N (2006) *Caenorhabditis elegans*: A versatile platform for drug discovery. *Biotechnology Journal* 1:1405-1418
83. Kaletta T, Hengratner M (2006) Finding function in novel targets: *C. elegans* as a model organism. *Nature Reviews Drug Discovery* 5:387-399
84. Hulme SE, Shevkoplyas SS, Apfeld J, Fontana W and Whitesides GM (2007) A microfabricated array of clamps for immobilizing and imaging *C. elegans*. *Lab Chip* 7:1515–1523



85. Kimmel CB (1995) Stages of Embryonic Development of the Zebrafish. *Developmental Dynamics* 203:255-310
86. Wolf E (1969) Three-dimensional structure determination of semi-transparent objects from holographic data. *Optics Communications* 1:153-156
87. Guo P and Devaney AJ (2005) Comparison of reconstruction algorithms for optical diffraction tomography. *Journal of Opt. Soc. Am. A* 22:2338:2347
88. Ntziachristos V (2010) Going deeper than microscopy: the optical imaging frontier in biology. *Nature Methods* 7:603-614
89. Roark RJ, *Roark's Formulas for Stress and Strain*, 6th ed., Warren C. Young Editor, New York, McGraw-Hill Book Co., 1989.
90. Yang YT, Heh D, Wei PK, and Fann WS (1997), "The probe dynamics under shear force in near-field scanning optical microscopy", *J. Appl. Phys.* 81, 1623.
91. Liu C, Tsao T, Lee GB, Leu JTS, Yi YW, Tai YC, Ho CM (2010), "Out-of-plane magnetic actuators with electroplated permalloy for fluid dynamics control", *Sensors and Actuators*, 78, 19
92. Fainman Y., L. Lee, D. Psaltis, and C. Yang, "Optofluidics: fundamentals, devices, and applications", McGraw-Hill, 2009.
93. Psaltis D, Quake SR, and Yang C (2006) "Developing optofluidic technology through the fusion of microfluidics and optics", *Nature*. 442:381-386.
94. Monat C, Domachuk P, and Eggleton BJ (2007) "Integrated optofluidics: a new river of light", *Nature Photonics*. 1:106-114.

95. Li Z, Zhang Z Emery T, Scherer A, and Psaltis D (2006) “Single mode optofluidic distributed feedback dye laser”, *Optics Express*. 14:696.
96. Agarwal A and Sharma RK (2007) “Automation is the key to standardized semen analysis using the automated sq-a-v sperm quality analyzer”, *Fertility and Sterility*. 87:156-162.
97. Heng X, Erickson D, Baugh LR, Yaqoob Z, Sternberg PW, Psaltis D, and Yang C (2006) “Optofluidic microscopy--a method for implementing a high resolution optical microscope on a chip”, *Lab on a Chip*. 6:1274-1276.
98. Cui X, Lee LM, Heng X, Zhong W, Sternberg PW, Psaltis D, and Yang C (2008) “Lensless high-resolution on-chip optofluidic microscopes for caenorhabditis elegans and cell imaging”, *Proceedings of the National Academy of Sciences of the United States of America*. 105:10670-10675.
99. Lee LM, Cui X, and Yang C (2009) “The application of optofluidic microscopy for imaging Giardia lamblia trophozoites and cysts”, *Biomedical Microdevices*. 11:951-958.
100. Pang S, Cui X, DeModena J, Wang YM, Sternberg P, and Yang C (2010) “Implementation of color capable optofluidic microscope on a RGB CMOS color sensor chip Substrate”, *Lab on a Chip*. 10:411-414.
101. Bishara W, Zhu H, and Ozcan A (2010) “Holographic opto-fluidic microscopy”, vol. 18, iss. 26.
102. Isikman SO, Bishara W, Zhu H and Ozcan A (2011) “Optofluidic Tomography on a chip”, *Applied Physics Letters*. 98:161109.

103. Bishara W, Isikman SO, and Ozcan A (2011), “Lensfree Optofluidic Microscopy and Tomography,” *Annals of Biomedical Engineering*, vol. 40, no.2.
104. Isikman SO, Sencan I, Mudanyali O, Bishara W, Oztoprak C, Ozcan A (2010), “Color and monochrome lensless on-chip imaging of *Caenorhabditis elegans* over a wide field-of-view”, *Lab Chip*, 10(9): 1109–1112.
105. Kaletta T and Hengartner MO (2006) “Finding function in novel targets: *C. elegans* as a model organism” *Nature Reviews Drug Discovery*, 5, 387-399
106. Barr MM and Sternberg PW (1999), “A polycystic kidney-disease gene homologue required for male mating behaviour in *C. elegans*” *Nature*, 401, 386-389
107. Hara M and Han M (1995) “Ras farnesyltransferase inhibitors suppress the phenotype resulting from an activated ras mutation in *Caenorhabditis elegans*” *Proc. Natl. Acad. Sci. U. S. A.*, 92, 3333-3337
108. Kim H, Rogers MJ, Richmond JE and McIntire SL (2004) “SNF-6 is an acetylcholine transporter interacting with the dystrophin complex in *Caenorhabditis elegans*” *Nature*, 430, 891-896
109. Yanik MF, Cinar H, Cinar HN, Chisholm AD, Jin Y and Yakar AB (2004), “Nerve regeneration in *Caenorhabditis elegans* after femtosecond laser axotomy” *Nature*, 432, 822
110. Crane MM, Chung K, Lu H (2009) “Computer-enhanced high-throughput genetic screens of *C. elegans* in a microfluidic system”, *Lab Chip*, 9, 38-40
111. Burns AR, Kwok TCY, Howard A, Houston E, Johanson K, Chan A, Cutler SR, McCourt P and Roy PJ (2006) “High-throughput screening of small molecules for bioactivity and target identification in *Caenorhabditis elegans*”, *Nature Protocols*, 1, 1906-1914

112. Dupuy D. (2007) “Genome-scale analysis of in vivo spatiotemporal promoter activity in *Caenorhabditis elegans*” *Nature Biotech.*, 25, 663-668.
113. Joung JK, Ramm EI and Pabo CO (2000), “A bacterial two-hybrid selection system for studying protein–DNA and protein–protein interactions” *Proc. Natl. Acad. Sci. U. S. A.*, 97, 7382–7387
114. Kak AC, Slaney M, “Principles of Computerized Tomographic Imaging”, Society for Industrial and Applied Mathematics, Philadelphia (2001)